SPIN COATING OF NEWTONIAN AND NON-NEWTONIAN FLUIDS

A THESIS SUBMITTED TO THE UNIVERSITY OF CAPE TOWN
IN FULFILMENT OF THE REQUIREMENTS FOR THE
DEGREE OF DOCTOR OF PHILOSOPHY

April, 2006

By
Mubanga Lombe
Department of Mathematics & Applied Mathematics
Faculty of Science

Abstract

The work in this thesis deals with the axisymmetric flow of a thin fluid layer on a rotating substrate.

In Chapter 3, a theoretical model is developed for the axisymmetric flow of a thin Newtonian fluid layer on a rotating disk, under the influence of surface tension, gravity, centrifugal and Coriolis forces. The starting point of the theoretical description is a non-dimensional analysis of the Navier-Stokes equations. These are reduced to a more tractable form using lubrication theory. The result is a well-known equation for the film height. This equation is solved numerically using a semi-implicit (upwind) scheme, to provide an estimate for the fluid thickness or film height. Simulations are then carried out using parameter values found in some experiments and certain spin coating applications. To study the effect of gravity and surface tension in particular, on the shape and spread rate of the fluid, various combinations of these effects are taken. The simulations reveal that surface tension and gravity have a significant effect on the shape and rate of spreading of a film. This is most significant at the moving front, where the characteristic capillary ridge develops.

In Chapter 4, the role of the Coriolis force on the evolution of a thin axisymmetric Newtonian fluid layer on a rotating disk is investigated. The analysis shows that the Coriolis force, together with the inertia term may only enter as a correction to the classical solution of the height for the free surface. This result is in direct contradiction to certain claims in the literature. We therefore explain the errors in the previous work.

In Chapter 5, the Newtonian model is then extended to deal with non-Newtonian fluids, using the power-law and Ellis viscosity models. A direct extension of the Newtonian scheme is not possible to implement because of the expression for flux in the non-Newtonian models. A normalisation of the flux is therefore introduced. This results in an innovative numerical scheme that is straightforward to implement as an extension of the Newtonian scheme. The predicted profiles of the non-Newtonian fluids show features which have not been previously

demonstrated in the literature, presumably since this is the first time that surface tension has been included in a numerical model of non-Newtonian rotating flow. The results obtained also show that surface tension and gravity have a significant influence on the resulting profiles, especially at the moving front, reducing the rate of spreading of the fluid.

Declaration

Thesis title : Spin coating of Newtonian & non-Newtonian fluids

I hereby grant the University of Cape Town permission to reproduce the above thesis in whole or in part, for the purpose of research.

I hereby declare that:

- the above thesis is my own work, apart from the normal guidance from my supervisor,
- neither the substance nor any part of the above thesis has been submitted in the past, or is being, or is to be submitted for another degree or qualification at this or any other University or institution of learning.

Signature : Signed by candidate

Date : 13/04/06

In loving memory of my sister, Sampa,
who never got to see the conclusion of this project...

Acknowledgements

I would like to thank my supervisor Prof. Tim G. Myers, for giving me the opportunity to carry out this project and for his supererogatory contribution to the completion of this thesis, the many suggestions and 'nice' comments which helped remove many obscurities along the way, and for the fun and cheerful way in which this was done. I am also thankful to Dr Jean P. F. Charpin for his time and skilful assistance with the computational work.

I am grateful to the Third World Organization for Women in Science (TWOWS) for the fellowship which was awarded to me for the period 2001–2004. The funding received from the National Research Foundation (NRF) in 2005 is also kindly acknowledged. I would like to thank the University of Cape Town and the University of Zambia as well, for their support throughout this period.

I would also like to thank the following: my daughter, Chewe, for her patience and understanding nature, especially during my stay in Cape Town; my parents, for their encouragement, loving support and for being there for me, I would not have done this without them; Aunt Ruth for her enthusiastic encouragement; Kangwa for all the roles that she has had to take on in my absence, I am indebted; my brothers for believing in me; Chimfwembe for her encouraging support, Lenganji and Chichi for giving me the inspiration to go on.

Thanks must also go to Derrick Mwansa whose loving support, patience and constant encouragement gave me the oomf to realise this goal.

Finally, I also wish to thank friends and relatives at home and in Cape Town, (ala mwalifula to mention all of you by name...) for all the encouragement over the past few years.

You all made it happen!!!

Cape Town, South Africa
April 13, 2006

Mubanga Lombe

Contents

List of Figures

List of Tables

Nomenclature

h	film thickness
h_0	initial film thickness
h_p	precursor film thickness
t	current time
Q	volumetric flow rate
Ω	angular velocity
μ	dynamic viscosity
ν	kinematic viscosity
ρ	density
L	characteristic length
H	characteristic height
δ	aspect ratio
r, θ, z	cylindrical polar coordinates
u, v, w	velocity vector
ϕ	angle to horizontal
C	inverse capillary number
E	evaporation factor
B	Bond number
p	pressure
p_a	ambient pressure
g	gravity
Re	Reynolds number
ε, ϵ	small parameter
σ	surface tension
η	non-Newtonian viscosity
n	power law index

κ	curvature or power law parameter
η_0	zero shear viscosity
η_∞	infinite shear viscosity
τ	shear stress
$\dot{\gamma}$	shear rate
$\tau_{1/2}$	parameter in Ellis model
α	parameter in Ellis model
λ	parameter in Carreau model

Chapter 1

Introduction & Literature Review

1.1 Motivation and research goals

This work is motivated by our interest in studying centrifugal spinning of liquid films as a convenient method for coating a substrate, such as a disk, with a uniform film.

Spin coating is a process that is used to produce thin uniform films by the spinning of a viscous fluid on a rotating disk. The fluid may be deposited onto the disk in various ways: as a pool of fluid at the centre of the disk (see figure 1.1) or through a hole in the centre of the disk; poured as a continuous stream through a port situated above the centre of the disk or one that moves radially over a disk; or as heavy rain that floods the entire disk [16]. The disk may be stationary as the fluid is dispensed or may be rotating slowly and then accelerated to a relatively higher speed. The fluid spreads radially outwards under the influence of centrifugal force. Spinning is continued until the required thickness is attained. Rotation speeds vary from a few rpm to several thousand rpm depending on the spin coating

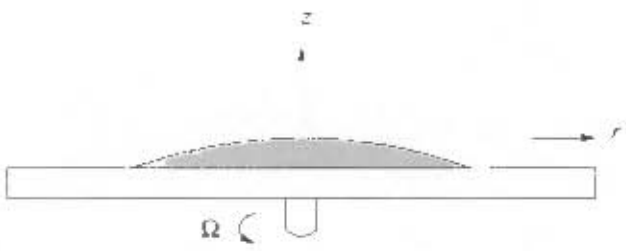

Figure 1.1: A pool of fluid at the centre of a disk.

application. The thickness of the resulting film is obviously dependent on rotation speed and viscosity of the fluid, among other things.

The uniformity and thinness of spin-coated layers far exceed those obtained by other methods, such as dip coating, which is one of the main reasons for the commercial usefulness of spin-coating [46]. Spin coating has been found to be a convenient and efficient means of coating planar solids with thin uniform films [77]. As a result, spin coating is a widely used procedure in the production of advanced electronic devices. For example, spin coating is used in the microelectronics industry to form thin films of photoresist, spin-on-glass and low dielectric constant materials on silicon wafers [58, 59]. It is also used to distribute thin layers of organic solvents, for cleaning purposes [82] as well as in several chemical engineering unit operations such as liquid atomization and liquid-liquid extraction [38]. This technique is also extensively used in the production of magnetic disk coatings, compact disks (CDs), antireflection coatings and television tube phosphor coatings [1, 46, 49, 61, 90] as well as in some nuclear instruments [42].

Determining the depletion rate of a lubricant coating on a rotating disk is useful for controlling product quality in the manufacture of magnetic hard disk devices for data storage [76]. When spin coating is used in the CD manufacturing process to make a glass master, in dye coating or to form a lacquer which acts as a protective layer of the metal layer on a CD [2, 3, 4], it is desirable that the fluid spreads and covers the entire substrate [1, 82] without fingering, therefore predicting how the fluid spreads would be useful in this process. In view of the foregoing commercial uses, it has long been recognized that predicting and controlling the rate at which a liquid film thins on a rotating disk is of great importance [42, 99].

We wish to derive mathematical models that will help us understand the behaviour of spin coated film profiles. In addition, we want to be able to predict the film thickness from the developed models, which is of paramount importance in many applications. We therefore aim to investigate the following:

- effects of surface tension and gravity on the shape and evolution of the film height,
- the role of the Coriolis force on the evolution of a thin rotating film,
- effects of including surface tension in non-Newtonian spin coating models.

The research objective of this thesis is to provide insight into spin coating of Newtonian and non-Newtonian fluids by addressing the preceding issues and to give a better understanding of how these affect the predicted profile and film thickness of spin coated films.

Recognising the important role surface tension plays in thin film flows, attempts have been made to include surface tension effects in Newtonian spin coating models [63, 66, 77, 82, 98], however very little has been done in the spin coating of non-Newtonian fluids. In both Newtonian and non-Newtonian spin coating, surface tension terms bring added complexity to the governing equations and are numerically demanding, which could be one of reasons why most studies neglect it in the governing equations. In this thesis, we will initially investigate the influence of surface tension and gravity on the height and final shape of the film in spin coating of Newtonian fluids. To do this, we will derive and solve numerically the governing equation which describes the shape of the film interface for axisymmetric flow of a thin Newtonian fluid layer under the influence of centrifugal force, surface tension and gravity. Comparisons of the variation of the film thickness along the radius for various values of surface tension and gravity effects will be carried out for some known Newtonian fluids.

The role of the Coriolis force on the evolution of a thin film of Newtonian fluid on a rotating disk has been investigated and attracted debate recently. Leshev and Peev [52], carry out an experimental and analytical investigation of a rotating thin layer of fluid. According to their findings, existing analytical results which neglect the Coriolis force in the radial direction and have centrifugal force as the only driving force [66, 75], predict film heights which are somewhat lower than experimental values near the centre of the disk. Their conclusion is that the Coriolis force must be included into the radial velocity equation to accurately describe film heights. However, a closer look at their work does reveal that the analysis leading up to this conclusion is flawed. Therefore, in Chapter 4 we investigate the role that the Coriolis force plays on the film height of spin coated films.

Most of the existing research on rotating thin films deals with Newtonian fluids. However, the majority of fluids used in industrial applications exhibit so-called 'non-Newtonian behaviour' [74]. For example, as previously mentioned CD manufacturing involves spin coating of photoresist onto a glass master, and acrylic plastic (lacquer) onto the metal layer of a CD to protect it from corrosion and damage [2, 5]. In the manufacture of CDR's, molded substrates are spin coated with an organic dye polymer later used as a recording layer [6, 7, 8]. The fluids used in these spin coating processes are all non-Newtonian fluids. As Ross *et al.* [79] point out, "many fluids encountered in industry and widely used as coating materials such as polymeric fluids, are non-Newtonian". In fact, coating fluids often consist of viscous suspensions which exhibit rather pronounced non-Newtonian behavior, especially at high concentrations [11]. Therefore, in Chapter 5 we will extend our analysis of spin coating models to non-Newtonian viscosity models and highlight how their behaviour differs from

that of Newtonian fluids. The viscosity models to be included in this investigation are commonly used models, namely Power-law, Ellis and Carreau.

Before proceeding with the objectives and aspirations of this study, we will give an overview of ideas that will be required in subsequent chapters. We will begin by reviewing existing research into Newtonian spin coating models and highlight some of the main findings of these investigations in Section 1.2. A review of some viscosity models that have been used to model non-Newtonian behaviour is given in Section 1.3. This is followed by a brief review of spin coating of non-Newtonian fluids in Section 1.4. The problem of a moving contact line is one common to driven thin films as a whole and one that cannot be avoided in modelling spreading films. Therefore, Section 1.5 reviews how the singularity arising at a moving contact line can be overcome when modelling moving fronts.

Thin liquid films are found everywhere from nature to technology and an understanding of their mechanics is important in many applications especially in industry [72]. In Chapter 2, as an introduction to the mathematical modelling of thin films, we will look at some applications of thin films in order to obtain a general understanding of the modelling involved in such applications. The starting point for modelling flow of thin films are the Navier-Stokes equations, which are essentially an application of Newton's law second law to the flow of fluids [10]. These equations are reduced using lubrication theory (Section 2.3). This approach was first developed by Reynolds in 1886 to describe motion of oil films in machine bearings [55]. Since then, it has become the norm in fluid-lubricated bearings and related devices involving thin films, so that the theory of such flows is commonly referred to as lubrication theory [83]. Considerable extensions of this theory have been made and it has often found application in thin film flows including those with a single free surface, such as spin coating.

1.2 The history of spin coating

The earliest mathematical analysis on the flow of a viscous fluid on a flat rotating disk is that of Emslie *et al.* [25]. In this well-known investigation, Emslie, Bonner and Peck considered spreading of a fluid on a disk with constant angular velocity. They developed a model of Newtonian flow on a rotating surface by balancing viscous resistance with centrifugal forces. Gravitational, Coriolis and capillary forces were neglected in this formulation, as was air-drag on the free surface. The model obtained from their analysis gives a simple relation between fluid flux and film height. Their theoretical results provide a simple estimate of

the distribution of the liquid as a function of time. The study reveals that spin coating of Newtonian fluids generally produces uniform films, regardless of the initial profile at the start of the rotation. Using contour surfaces for a number of initial distributions, they showed that an initially uniform film remains uniform after spinning, and an initially irregular film as a rule becomes uniform upon spinning. However in certain cases, rather than flattening, vertical wave fronts that progress radially outwards develop, but the film that is left behind is fairly uniform. Such a front has been found unstable and leads to the formation of radially advancing fingers [16, 82]. We look at the analysis of Emslie *et al.* in detail in Section 3.4 and what has made it so renowned.

Several authors have employed or extended the hydrodynamic equation of Emslie *et al.*, by considering other physical effects on spin coating such as solvent concentration and evaporation [48, 77, 86], induced air flow [59], surface roughness [35], Coriolis effects [60, 66, 67], surface tension [93, 98], non-Newtonian viscosity [11, 38, 49] *etc.*

The height of a thin film of liquid on a rotating disk under the influence of surface tension, gravity, evaporation, surface roughness and an induced air flow can be described by:-

$$\frac{\partial h}{\partial t} + \frac{1}{r}\frac{\partial}{\partial r}\left(\frac{r(h-h_\lambda)^3}{3}\left(C\frac{\partial}{\partial r}\left(\frac{1}{r}\frac{\partial}{\partial r}\left(r\frac{\partial(h-h_\lambda)}{\partial r}\right)\right) - B\frac{\partial(h-h_\lambda)}{\partial r} + r\right) + Ar^2(h-h_\lambda)^2\right) = -E\,, \tag{1.1}$$

where C is the inverse capillary number, B is the Bond number, E is the dimensionless evaporation, A is the dimensionless shear stress imposed by an external air flow. Surface roughness can be considered by prescribing the function $h_\lambda(r)$. Using (1.1) as a base equation, we will now briefly look at some of the physical effects that have been considered as an extension to the original model by Emslie *et al.* [25].

1.2.1 Evaporation

In the spin coating of viscous fluids, evaporation is often assumed to have negligible influence on the thinning of the film as compared to centrifugal draining. However, when modelling spin coating of a liquid consisting of a solid dissolved in a volatile solvent, it can be the competition between solvent evaporation and centrifugal force on film thinning that eventually determines the coating thickness. As a result, a number of investigations have been done that attempt to include the effects of solvent evaporation on the final film thickness [16, 37, 48, 58, 71, 77]. To simplify the problem, the evaporation rate is often modelled as

constant. The change in solvent concentration in the film due to evaporation and the effect of interfacial shear induced by the overlying gas phase are often assumed negligible as well.

One of the earlier studies that described a spin coating model based on the equations of Emslie *et al.* with the addition of the evaporation of the solvent was that of Meyerhofer [58]. Meyerhofer's analysis showed that the final film height for a spinning solvent with evaporation effects can be estimated analytically, assuming the transition from a radially dominated flow to one dominated by evaporation is abrupt. From the model equations, the film height could then be solved if the dependency on the viscosity and evaporation rate are known. Ohara *et al.* [71], in their investigation of the effect of evaporation on film thinning on a rotating disk, supported this approach, namely that at the start of the spin coating process, radial flow governs the film thinning but later, when the film is only a few microns thick, it is primarily reduced by the evaporation of the solvent. Lawrence [47] also comes to a similar conclusion on the sudden change from radially-dominated thinning to evaporation-dominated thinning in spinning films.

Reisfeld *et al.* [77] derived a spin coating model that included inertial forces and mass transfer (evaporation and absorption) at the free surface. According to their investigation, they found that evaporation from the free surface increases mass loss and decreases the film height monotonically to zero thickness in finite time, whereas in the absence of evaporation, the film decreases monotonically approaching zero thickness as $t \rightarrow \infty$.

From the preceding published works, it is generally agreed (and rather obvious) that evaporation from the free surface increases mass loss and causes the film to thin faster.

1.2.2 Induced air flow

Another extension to the Emslie *et al.* model has been the addition of an induced air flow. This was investigated by Middleman [59] who aimed to determine the degree to which an induced air flow affects the rate of thinning of a liquid on a rotating film. He employed the Emslie *et al.* approximation and considered the case when there was a significant radially directed shearing force generated by an induced air flow. While acknowledging that one cannot simply impose a shear stress on the spin coating problem, he argued that in the thin-film treatment, when viscous effects become very large, there may be conditions such that the radial velocity of the air near the free surface is sufficiently larger than the radial flow of the liquid. It is against this background, that his spin coating model included an induced air flow to determine how it helps the rate of thinning of the liquid film. The results showed

that an induced air-flow can enhance thinning considerably when compared with theory in which the air-flow is negligible. This is supported in part by Rehg & Higgins [76] who also considered the effect of an interfacial shear on the rate at which a rotating film thins. Their analysis suggests the effect is negligible for moderate spinning times but that it does have a 'measurable' effect on the rate of thinning for sufficiently long times.

1.2.3 Surface tension

Surface tension is a very important component in thin film applications such as paint films and various wetting or coating flows [70]. The governing equation for a rotating thin film with significant surface tension is

$$\frac{\partial h}{\partial t} + \frac{1}{r}\frac{\partial}{\partial r}\left[\frac{rh^3}{3}\left(C\frac{\partial}{\partial r}\left(\frac{1}{r}\frac{\partial}{\partial r}\left(r\frac{\partial h}{\partial r}\right)\right)+r\right)\right] = 0 \tag{1.2}$$

where C, the inverse capillary number, is the ratio of surface tension to viscous forces. Wilson *et al.* [98] consider among other things, spreading of a rotating thin film when surface tension is significant. Their results show profiles that develop the distinctive capillary ridge near the contact line in agreement with the experimental work of Melo *et al.* [57].

When modelling nearly flat film flows, the influence of surface tension is generally regarded as negligible. However, in the vicinity of a contact line or wherever there are waves, surface tension must be included at the moving front [93]. Surface tension has been found to play a stabilizing role, and reduce any non-uniformities of the free liquid surface. For example, its inclusion in the Emslie model prevents the formation of vertical wave fronts from developing [66].

Variation of temperature or concentration of surfactants, can introduce surface tension gradients into the governing equations [83]. Such gradients give rise to what are called Marangoni flows. The effect of Marangoni flows on non-spinning types of flows has been investigated, by a number of authors, see [39, 50, 54, 64, 69] for example.

1.2.4 Surface roughness

Roughness is known to retard radial film flow under the action of a radially directed shear stress. Yanagisawa [99] observed a retardation of the film thinning rate such that the time required to reduce the film height to one-third its initial value was increased by a factor of 2, in comparison to that for a smooth surface under otherwise identical conditions. The

resulting surface of the film tends not to be flat, but to conform to the topography of the underlying substrate [46]. This conformity can be observed from the appropriate governing equation

$$\frac{\partial(h-h_\lambda)}{\partial t}+\frac{1}{r}\frac{\partial}{\partial r}\left(\frac{r^2(h-h_\lambda)^3}{3}\right)=0\,, \tag{1.3}$$

i.e. an equation for the film thickness, other than one for the position of the free surface. Hwang & Ma [35] have also investigated the Emslie formulation by adding surface roughness. Their numerical solution indicates that surface roughness enhances lubricant retention, but if surface tension is neglected, surface roughness by itself does not increase lubricant retention.

1.2.5 Coriolis force

The effect of the Coriolis force on the evolution of a thin film of Newtonian fluid on a rotating disk has been investigated by a number of authors [52, 60, 66, 82]. Momoniat & Mason [60] include the Coriolis force in their axisymmetric analysis and conclude that the effect of the Coriolis force should be included fully, while neglecting the effect of the inertia. However, their numerics show that no visible Coriolis effect is observed. Schwartz & Roy [82], who study the formation of fingers in spin coating also argue that the Coriolis effect is of relative order Re and that other predictions of $\mathcal{O}(Re^2)$ are "as a result of the *ab initio* assumption that the motion is axisymmetric". However, assuming axisymmetry is a physically realistic asumption for some problems since certain deposition methods allow for it [68]. Myers & Charpin [66] carry out an axisymmetric analysis to show that the Coriolis term in the radial velocity equation appears at the same order as the inertia term and is therefore negligible at leading order. Following an experimental and analytical investigation, Leshev & Peev [52] conclude the Coriolis force must be included into the radial velocity equation to accurately describe film heights. They point out that existing analytical results which have centrifugal force as the only driving force, predict film heights which are lower than experimental values near the centre of the disk. In a subsequent paper, Myers & Lombe [67] show that the Coriolis force, together with the inertia term, may only enter as correction terms to the standard solution of the height of the free surface.

1.2.6 Discussion

Another very important factor that has been investigated in spin coating is the effect of non-Newtonian viscosity. However, the discussion of this will be deferred to Section 1.4,

following a brief introduction of non-Newtonian fluids and general characteristics of some non-Newtonian viscosity models in Section 1.3.

The preceding discussion indicates that many physical effects relevant to spin coating have been investigated in various studies. Solving a governing equation that includes all the various effects would be very difficult numerically or otherwise. However, a satisfactory understanding of the spin coating process can be achieved using a simplified lubrication analysis that neglects some of these. For example, in some spin coating applications, gravity is regarded as negligible when the liquid is very thin (only several hundred angstroms) [99]. Generally, its effect can be observed from the value of B in equation (1.1). If $B \ll 1$, then gravity effects can be assumed negligible. In spin coating of viscous liquids, inertial effects are unimportant except near the axis and can, in general, be neglected. To simplify the problem further, the centrifugal force may be taken to be essentially constant during spinning [76]. While recognising the importance of evaporation in modelling spin coating of volatile substances, several models are available that provide a basic understanding of its effect on the predicted film. Therefore, in our derivation of both the Newtonian and non-Newtonian models, not all the physical effects discussed in this section will be included.

1.3 Non-Newtonian fluids

Newtonian fluids have a shear stress τ that is proportional to the shear rate $\dot{\gamma}$ *i.e.*

$$\tau = \mu \dot{\gamma} \,, \tag{1.4}$$

where μ is a constant, known as the dynamic viscosity. Fluids with a non-constant viscosity are called non-Newtonian [10, 20]. Liquids with complex structures such as macromolecular fluids, polymeric fluids and soap solutions for example, fall into this category [87]. The term "non-Newtonian", however, is a very broad one which encompasses a large variety of fluids displaying so called non-Newtonian behavior in various ways. The two most common non-Newtonian properties on the spreading of a fluid are a shear-rate-dependent viscosity and normal stress effects [14]. We define the non-Newtonian viscosity analogously to the definition of viscosity for Newtonian fluids:-

$$\tau = \eta \dot{\gamma} \,, \tag{1.5}$$

where the fluid viscosity η is a function called the apparent viscosity, which varies for example, as a function of shear stress, shear rate, pressure or temperature [15]. However, we will focus

our attention on fluids that exhibit a shear-rate (or shear-stress) dependence of the viscosity, and in particular, shear-thinning fluids.

1.3.1 Shear-thinning fluids

Many foods transported and processed in industry behave as non-Newtonian fluids and in particular as shear-thinning fluids [87]. Shear-thinning fluids, also called pseudoplastic fluids, exhibit a shear-rate-dependent viscosity which decreases progressively with shear rate (see figure 1.2). Typically, these fluids flow more easily under shear as some internal structure in the material is broken down [17]. With this type of fluid, a popular relationship between $\dot{\gamma}$ and τ is the power-law, $\eta = \kappa|\dot{\gamma}|^{n-1}$. A fluid whose viscosity increases with shear stress is termed shear-thickening or dilatant, in this case $n > 1$ [87]. Shear-thickening is exhibited by fairly concentrated suspensions of very small particles, for example, corn-starch [15]. However, most polymer melts and solutions that exhibit a shear-rate-dependent viscosity are shear-thinning fluids, $n < 1$ [13]. Therefore our discussion of non-Newtonian fluids in this thesis will primarily be referring to the case $n < 1$. The case $n = 1$ describes Newtonian fluids. Figure 1.2 illustrates the relationship between shear stress and shear rate for the three cases:- shear-thickening, Newtonian behaviour, and shear thinning.

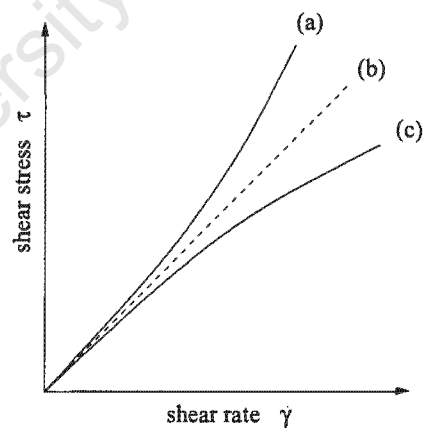

Figure 1.2: Shear stress vs. shear rate. (a) Dilatant or shear-thickening (b) Newtonian behaviour (c) Pseudoplastic or shear thinning

Examples of shear-thinning fluids include ketchup, mustard, fruit juice concentrates, honey, paint, slurries, shaving cream and shampoo [87]. Other shear-thinning fluids include molten polyethylene and polypropylene and solutions of carboxymethylcellulose (CMC) in water,

polyacrylamide in water and glycerin, and aluminium laurate in decalin and m-cresol [15]. Shear-thinning is also a characteristic of many polymers and suspensions used in engineering practice [79]. Many of these fluids only display shear thinning behaviour at intermediate shear rates. At very low and high shear rates their behaviour is basically Newtonian. For some of these fluids, the viscosity can change by a factor of $10^{-3} - 10^{-4}$ of the zero-shear-rate viscosity [14, 87]. To allow for such changes in viscosity with respect to the shear rate, the idea of the 'generalized Newtonian fluid' was introduced to describe the shear thinning [15]. When the relationship between $\log(\eta)$ and $\log(\dot{\gamma})$ is linear, the shear thinning is described by the power-law model. However, since the power-law does not describe the behaviour of most shear thinning fluids at very low and high shear rates, other models have been suggested to include these regions. These include the Ellis and Carreau models which have a Newtonian plateau at low shear rates. Unlike the Ellis model though, the Carreau model also has a Newtonian plateau at very high shear rates.

Several other empiricisms are available that attempt to describe the non-Newtonian viscosity for shear-thinning fluids. These include the Eyring model, Cross model and other modified ones such as the Carreau-Yasuda and Powell-Eyring models [15, 49]. However, their features are similar to the Ellis and Carreau models. Therefore, only three models will be discussed in the following section, namely power-law, Ellis and Carreau models.

1.3.2 Viscosity models

Power-law model

A simple mathematical model describing the shear thinning behavior of polymers is the power-law model. The viscosity of a power-law fluid (also known as Ostwald-de Waele fluid) can be expressed as [15, 87]:-

$$\eta = \frac{\tau}{\dot{\gamma}} = \kappa|\dot{\gamma}|^{n-1} , \tag{1.6}$$

where $\dot{\gamma}$ is the shear rate, κ is a measure of consistency of the fluid, and n is a power-law index or a measure of the degree of non-Newtonian behavior. Typical values of n for macromolecular fluids commonly modelled as shear thinning fluids are in the range of $0.15 - 0.6$ [15].

The constitutive model (1.6) gives $\eta \to \infty$ as $\dot{\gamma} \to 0$ when $n < 1$, *i.e.* the viscosity goes to infinity at vanishing shear rates [38]. When $n > 1$, $\eta \to 0$ as $\dot{\gamma} \to 0$. Both cases are unrealistic and as a result, the power-law does not accurately describe the portion of the

viscosity curve near $\dot{\gamma} = 0$. The usefulness of the power-law model is derived from the fact that several analytical solutions are possible because of its simplicity. In addition, many practical flow problems occur at moderate-to-high shear rates where the power-law model gives a reasonable fit of viscosity data [49]. The power-law model is, "without doubt the most well known and widely used empiricism in engineering work; many specific flow problems and heat transfer problems have been solved using it and the results have proven to be useful." [15]. Therefore, the power-law model can be useful in accurately describing the behavior of some polymeric liquids at moderate-to-high shear rates.

Carreau model

Another especially useful model for non-Newtonian fluids is the Carreau model, with non-Newtonian viscosity described mathematically as [87]:-

$$\eta = \eta_\infty + (\eta_o - \eta_\infty)\left(1 + (\lambda\dot{\gamma})^2\right)^{(n-1)/2} , \tag{1.7}$$

where η_o is the zero-shear-rate viscosity (or Newtonian viscosity), λ is a time constant, $\dot{\gamma}$ is the shear-rate, n is the power-law exponent and the quantity η_∞ represents the limiting viscosity at very large shear rates. Unlike the power-law model, this model predicts a fluid whose viscosity approaches a constant, η_o , at low shear rates. The Carreau model therefore, becomes Newtonian as shear rates approach zero. At moderate shear rates, the Carreau model basically reduces to a power-law model with $\kappa = \eta_o\lambda^{n-1}$ and at very high shear rates becomes Newtonian again with viscosity $\eta \to \eta_\infty$ (which is often taken as 0 for practical purposes as it is very small in magnitude compared to the zero-shear-rate viscosity [15, 65]). The viscosity of many polymer solutions can be adequately fitted by the Carreau model [38]. The Carreau model is considerably more difficult to use than the power-law as one cannot obtain an analytical expression describing the fluid film height. Nevertheless, this model describes the viscosity data well enough for most engineering calculations [14].

For most polymer solutions and polymer melts, n lies between 0 and 1 [15].

Ellis model

The Ellis model is another commonly-used model that overcomes some of the shortfalls of the power law model. This model gives the viscosity, η, as a function of the shear stress, τ.

The constitutive equation is given by [15, 56]:-

$$\frac{1}{\eta} = \frac{1}{\eta_0}\left(1 + \left|\frac{\tau}{\tau_{1/2}}\right|^{\alpha-1}\right) , \tag{1.8}$$

where η_0 is the viscosity at zero shear stress, τ the shear stress, $\tau_{1/2}$ the shear stress at which the viscosity is reduced by a factor of half, and α is a power law index. The Ellis model, like the Carreau model describes a liquid that at low levels of stress flows at constant viscosity, while at moderate to high stress levels displays power-law shear thinning behavior [49, 56].

Figures 1.3 and 1.4 illustrate the viscosity predicted by the three preceding non-Newtonian viscosity models for Polyethylene Oxide and Hydroxethylcellulose. The data is taken from Myers [65], who uses data sets from [15, 20].

Figure 1.3 shows the viscosity of Polyethylene Oxide in water. For low shear rates the Ellis model predicts the same viscosity as the Carreau model while the power-law is remarkably different, with the viscosity tending to infinity at vanishing shear rates. Apart from that, the three models predict similar viscosity for moderate to high shear rates.

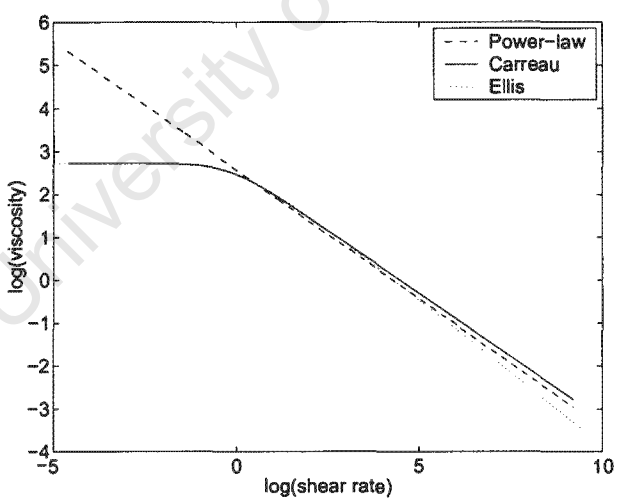

Figure 1.3: Shear rate vs viscosity for Polyethylene Oxide.

Similarly, figure 1.4 shows the viscosity of 0.5% Hydroxethylcellulose predicted by the three models. At low shear rates, the Carreau and Ellis models predict the same Newtonian plateau even though they differ slightly in the transition region from power-law to Newtonian behaviour. Once more, the power-law predicts viscosity that tends to infinity at vanishing

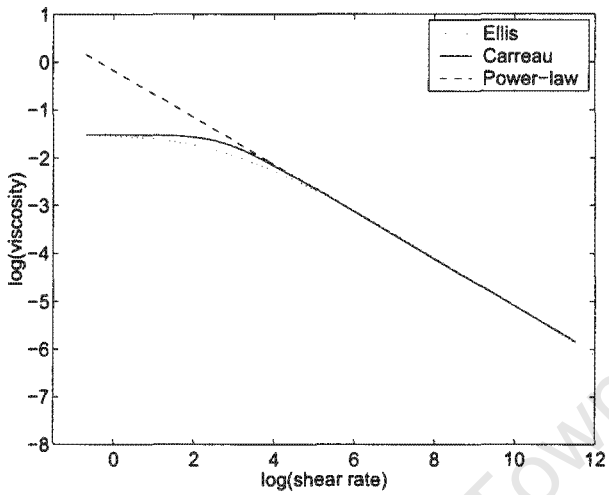

Figure 1.4: Shear rate vs viscosity for 0.5% Hydroxethylcellulose.

shear rates. In both graphs, the second Newtonian plateau for the Carreau model is not included as η_∞ has been set to 0.

Figures 1.3 and 1.4 are just two examples where the three models predict similar viscosity in the 'power-law' region but this is not always the case. The two graphs are included to highlight the main difference in behaviour at very low shear rates between the power-law model and the other two models as this is relevant to spin coating as we shall see later.

We will now briefly review what has been done in previous studies with regard to spin coating using the preceding non-Newtonian viscosity models.

1.4 Spin coating with non-Newtonian fluids

Following the pioneering analysis of Emslie *et al.* [25], a natural extension to their work is the investigation of the behavior of non-Newtonian fluids on a rotating substrate.

The flow of a power-law fluid on a rotating disk (surface tension and gravity neglected) was first investigated by Acrivos *et al.* [11] who obtained a method-of-characteristics solution for lubrication flow. Their analysis showed that, in general, uniform films cannot be obtained from spinning a power-law fluid on a disk. An initially irregular film profile will remain non-uniform even after long spinning times, while an initially uniform film will lose its uniformity. Another feature observed in their analysis of a power-law fluid on a rotating

disk, is the unrealistic film profiles (spikes) at the centre of the disk, which are a result of the predicted infinite viscosity at the centre (where $\dot{\gamma} = 0$) forcing the liquid to 'remain' stationary.

Jenekhe [36] suggested the use of the more realistic Carreau model to describe the fluid viscosity, after showing that polyamic acid and polyimide solutions, exhibit Newtonian behavior below a critical shear rate. Jenekhe & Schuldt [38] later considered the spin coating flow of a fluid described by the Carreau model, with surface tension and gravity neglected. They obtained numerical solutions to the flow equations and observed a transition from power-law to Newtonian behaviour as the film became thinner. Their results show that for Carreau fluids, initially non-uniform films will become uniform after long spinning times. Initially uniform films will lose their uniformity but then become uniform after sufficient spinning times. At large shear rates however, the Carreau model profiles will become more like power-law profiles [38], but without the spikes at the centre.

Lawrence & Zhou [49] also consider spin coating of non-Newtonian fluids with evaporation at the free surface. In their investigation, they use rheological models such as the Ellis and Carreau-Yasuda models, which show Newtonian behaviour at low shear rates with a transition to power-law shear thinning at moderate rates. In their work, they present a theoretical description of the flow and diffusion in a non-Newtonian fluid film, incorporating the effects of shear thinning. They neglect surface tension and gravity effects in their analysis but instead consider the effects of rapid and slow evaporation. According to their findings, for fluids which show shear thinning at intermediate shear rates, the final film thickness is similar to the Newtonian case. They also analysed the effect of prematurely stopping the spinning process and give an equation that relates this to the final film thickness obtained.

A number of papers on non-Newtonian spin coating have concentrated on the effects of evaporation especially on polymer resists in order to determine the dependence of the final film thickness on the processing parameters [16, 21, 27, 48], see Section 1.2.1.

In general, there are a small number of investigations into the spin coating of non-Newtonian fluids and therefore, we wish to look at this in more detail in this thesis.

1.5 Contact lines

1.5.1 Contact-line motion for Newtonian fluids

A standard problem encountered in thin film flow modelling is that of the moving contact line [22, 30, 63]. This occurs when the leading edge of the film, where $h = 0$, moves over a dry substrate. The basic problem is due to the conflict between applying a no-slip boundary condition on $z = 0$ and allowing the front at $h = z = 0$ to move with a non-zero velocity. This gives rise to a non-integrable singularity of the shear stress at the leading edge [24, 34]. The formulation of the problem must therefore be relaxed in such a way that the singularity is removed. Since a number of flow situations discussed in subsequent chapters will involve a moving contact line, we will now discuss two common approaches to remove the singularity.

Slip condition

One method that is used to eliminate the singularity is the replacement of the no-slip boundary condition by a slip one in the immediate vicinity of the moving contact line [32, 84, 85]. Any slip condition $u = f(h)u_z$, (where u is the fluid velocity in the z direction and z is the coordinate in the direction normal to the substrate) is sufficient to remove the infinite-force singularity [22]. In practice, the most common slip laws used are [64]:

$$u = \frac{\alpha}{3h}u_z \ , \qquad u = \beta u_z \ , \tag{1.9}$$

where α and β are constant slip coefficients, $\alpha, \beta \ll 1$. With these slip laws, the term $h^3/3$ in (1.2) will be modified to

$$\frac{h^3 + \alpha h}{3} \ , \qquad \frac{h^3}{3} + \beta h^2 \ ,$$

for the two slip models. The slip condition is formulated in such a way that it only significantly affects the dynamics of the flow in the vicinity of the contact line where the film thickness is 'small', $h \sim \sqrt{\alpha}$, $h \sim \beta$ [64]. Imposing a slip condition allows the free surface to make contact with the substrate. This often requires imposing a contact angle at the leading edge, as one of the boundary conditions. This contact angle is often assumed to be related to the contact-line speed by some law, such as Tanner's law, see [23, 30, 32, 84, 98] for example.

Precursor film

An alternative method for dealing with moving contact lines is to impose a very thin precursor film or wetting layer (whose thickness h_p is assumed constant) ahead of the main flow. This has the advantage of removing the difficulty arising at the contact line so that the classical no-slip boundary condition can be applied everywhere along the substrate [63]. The addition of a precursor film is not unrealistic since precursor films are often a prerequisite in some industrial coating applications [64]. When the aim is to study the way in which an extra quantity of fluid moves down an already wet wall, such an assumption is actually required [63]. In addition, experiments on advancing contact lines have been reported that indicate the presence of a precursor layer of fluid ahead of the easily observable contact line for some fluids [24, 63].

When using a precursor layer model, the film is assumed infinite in the sense that it extends infinitely on the plane in question, with finite but very small thickness. The "no-slip" boundary condition can then be applied at every point along the plane. The precursor film allows the movement of the front and the contact line problem is eliminated. Inclusion of a precursor film does not affect the governing equation for the fluid flow and gives similar results to those obtained using a slip model [85]. Experimental data on spreading drops suggests the precursor film height being in the range $1 - 100\,\text{nm}$ [81].

Other approaches

Other approaches to modelling the advancing contact-line problem include what has been observed in experimental studies for some liquids, namely that the spreading of some viscous liquids over the surfaces of solids can be modelled by rolling [24]. This approach is investigated analytically by Shikhmurzaev [84], where fluid is modelled rolling in the vicinity of the contact line. In this way, material that is located on the free surface will eventually reach the solid surface in a finite time, and hence the fluid front moves without slipping.

It is interesting to note that when performing numerical computations, it is possible to compute the free surface profiles by ignoring the singularity at the contact line altogether. Moriarty and Schwartz [62] point out that this is because slip is introduced implicitly by the numerical scheme, as a result of solving the governing equation at discrete points, with the implicit numerical slip being a function of the numerical grid-spacing. In other words, the no-slip boundary condition would be imposed at a point close to the contact line but

not at the contact line itself. However, the singularity becomes evident in that convergence may not be achieved by refining the grid [62]. Since we require our numerical scheme to converge, this is not satisfactory. Therefore, the simple approach of a precursor film model will be assumed throughout this thesis.

1.5.2 Contact-line motion for shear-thinning liquids

For both Newtonian and shear-thinning fluids, the stress is singular at the contact point. However, for shear-thinning fluids the difficulty of the moving contact lines does not always arise since when the shear stress tends to infinity, the effective viscosity tends to zero [13, 95]. In effect this can remove the inconsistency between the no-slip boundary condition and the requirement of contact-line movement. Consequently, the no-slip boundary condition could still be retained in the vicinity of the contact line, while allowing the contact line to move on the surface.

Kataoka & Troian [40] point out "singularities of the flow often signal some break down in the assumptions of the model". For shear thinning fluids, as long as a fluid exhibits power-law behaviour at high shear rates, it is argued that no singularity arises in this case [13]. For a fluid exhibiting a Newtonian plateau at high shear rates like the Carreau model, methods discussed in Section 1.5.1 would have to be applied to avoid any singularity at the contact line [41, 95].

Chapter 2

Mathematical modelling of thin film flows

2.1 Introduction

The aim of this chapter is to introduce the mathematical modelling of thin films. A thin film is generally one in which the characteristic thickness of the film H (in the z-direction), is assumed to be much smaller than the characteristic length of the film L (in the x-direction, and y-direction if relevant) [10, 69]. The flows that will be considered are therefore the ones that take place predominantly in the direction of the longer dimensions under the action of some external force.

A thin film of viscous fluid near a boundary is typically characterised by laminar flow. Laminar flow is a type of flow in which individual particles of fluid travel smoothly along well-defined paths without crossing those of neighbouring particles [91]. Laminar flow is characterised by low Reynolds numbers (< 2000) [55]. The Reynolds number, Re, is a dimensionless quantity defined as $Re = UL/\nu$, which is equivalent to the ratio of inertia forces to viscous forces, where U is the characteristic velocity of the flow, L the characteristic length scale and ν the kinematic viscosity of the fluid [83]. In laminar flow viscous forces are predominant while in turbulent flows, inertia forces dominate.

Viscous flow is described by the Navier-Stokes equations which have no general solution. However, the equations may be simplified using what is known as lubrication theory (sometimes called the long-wave approximation [82]). This is described in Section 2.3. This

approach was originally developed to describe the motion of oil films in bearings and hence became known as 'lubrication theory' [55].

In Section 2.3, a non-dimensional analysis is carried out to show how the Navier-Stokes equations can be reduced using lubrication theory. Non-dimensionalisation is an important procedure which provides insight into the relative magnitudes of the various terms in the equations (provided the scales are chosen appropriately) [70]. This is then exploited by neglecting terms that are not significant. This results in a simplified and more manageable form of the Navier-Stokes equations, which can then be solved analytically or numerically depending on the problem at hand. The focus of this thesis is on thin film flows with a single free surface. However, to illustrate the appropriate equations and modelling involved in lubrication theory, in Section 2.4 we will present two problems involving thin films with no free surface, namely Poiseuille and Couette flows.

Lubrication theory, which was first used to describe motion of oil films in bearings, has since been extended to other problems involving thin films in general, including those with a free surface. In Section 2.5, we investigate standard models for a driven film with a single free surface. We also demonstrate the use of a precursor film to overcome the contact line singularity. This analysis paves the way for our subsequent analysis on film spreading on rotating disks.

2.2 Navier-Stokes equations for an isoviscous fluid

The Navier-Stokes equations govern the motion of a viscous fluid. For the moment we will focus on Newtonian fluids, *i.e.* fluids in which the shear stress is proportional to the velocity gradient, where the proportionality coefficient μ (a constant) is a property of the fluid known as the dynamic viscosity [55, 70]. For an incompressible isoviscous fluid, the Navier-Stokes and continuity equations may be written in vector form as [10] :-

$$\rho\left(\frac{\partial \mathbf{u}}{\partial t} + (\mathbf{u}\cdot\nabla)\mathbf{u}\right) = -\nabla p + \mu\nabla^2\mathbf{u} + \mathbf{F} \tag{2.1}$$

$$\nabla\cdot\mathbf{u} = 0 \tag{2.2}$$

where ρ is the density of the fluid, p is the pressure, $\mathbf{u}$ is the velocity vector and $\mathbf{F}$ is the body force per unit mass. Equation (2.1) results from conservation of momentum which corresponds to Newton's second law for incompressible fluids. The term in large brackets on the left hand side of equation (2.1) represents the acceleration while the right hand side

is the sum of the forces (per unit volume) acting on the particle:- the pressure gradient and viscous resistance while the term **F** represents the contribution of the body forces such as gravity and centrifugal force. The continuity equation or mass-conservation equation (2.2), represents the principle of mass conservation, which states that the mass flux entering a control volume exactly balances the outgoing mass flux when there are no mass source or sink terms [55]. We are now going to simplify equation (2.1) using lubrication theory.

2.3 Lubrication theory

The basic assumption of lubrication theory is that inertia (and some viscous) terms in the Navier-Stokes equation can be neglected, hence simplifying the problem. This reduction of Navier-Stokes equations using lubrication theory therefore allows us to tackle problems that would otherwise be solved only numerically. This simplification is valid provided [10]:

- the square of the aspect ratio is small, $\delta^2 \ll 1$
- the reduced Reynolds number is small, $\delta^2 Re \ll 1$

where $\delta = H/L$. It is important to note that it is not necessary for the Reynolds number to be small but only that the reduced Reynolds number $\delta^2 Re$ be small [70]. Flows at very low Reynolds numbers ($Re \ll 1$) are also called creeping flows [83].

Suppose we have a two-dimensional thin film driven by a pressure gradient. The components of the Navier-Stokes equations in the x and z directions are:

$$\frac{\partial u}{\partial t} + u\frac{\partial u}{\partial x} + w\frac{\partial u}{\partial z} = -\frac{1}{\rho}\frac{\partial p}{\partial x} + \nu\left(\frac{\partial^2 u}{\partial x^2} + \frac{\partial^2 u}{\partial z^2}\right) \tag{2.3}$$

$$\frac{\partial w}{\partial t} + u\frac{\partial w}{\partial x} + w\frac{\partial w}{\partial z} = -\frac{1}{\rho}\frac{\partial p}{\partial z} + \nu\left(\frac{\partial^2 w}{\partial x^2} + \frac{\partial^2 w}{\partial z^2}\right) \tag{2.4}$$

where $\nu = \mu/\rho$ is the kinematic viscosity, (u, w) are the velocity components in the x and z directions, respectively. The continuity equation (2.2) takes the simple form

$$\frac{\partial u}{\partial x} + \frac{\partial w}{\partial z} = 0\ . \tag{2.5}$$

Non-dimensionalisation

Let H be the characteristic thickness of the layer and L the characteristic length scale. Let U and W be the velocity scales in the x and z directions, respectively. The vertical velocity

scale W is obtained by balancing the terms in the continuity equation

$$\frac{U}{L}u'_{x'} + \frac{W}{H}w'_{z'} = 0\ . \tag{2.6}$$

If we write

$$\delta U u'_{x'} + W w'_{z'} = 0\ , \tag{2.7}$$

then a naive approximation would suggest $w'_{z'} = 0$, which, after applying the no-slip boundary condition $w'(0) = 0$, then indicates $w' = 0$. We therefore conclude that the only reasonable scaling is $W = HU/L$. Time is scaled by L/U.

The dimensionless variables (denoted by primes) are related to their dimensional counterparts by:-

$$x = Lx' \qquad z = Hz' \qquad u = Uu' \qquad w = \left(\frac{HU}{L}\right)w' \qquad t = \left(\frac{L}{U}\right)t' \qquad p = Pp'\ .$$

On substituting the non-dimensional variables into the governing equations and dropping the primes, we have

$$\delta^2 Re\left(\frac{\partial u}{\partial t} + u\frac{\partial u}{\partial x} + w\frac{\partial u}{\partial z}\right) = -\frac{PH^2}{\mu UL}\frac{\partial p}{\partial x} + \delta^2\frac{\partial^2 u}{\partial x^2} + \frac{\partial^2 u}{\partial z^2}\ , \tag{2.8}$$

$$\delta^4 Re\left(\frac{\partial w}{\partial t} + u\frac{\partial w}{\partial x} + w\frac{\partial w}{\partial z}\right) = -\frac{PH^2}{\mu UL}\frac{\partial p}{\partial z} + \delta^4\frac{\partial^2 w}{\partial x^2} + \delta^2\frac{\partial^2 w}{\partial z^2}\ . \tag{2.9}$$

From equations (2.8) and (2.9), we can see that the pressure scale, P, is the standard one for lubrication theory $P = \mu UL/H^2$ [66].

Using the lubrication assumptions, equations (2.3) and (2.4) are thus reduced to obtain the leading order terms:-

$$0 = -p_x + u_{zz}\ , \tag{2.10}$$

$$0 = -p_z\ . \tag{2.11}$$

To help us appreciate the usefulness of the lubrication simplification, we will now consider three simple and well known problems of fluid dynamics in which lubrication theory is applied:- forced flow between parallel plates, flow induced by the movement of one of a pair of parallel planes and gravity-driven flow of a liquid down an inclined or vertical plane with one free surface.

2.4 Lubrication with two fixed surfaces

A common lubrication problem involves flow in a narrow gap between two plates, one of which is moving with constant velocity U. Even if both plates are moving, this assumption is still valid if both velocities are considered relative to one of the boundaries which is then supposed to be at rest [55]. This problem can be solved in one of two ways: as unidirectional flow or as a lubrication problem to obtain equations (2.10) and (2.11).

In the first instance, we assume parallel plates located at $z = 0, 1$. Equations (2.10) and (2.11) must be solved subject to boundary conditions

$$u = 1 \quad \text{at} \quad z = 0\,; \qquad u = 0 \quad \text{at} \quad z = 1\,. \tag{2.12}$$

Integrating (2.10) with respect to z and imposing boundary conditions (2.12) we have

$$u = \frac{1}{2} p_x \left(z^2 - z\right) + 1 - z\,. \tag{2.13}$$

We are interested in the total flux or discharge through the region in between the plates since it is often simpler to measure the flux than the pressure gradient. The total volume flow rate per unit width between the two plates is given by

$$Q = \int_0^1 u \, \mathrm{dz} = -\frac{p_x}{12} + \frac{1}{2}\,. \tag{2.14}$$

Therefore, from equation (2.14) we can express the pressure gradient p_x in terms of the total volume flow rate Q, and use it to eliminate p_x in (2.13).

Couette flow

Equations (2.13) and (2.14) show that flow may occur without a pressure gradient, provided one boundary is moving. Such flow, caused by the movement of a boundary is known as Couette flow [55]. The velocity is then a simple shear, $u = 1 - z$, and the flux is given by $Q = 1/2$.

Poiseuille flow

When both plates are fixed and the flow is caused by a pressure difference, then we have Poiseuille flow [10, 45]. Since $U = 0$ at $z = 0$, equation (2.13) now reduces to

$$u = \frac{1}{2} p_x \left(z^2 - z\right)$$

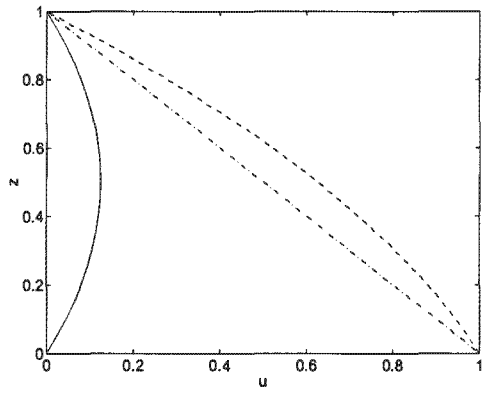

Figure 2.1: Typical velocity profiles for Poiseuille flow and Couette flow.

and the flux is given by $Q = -p_x/12$.

Figure 2.1 shows typical velocity profiles for Poiseuille flow (solid), Couette flow (dash-dot) and a combination of the two (dash) with $p_x = 0$ or 1 and $U(0) = 0$ or 1. The resulting velocity profile for Poiseuille flow is parabolic (the maximum velocity occurs at the centre) while for Couette flow, the maximum velocity occurs at the moving boundary. When you have both a pressure gradient and a moving boundary, where the maximum velocity occurs depends on which one dominates the flow.

Slider bearing

A typical example of Couette flow found in the lubrication of machinery is a slider bearing [10, 83], which consists of a thin layer of viscous fluid confined between two nearly parallel plates that are in relative tangential motion (see figure 2.2).

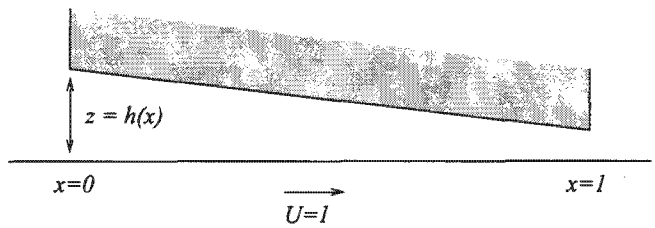

Figure 2.2: Slider bearing.

The top plate is called the slipper and the bottom plate is called the bearing plate. The

slipper is considered fixed while the bearing plate ($z = 0$) moves with velocity $U = 1$. The slipper is inclined to the bearing plate in the direction of motion as shown in the figure.

Suppose $h(x)$ varies linearly between two values say h_1 at $x = 0$ and h_2 at $x = 1$, with $h_2 < h_1$. Since the bearing is linear, an expression for h is given by

$$h(x) = (h_2 - h_1)x + h_1 \ . \tag{2.15}$$

This problem requires a slight modification of the analysis leading up to equation (2.13) to account for a non-constant height.

Equations (2.10) and (2.11) must be now solved subject to boundary conditions

$$u = 1 \quad \text{at} \quad z = 0 \ , \qquad u = 0 \quad \text{at} \quad z = h(x) \ , \tag{2.16}$$

to give

$$u = \frac{1}{2}p_x(z^2 - zh) + 1 - \frac{z}{h} \ . \tag{2.17}$$

Using the equation of continuity, and assuming no fluid escapes on the sides, then the volume flux Q across all sections must be the same:-

$$Q = \int_0^{h(x)} u \, \mathrm{d}z = \frac{h}{2} - \frac{h^3 p_x}{12} \ . \tag{2.18}$$

For a bearing subject to ambient pressure, p_a, at either end, the boundary conditions on p are:-

$$p\,(0) = p_a \qquad \text{and} \qquad p\,(1) = p_a \ . \tag{2.19}$$

Equation (2.18) can be expressed in terms of p_x and integrated with respect to x to obtain

$$\frac{p - p_a}{6} = \int_0^x \frac{1}{h^2(s)} \, \mathrm{d}s - 2Q \int_0^x \frac{1}{h^3(s)} \, \mathrm{d}s \ , \tag{2.20}$$

where s is a dummy variable. From our boundary conditions (2.19) we find

$$Q = \int_0^1 \frac{1}{h^2(s)} \, \mathrm{d}s \Big/ 2 \int_0^1 \frac{1}{h^3(s)} \, \mathrm{d}s \ .$$

Substituting for h from equation (2.15) leads to

$$Q = \frac{h_1 h_2}{h_1 + h_2} \ ,$$

and therefore

$$\frac{p - p_a}{6} = \frac{(h_1 - h)(h_2 - h)}{(h_2^2 - h_1^2)h^2} \ , \tag{2.21}$$

from which the pressure p generated by the system can be calculated. The term on the right hand side of (2.21) is positive since $h_2 \leq h(x) \leq h_1$. Consequently, when lubricant is forced into a converging bearing, there is a net upward force on the slipper to support a load therefore keeping the surfaces separate, which is the whole essence of lubrication [55]. Further, since the pressure scale

$$p = \frac{\mu U L}{H^2} \sim \frac{1}{H^2} ,$$

we see that for non-zero p, very high loads may be supported by thin films.

2.5 Two-dimensional film with a single free surface

Thin liquid films with a free surface are found in many industrial processes and natural phenomena and consequently have been widely studied, see [23, 33, 44, 63, 69, 80, 92] for example. Examples include the motion of raindrops on a window pane, spread of a fluid drop on a surface or molten lava over the ground and coating processes (such as spin coating) in the manufacturing of various products [64, 83]. Typically, these flows are termed draining or coating flows since they describe the motion of spreading films under a driving force [94].

The aim of this section is to show how to model a free surface flow and how to deal with contact lines. It is well known that driven spreading films bring the added difficulty of moving contact lines. One way of overcoming the problem of the singularity that arises at the moving front is by having a very thin precursor film, h_p, ahead of the main flow (see Section 1.5). In this section, we derive a third-order equation that can be used to describe draining over a precursor layer and solve this numerically both as an initial value problem and a boundary value problem.

We now derive the governing equation for a thin liquid film of a viscous fluid on an inclined plane under the influence of gravity and surface tension. We define the positive x-axis in the direction of the flow. The physical configuration is shown in figure 2.3.

The moving front is characterised by a capillary ridge (where the fluid piles up), which forms just behind the fluid front or contact line. The equilibrium region is the region far behind the moving front where the film has an approximately constant height.

We start our analysis with the lubrication equations derived in Section 2.3, with the inclusion of a body force:-

$$0 = -p_x + u_{zz} + B\sin\phi \tag{2.22}$$

$$0 = -p_z - \delta B\cos\phi , \tag{2.23}$$

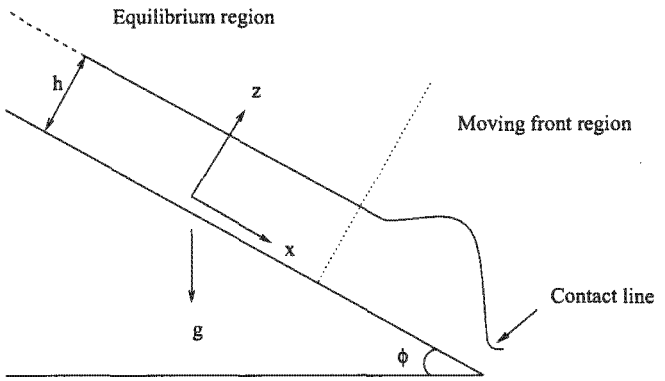

Figure 2.3: Schematic illustration of a thin film on a slope.

where $B = gH^2/\nu U$, is the Bond number - the ratio of gravity to viscous forces [10] and ϕ is the angle of inclination of the plane. These equations must be solved subject to no-slip at the solid-liquid interface $z = 0$

$$u = w = 0 \, . \tag{2.24}$$

At the free surface $z = h(x,t)$, there is zero shear stress

$$u_z = 0 \, , \tag{2.25}$$

and the standard kinematic condition holds

$$w = \frac{\partial h}{\partial t} + u\frac{\partial h}{\partial x} \, . \tag{2.26}$$

Boundary condition (2.25) denotes that any friction between the liquid surface and ambient air can be neglected and the kinematic condition (2.26) ensures that fluid particles at the free surface stay on the free surface, *i.e.* there is no evaporation or condensation, see [10] for example. In addition, the pressure jump at the free surface is expressed by $p = p_a - \sigma\kappa$, where p_a is the ambient pressure above the surface and κ is the curvature. Since the curvature of a thin film is small, $|\partial h/\partial x| \ll 1$, we may approximate the curvature by [70, 83]:-

$$\kappa \; = \; \frac{h_{xx}}{(1+h_x^2)^{3/2}} \; \approx \; h_{xx} \, . \tag{2.27}$$

The non-dimensional pressure is then expressed as $p = p_a - Ch_{xx}$, where $C = \sigma\delta^3/\mu U$ is the inverse capillary number which relates surface tension to viscous forces. Integrating (2.23) with respect to z and using the condition that $p = p_a - Ch_{xx}$ on the free surface ($z = h$), gives the pressure

$$p = p_a - \delta B\cos\phi(z-h) - Ch_{xx} \, . \tag{2.28}$$

Differentiating (2.28) with respect to x we have,

$$p_x = \delta B h_x \cos\phi - C h_{xxx} \ . \tag{2.29}$$

This shows p_x is a function of x only. Integrating (2.22) twice and imposing the necessary boundary conditions gives the velocity along the plane,

$$u = \frac{1}{2}(p_x - B\sin\phi)(z^2 - 2hz) \ . \tag{2.30}$$

Integrating the continuity equation $u_x + w_z = 0$, and using Leibnitz's rule and the kinematic boundary condition (2.26) gives

$$\frac{\partial h}{\partial t} + \frac{\partial}{\partial x}\int_0^h u \, \mathrm{d}z = 0 \ . \tag{2.31}$$

Integrating and simplifying the above equation using equations (2.30) and (2.29) leads to

$$h_t + \frac{\partial}{\partial x}\left(\frac{h^3}{3}\left(B\sin\phi - \delta B h_x \cos\phi + C h_{xxx}\right)\right) = 0 \ . \tag{2.32}$$

Therefore, we have reduced the governing equations of the flow to a single fourth-order non-linear equation for the prediction of the film thickness, under the action of gravity and surface tension. This well known equation is discussed in detail in the reviews of Myers [64] and Oron *et al.* [72].

In the equilibrium region, the film height is approximately constant and steady and so the solution of equation (2.32) is simply h equal to some constant, which is determined by the known flux. Due to the non-dimensionalisation, the constant may be set to 1. The region of primary interest is therefore the moving front region, where the capillary ridge forms. We will now focus on the solution of equation (2.32) in this region.

2.6 Flow in the moving front region

For simplicity we now consider a fluid film that is draining down a vertical plane ($\phi = \pi/2$). This removes the term involving $\cos\phi$ and equation (2.32) reduces to

$$h_t + \frac{\partial}{\partial x}\left(\frac{h^3}{3}\left(B + C h_{xxx}\right)\right) = 0 \ . \tag{2.33}$$

Even when the plane is not necessarily vertical, the term $\delta B h_x \cos\phi$ is negligible in comparison to $B\sin\phi$, except at very low angles of inclination and can therefore, in general, be neglected.

We are mainly interested in the front region which describes the shape of the film height as it advances over the substrate. We consider the moving front as a wave, travelling at a constant velocity $\tilde{U}$ (which is not necessarily the same as the velocity scale U), in the x-direction and set a new co-ordinate $\zeta = x - \tilde{U}t$. Using the substitution $h(x,t) = h(x - \tilde{U}t) = h(\zeta)$, in equation (2.33) leads to

$$-\tilde{U}h_\zeta + \frac{\partial}{\partial\zeta}\left(\frac{h^3}{3}\left(B + Ch_{\zeta\zeta\zeta}\right)\right) = 0\ . \tag{2.34}$$

We define the equilibrium region as the region far from the moving front where the height is uniform, for simplicity this may be set to 1. The moving front is the region just behind the contact line as the film advances on the plane. The boundary conditions for this region are

$$h \to 1 \qquad \text{as} \qquad \zeta \to -\infty \tag{2.35}$$

$$h \to h_p \qquad \text{as} \qquad \zeta \to +\infty\ . \tag{2.36}$$

Integrating (2.34) we have

$$\frac{h^3}{3}\left(B + Ch_{\zeta\zeta\zeta}\right) = \tilde{U}h + I\ , \tag{2.37}$$

where I is a constant of integration. Applying boundary conditions (2.35) and (2.36) we get

$$\begin{aligned} I &= -\tilde{U} + \frac{B}{3} \\ I &= -\tilde{U}h_p + \frac{B}{3}h_p^3 \end{aligned} \tag{2.38}$$

which together give the value of $\tilde{U}$ as

$$\tilde{U} = \frac{B}{3}\Lambda \qquad \text{where} \qquad \Lambda = 1 + h_p + h_p^2\ . \tag{2.39}$$

Note that the front speed depends on both gravity and the precursor height. As h_p decreases, the velocity also decreases as it becomes more difficult for the fluid to move.

Substituting this value of $\tilde{U}$ in (2.38) to find I gives

$$I = -\frac{B}{3}\left(h_p + h_p^2\right)\ .$$

Rearranging (2.37), we obtain

$$h_{\zeta\zeta\zeta} = \frac{B}{C}\left(-1 + \frac{1 + h_p + h_p^2}{h^2} - \frac{h_p + h_p^2}{h^3}\right)\ , \tag{2.40}$$

which is the governing equation for the height of the moving front over a pre-wetted wall. When $h_p = 0$, this reduces to

$$h_{\zeta\zeta\zeta} = \frac{B}{C}\left(-1 + \frac{1}{h^2}\right)\ , \tag{2.41}$$

which describes draining on a dry wall [94].

Numerical solution

We start our numerics by first solving (2.41), as an initial value problem, to show the behavior of the solution and how the problem of the contact line manifests itself numerically. We will then go on to solve (2.40) to show how a more realistic model solution is obtained by including a precursor film. This is solved as a boundary value problem, using a MATLAB BVP solver.

The film height in the equilibrium region is perturbed to provide a starting point for the initial value algorithm:-

$$h = 1 + \varepsilon f(\zeta) \,, \tag{2.42}$$

where $\varepsilon \ll 1$. To simplify the problem, we scale out B/C [69, 70]. Equation (2.41) then reduces to

$$h''' = -1 + \frac{1}{h^2} \,. \tag{2.43}$$

Substituting (2.42) in the governing equation and linearizing leads to

$$f''' \approx -2f \,, \tag{2.44}$$

which is a linear ordinary differential equation, so that f takes the form $e^{m\zeta}$. There are 3 roots, $m_0 = -\omega$, $m_1 = \frac{\omega}{2} + i\frac{\omega\sqrt{3}}{2}$ and $m_2 = \frac{\omega}{2} - i\frac{\omega\sqrt{3}}{2}$, where $\omega = 2^{1/3}$. The general solution for the above ordinary differential equation (2.44) is therefore

$$f = a_0 e^{-\omega\zeta} + e^{\frac{\omega}{2}\zeta}\left(a_1 \cos\frac{\omega\sqrt{3}}{2}\zeta + a_2 \sin\frac{\omega\sqrt{3}}{2}\zeta\right) \,.$$

We are however, perturbing the equilibrium height which is uniform far behind the front, therefore a_0 must be equal to zero otherwise the root becomes unbounded as $\zeta \to -\infty$. The general solution is therefore given by

$$f = e^{\frac{\omega}{2}\zeta}\left(a_1 \cos\frac{\omega\sqrt{3}}{2}\zeta + a_2 \sin\frac{\omega\sqrt{3}}{2}\zeta\right) \,, \tag{2.45}$$

with a corresponding film height

$$h = 1 + \varepsilon e^{\frac{\omega}{2}\zeta}\left(a_1 \cos\frac{\omega\sqrt{3}}{2}\zeta + a_2 \sin\frac{\omega\sqrt{3}}{2}\zeta\right) \,, \tag{2.46}$$

which can also be written in the form

$$h = 1 + \varepsilon e^{a\zeta}\cos(b(\zeta - \theta)) \,, \tag{2.47}$$

where θ is a constant, a_1 is absorbed into ε, $a = 0.5\,(2^{1/3})$ and $b = 0.5\,(2^{1/3}\sqrt{3})$. Since the governing equation is autonomous, the choice of complex root is arbitrary and we can shift

the ζ-axis to superimpose the two roots, *i.e.* set $\theta = 0$. Equation (2.47) can therefore be written as

$$h = 1 + \varepsilon e^{a\zeta} \cos b\zeta \ , \tag{2.48}$$

where the choice of ε determines how close to zero the solution gets.

The initial height is given by (2.48) and we let $\zeta = 0$ be the starting point. Repeated differentiation of (2.48) gives the initial conditions

$$h(0) = 1 + \varepsilon \qquad h'(0) = a\varepsilon \qquad h''(0) = \varepsilon(a^2 - b^2) \tag{2.49}$$

that can be used in an initial value algorithm. The original equation can be written as an initial-value problem for a system of first-order differential equations

$$h' = v \ , \tag{2.50}$$

$$v' = u \ , \tag{2.51}$$

$$u' = -1 + 1/h^2 \ . \tag{2.52}$$

The system of differential equations is now solved numerically, the first two equations using Euler's method and the last equation using a fourth order forward marching Runge-Kutta method [73].

Figure 2.4 shows the results obtained using the method described above. Without loss of generality, we have shifted the starting point from $\zeta = 0$ to $\zeta = -8$ so as to match the solution on a pre-wetted wall that will follow (which is slightly more complicated). The solution is characterised by a capillary ridge (approximately around $\zeta = -1.5$) which results from the competition between gravity and surface tension.

The film heights are obtained using three values of ε, ($\varepsilon = 0.005$, 0.004 and 0.003) to illustrate the behavior at the moving front. The values of ε determine how close h can get to zero (though never reaching it) before h increases beyond realistic expectations. Changing ε changes the minimum value of h that can be attained but only within certain limits. The minimum film height values corresponding to $\varepsilon = 0.005$, 0.004 and 0.003 are $h = 0.1043$, 0.1570 and 0.2285, respectively. These minimum heights are attained approximately around $\zeta = 0.5$ in figure 2.4.

From figure 2.4, it can be observed that the lower the minimum value of h attained in a particular case of ε, the higher the capillary ridge. In the analysis of Tuck & Schwartz [94], they found that the solution beyond this minimum point oscillates, having an infinite number of maxima and minima, the minima taking positive values that become smaller and smaller

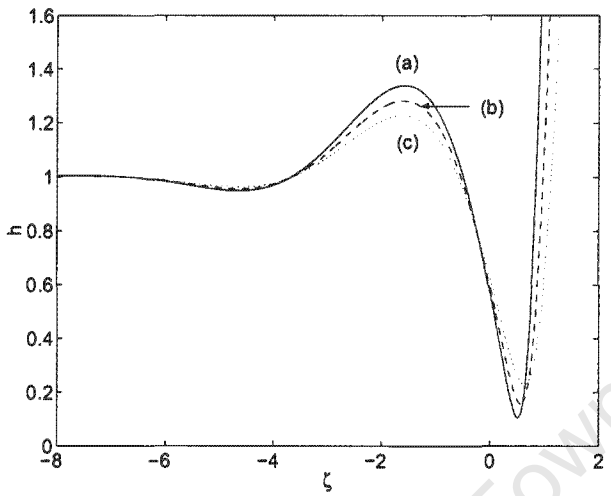

Figure 2.4: Film height for (a) $\varepsilon = 0.005$ (b) $\varepsilon = 0.004$ and (c) $\varepsilon = 0.003$

in magnitude as $\zeta \to +\infty$, while the maxima take values that become larger and larger as $\zeta \to +\infty$. These oscillations have been reported to be present even with the inclusion of second-order corrections *i.e.* terms of order ε^2, in equation (2.42). The observed oscillations in the numerical solution are evidently physically unrealistic and indicate the break down in the assumptions of the model. The reason for this being that as $h \to 0$, equation (2.43) is likely to encounter problems associated with the impossibility of moving a contact line on a dry wall, as discussed in Section 1.5. In fact, using initial condition (2.48) to solve equation (2.43), it is found that the film thickness can never be brought to zero, for any value of ε at a finite value of ζ [94]. Consequently, since the requirement that $h_p = 0$ can never be satisfied, we need to introduce a precursor layer, $h_p \neq 0$, to permit a solution consistent with the boundary conditions.

Given the impossibility of solving (2.41), which corresponds to draining with $h_p = 0$, we will now solve equation (2.40), which describes draining over a pre-wetted wall with a non-zero precursor layer, h_p. The method used on the previous case (dry wall draining) could still be used, solving equation (2.48) as an initial value problem, starting at one of the boundaries and shooting towards the other. However, the procedure now includes choosing ε by trial and error until boundary condition (2.36) is satisfied, which can take quite some time. For this reason, and also to demonstrate a different method we will now solve equation (2.40) as a boundary value problem subject to boundary conditions (2.35) and (2.36), using a MATLAB BVP solver.

For comparisons' sake, we will let h_p take on the minimum values that were obtained in the previous case *i.e* $h_p = 0.1043$, 0.1570 and 0.2285. These are the points at which the solution of the equation (for the three values of ε) that describes draining on a dry wall (2.41), became physically unrealistic and therefore seems to be the best point to impose boundary condition (2.36) for the solution to represent a more physically realistic model. The results are shown in figure 2.5.

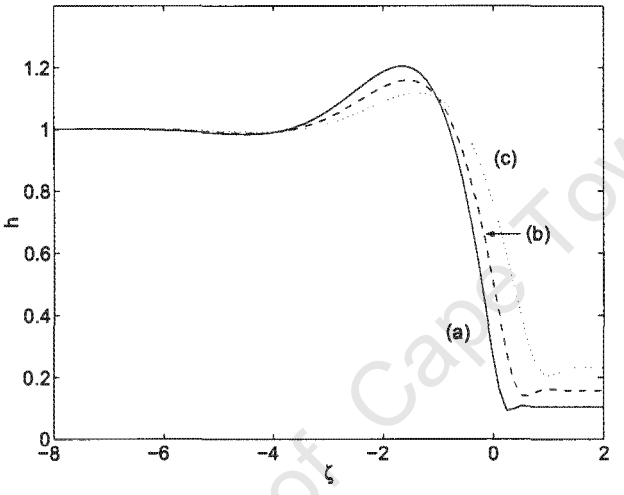

Figure 2.5: Film height for (a) $h_p = 0.2285$ (b) $h_p = 0.1570$ and (c) $h_p = 0.1043$

Comparing the two graphs, it is observed that in the second case, the curves do not shoot off to 'infinity', but attain some minimum height before taking on the specified precursor film height. The maximum heights (on the capillary ridge) in figure 2.5 are seen to be slightly lower than those obtained previously in figure 2.4. Presumably this occurs as a result of the slight difference in the two equations (namely the terms involving h_p). Similar results are found in [94].

From the derivation and numerical solution of the front flow model, we have shown how including a precursor film in the draining problem overcomes the difficulties arising at the contact line. We will use this information in subsequent chapters when modelling rotating thin films with a moving contact line.

2.7 Conclusion

In this chapter, we have laid the foundation for the mathematical modelling of thin films. We have demonstrated how the Navier-Stokes equations can be reduced to a simpler and more

manageable form using lubrication theory, and how the simplified form can be applied in many practical situations involving thin films, including driven films with a single free surface. This will be very useful in the following chapters where we consider thin centrifugally-driven films.

From the preceding results and discussion, it can be seen that modelling draining on a dry wall will encounter problems associated with the contact line singularity. One way to overcome this problem is to specify a precursor film ahead of the main flow. Therefore, a precursor film will be assumed in modelling films in subsequent chapters. While this may not be necessary for shear thinning fluids, as discussed in Section 1.5.2, we will nevertheless assume a precursor film when modelling non-Newtonian fluids for the sake of uniformity.

Chapter 3

Rotating Newtonian thin films

3.1 Introduction

The aim of this chapter is to introduce our first mathematical model of the spin coating process. Spin coating is a coating process that relies on centrifugal force for the spread of the coating fluid onto a rotating substrate. The fluid flows outward in the radial direction under the influence of centrifugal force. Spinning is continued until the required thickness is attained. Typical spinning speeds may vary in the range 1500 - 6000 rpm (3.98 - 15.92 rad/s) depending on the properties of the fluids and the type of substrate [9].

The fluids that are considered in this chapter are Newtonian fluids. Therefore, we will derive a model for axisymmetric flow of a thin viscous Newtonian fluid layer under the influence of centrifugal force, surface tension and gravity in Section 3.3. The Navier-Stokes equations, will be the starting point of our derivation. Lubrication theory will be used to reduce the Navier-Stokes equations as was carried out in Chapter 2.

Neglecting surface tension and gravity in this model results in the Emslie-Bonner-Peck model. The analytical results of this model are presented in Section 3.4. The stability of thin liquid films is important in the levelling of any unevenness that may arise in the film, therefore, a linear stability analysis of the derived governing equation for a rotating thin film is carried out in Section 3.5.

The non-linear evolution equation describing the shape of the film interface for axisymmetric flow of a thin Newtonian fluid layer under the influence of centrifugal force, surface tension and gravity is solved numerically in Section 3.6, using carefully constructed numer-

ical schemes and adequate treatment of the boundary conditions. The inclusion of surface tension in the model is the most demanding numerically but essentially we are interested in whether surface tension does make a difference to the final shape of the film.

Convergence, consistency and stability of the developed numerical scheme will be discussed in Section 3.6. In Section 3.7, we will compare the variation of film thickness along the radius for different values of surface tension and gravity effects that are calculated using some common Newtonian fluids.

3.2 Governing equations

We use cylindrical polar coordinates (r, θ, z) in a frame of reference rotating with the disk[1], where r is the radial distance from the centre of the disk, θ is the angle from some fixed radial line in the disk, we identify the z-axis with the axis of rotation and the plane $z = 0$, with the solid surface. The physical configuration is shown in figure 3.1. The equations of

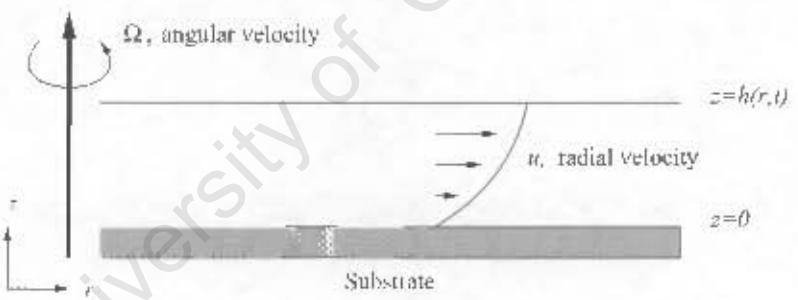

Figure 3.1: Side view of spinning disk.

motion for rotating incompressible fluids, including Coriolis and centrifugal forces are [77]:-

$$\rho\left(\frac{\partial \mathbf{u}}{\partial t} + (\mathbf{u}\cdot\nabla)\mathbf{u}\right) = -\nabla p - \mu\nabla^2\mathbf{u} + \rho[2\Omega\times\mathbf{u} + \Omega\times(\Omega\times\mathbf{r}) + \mathbf{g}] \quad (3.1)$$

$$\nabla\cdot\mathbf{u} = 0 \quad (3.2)$$

where p is the pressure, Ω the angular velocity, $\mathbf{g}$, gravity, $\mathbf{u}$ the velocity vector, μ the viscosity and ρ the fluid density. The first two terms in the square brackets of equation (3.1) represent the Coriolis and centrifugal forces, respectively.

[1] In applications with a rotating geometry, such as helicopter blades, turbo-machinery etc, it is preferable to use a rotating coordinate system [96], as opposed to a stationary coordinate system; a rotating one has the advantage of making it much simpler to visualize.

3.3 Derivation of the model

We now derive the governing equations for a thin film on a rotating substrate. We make the following assumptions:-

- the rotating plane is horizontal, smooth and infinite in extent, and rotates at a constant angular velocity,
- the liquid is Newtonian, axisymmetric and thin,
- gravitational and capillary forces are significant,
- air shear and evaporation are negligible.

The components of the Navier-Stokes equations for a rotating axisymmetric viscous thin film in the radial, azimuthal and z directions are: [10, 66] :-

$$\frac{\mathrm{d}u}{\mathrm{d}t} = -\frac{1}{\rho}\frac{\partial p}{\partial r} + \nu\left(\frac{\partial^2 u}{\partial r^2} + \frac{1}{r}\frac{\partial u}{\partial r} + \frac{\partial^2 u}{\partial z^2} - \frac{u}{r^2}\right) + 2\Omega v + \Omega^2 r \tag{3.3}$$

$$\frac{\mathrm{d}v}{\mathrm{d}t} = \nu\left(\frac{\partial^2 v}{\partial r^2} + \frac{1}{r}\frac{\partial v}{\partial r} + \frac{\partial^2 v}{\partial z^2} - \frac{v}{r^2}\right) - 2\Omega u \tag{3.4}$$

$$\frac{\mathrm{d}w}{\mathrm{d}t} = -\frac{1}{\rho}\frac{\partial p}{\partial z} + \nu\left(\frac{\partial^2 w}{\partial r^2} + \frac{\partial^2 w}{\partial z^2}\right) - g \tag{3.5}$$

where ν is the kinematic viscosity and (u, v, w) are the velocity components in the radial, azimuthal and z directions. The liquid-air interface is located at $z = h(r, t)$, where h is the film thickness. The continuity equation takes the form

$$\frac{1}{r}\frac{\partial}{\partial r}(ru) + \frac{\partial w}{\partial z} = 0 \; . \tag{3.6}$$

The boundary conditions to be applied for (3.3) - (3.6) are :- no-slip at the solid-liquid interface ($z = 0$),

$$u = v = w = 0 \; ; \tag{3.7}$$

at the free surface ($z = h$), the jump in normal stress is proportional to the curvature

$$p - p_a = -\sigma\kappa \tag{3.8}$$

where κ is the curvature[2], σ is the surface tension and p_a is the ambient pressure. The standard kinematic condition also holds:

$$w = \frac{\partial h}{\partial t} + u\frac{\partial h}{\partial r} \; . \tag{3.9}$$

[2] $\kappa \approx (1/r)(\partial/\partial r)[r(\partial h/\partial r)]$, using the level of accuracy of the lubrication approximation [16] .

The kinematic condition indicates that fluid particles at the free surface stay on the free surface, *i.e.* there is no evaporation or condensation, see [10] for example.

In addition, there is no shear (zero tangential stress) at the free surface:

$$u_z = v_z = 0 \,. \tag{3.10}$$

Non-dimensionalisation

We non-dimensionalise equations (3.3) - (3.6) using scales introduced in Section 2.3 and apply lubrication theory. The driving force in the radial direction is the centrifugal force. The characteristic radial velocity therefore, is obtained by balancing the centrifugal force with the dominant viscous forces, $U = \Omega^2 L H^2/\nu$ [66]. This scale was also implied in the analysis of Emslie *et al.* [25]. The influence of the Coriolis force on a rotating thin film is neglected. This is because the Coriolis term in the radial velocity equation can be shown to be negligible at leading order [66, 67]. This is systematically shown in Chapter 4.

The governing equations at leading order become

$$\frac{\partial^2 u}{\partial z^2} = \frac{\partial p}{\partial r} - r + \mathcal{O}(\delta^2) \tag{3.11}$$

$$\frac{\partial^2 v}{\partial z^2} = u + \mathcal{O}(\delta^2) \tag{3.12}$$

$$\frac{\partial p}{\partial z} = -B + \mathcal{O}(\delta^2)\,, \tag{3.13}$$

where $B = gH^3/\nu U L$, is the Bond number. Integrating (3.13) subject to boundary condition (3.8) leads to

$$p = p_a - B(z-h) - C\left(\frac{1}{r}\frac{\partial}{\partial r}\left(r\frac{\partial h}{\partial r}\right)\right)\,, \tag{3.14}$$

where $C = \sigma\delta^3/\mu U$ is the inverse capillary number. The radial velocity is obtained by integrating (3.11) subject to conditions (3.7) and (3.10):

$$u = \frac{1}{2}\left(\frac{\partial p}{\partial r} - r\right)(z^2 - 2zh)\,. \tag{3.15}$$

Differentiating (3.14) with respect to r, gives the expression for the pressure gradient

$$\frac{\partial p}{\partial r} = B\frac{\partial h}{\partial r} - C\frac{\partial}{\partial r}\left(\frac{1}{r}\frac{\partial}{\partial r}\left(r\frac{\partial h}{\partial r}\right)\right)\,. \tag{3.16}$$

The flux per unit length of circumference is then

$$Q = \int_0^h u\,\mathrm{dz} = -\frac{h^3}{3}\left(\frac{\partial p}{\partial r} - r\right)\,. \tag{3.17}$$

Integrating the continuity equation (3.6), and using Leibnitz's rule and the kinematic boundary condition (3.9) gives the thickness of the fluid film as

$$\frac{\partial h}{\partial t} + \frac{1}{r}\frac{\partial (rQ)}{\partial r} = 0 \,. \tag{3.18}$$

The governing equation for the flow of a thin film on a spinning disk with surface tension and gravity is therefore given by

$$\frac{\partial h}{\partial t} + \frac{1}{r}\frac{\partial}{\partial r}\left[\frac{rh^3}{3}\left(C\frac{\partial}{\partial r}\left(\frac{1}{r}\frac{\partial}{\partial r}\left(r\frac{\partial h}{\partial r}\right)\right) - B\frac{\partial h}{\partial r} + r\right)\right] = 0 \,. \tag{3.19}$$

Equation (3.19) is a fourth-order non-linear degenerate parabolic differential equation, typical of thin film flows with a free surface [64].

3.4 Emslie-Bonner-Peck model

Neglecting surface tension and gravity in equation (3.19) we obtain a simpler version of this equation, which is the Emslie-Bonner-Peck model. In this case, the governing equation reduces to

$$\frac{\partial h}{\partial t} + \frac{1}{r}\frac{\partial}{\partial r}\left(\frac{r^2h^3}{3}\right) = 0 \,. \tag{3.20}$$

Equation (3.20) describes the time evolution of the film thickness profile over the spinning disk. This equation is easily solved using the method of characteristics[3] as follows:- Let $r = r(t)$ and $h = h(r(t), t)$, describe the evolution of the surface contour with time. By the chain rule

$$\frac{dh}{dt}(r(t), t) = \frac{\partial h}{\partial t} + \frac{\partial h}{\partial r}\frac{dr}{dt} \,. \tag{3.21}$$

Equation (3.20) can be written as :-

$$-\frac{2h^3}{3} = \frac{\partial h}{\partial t} + rh^2\frac{\partial h}{\partial r} \,. \tag{3.22}$$

Comparing (3.21) and (3.22), it follows that

$$\frac{dh}{dt} = -\frac{2h^3}{3} \,, \qquad \frac{dr}{dt} = rh^2 \,. \tag{3.23}$$

[3]The aim of the method of characteristics is to change coordinates from say (r, t) to a new coordinate system in which a partial differential equation becomes an ordinary differential equation along certain curves in the r-t plane. Such curves, along which the solution of the PDE reduces to an ODE, are called characteristic curves [97]

Integrating (3.23a) yields

$$h(t) = \left(a + \frac{4}{3}t\right)^{-1/2} \tag{3.24}$$

for some constant a. If we consider a particle initially at (r_0, h_0), then $a = 1/h_0^2$ and

$$h(t) = h_0\left(1 + \frac{4}{3}h_0^2 t\right)^{-1/2} . \tag{3.25}$$

Substituting the expression (3.25) into (3.23b) we have

$$\frac{dr}{dt} = \frac{r h_0^2}{\left(1 + \frac{4}{3}h_0^2 t\right)} , \tag{3.26}$$

which upon integration yields

$$r(t) = c(3 + 4h_0^2 t)^{3/4} . \tag{3.27}$$

The initial condition implies that $c = r_0/3^{3/4}$. Therefore the radial motion of the particle is described by

$$r(t) = r_0\left(1 + \frac{4}{3}h_0^2 t\right)^{3/4} . \tag{3.28}$$

Equations (3.25) and (3.28) give the coordinates (r, h) after time t, of a particle initially at (r_0, h_0). Using contour surfaces for a number of initial distributions, Emslie *et al.* [25] showed that an initially uniform film remains uniform after spinning, and an initially irregular film as a rule becomes uniform upon spinning.

Suppose we have a film height that is constant (set $h = 1$) at $t = 0$, figure 3.2 shows how the film height varies with time. It can be seen that the liquid film thins out much more quickly when it is relatively thick than when thin. This means peaks will go down more quickly than pits, which explains why non-uniform layers become increasingly uniform with spinning. As spinning goes on, the film does continue to thin further, though ever more slowly. In fact, it is clear from (3.25) that $h \sim t^{-1/2}$. Viscous resistance to radial flow becomes very large for very thin films, with the result that thinning slows down remarkably as one attempts to produce extremely thin films [59].

Figure 3.3 shows the evolution of a film with the initial profile $h_0(r_0) = (1 + b\cos r_0)$, when $b = 0.05$. The figure clearly demonstrates the flattening effect produced by the flow with increasing t.

In certain cases however, rather than flattening, vertical wave fronts develop as shown in figure 3.4 when $t = 1$. This happens when $\partial h/\partial r \to \infty$. Given that

$$\frac{\partial h}{\partial r} = \frac{\partial h}{\partial r_0}\frac{\partial r_0}{\partial r} ,$$

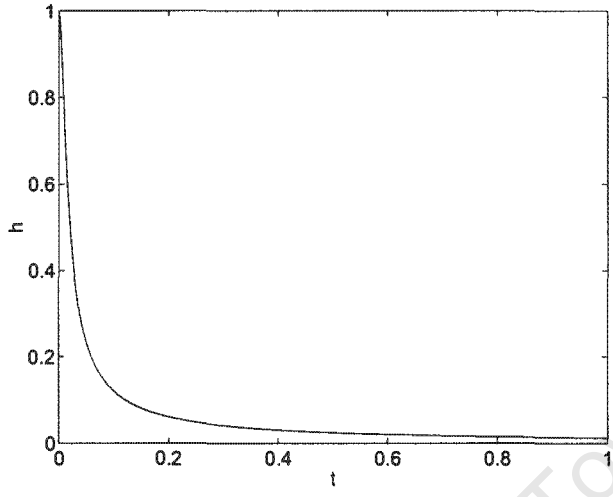

Figure 3.2: Variation of height with time for an initially constant film height.

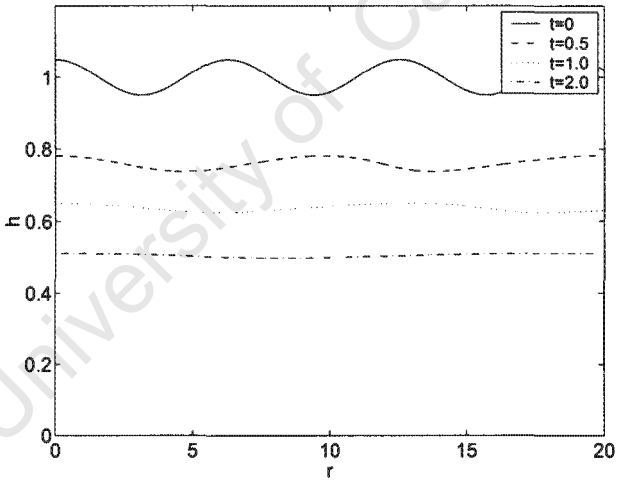

Figure 3.3: Successive surface contours for initial surface containing a ripple, with amplitude 0.05.

we will obtain an infinite gradient provided $\partial r/\partial r_0 = 0$, for some time t.

Differentiating (3.28) leads to

$$\frac{\partial r}{\partial r_0} = \left[1 + \frac{4}{3}h_0^2 t + 2r_0 h_0 t \frac{\partial h_0}{\partial r_0}\right] \Big/ \left(1 + \frac{4}{3}h_0^2 t\right)^{1/4}, \tag{3.29}$$

which may also be written as

$$\frac{\partial r}{\partial r_0} = \left[1 + \frac{2}{3}h_0 t\left(2h_0 + 3r_0\left(\frac{\partial h_0}{\partial r_0}\right)\right)\right] \Big/ \left(1 + \frac{4}{3}h_0^2 t\right)^{1/4}. \tag{3.30}$$

Equation (3.30) shows that for $\partial r/\partial r_0 = 0$ to occur, for some $t > 0$ requires

$$2h_0 + 3r_0\left(\frac{\partial h_0}{\partial r_0}\right) < 0 \qquad \Rightarrow \qquad \frac{\partial h_0}{\partial r_0} < -\frac{2h_0}{3r_0}. \tag{3.31}$$

When h_0 (> 0) is constant, condition (3.31b) is never satisfied and no vertical wave fronts are observed. For an initial contour $h_0(r_0) = (1 + b\cos\phi r_0)$, condition (3.31$b$) will be satisfied for

$$\phi r_0 > \frac{2}{3}\left(\frac{1 + b\cos\phi r_0}{b\sin\phi r_0}\right). \tag{3.32}$$

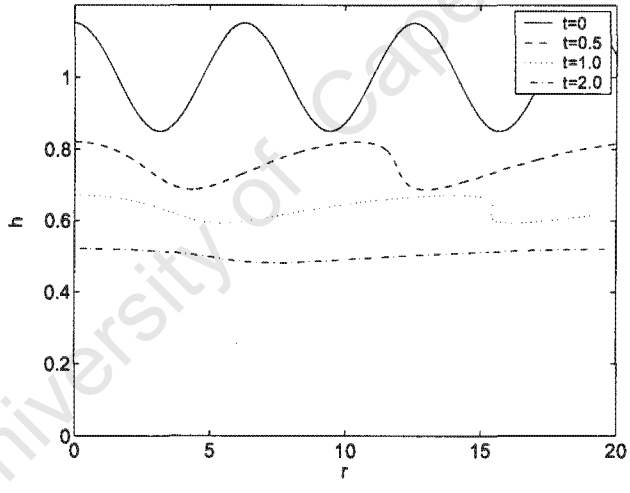

Figure 3.4: Successive surface contours for initial surface containing a ripple, with amplitude $b = 0.15$.

Figure 3.4 gives the evolution of a film with initial profile $h_0(r_0) = (1 + b\cos r_0)$ with $b = 0.15$ and $\phi = 1$. In this case condition (3.32) is satisfied when $r_0 > 9.8$ (radians). Figure 3.4 shows formation of a vertical front around $r = 15$. However, when $b = 0.05$ condition (3.32) is not satisfied in the interval $[0, 20]$ and no vertical fronts are observed for this interval, as shown in figure 3.3.

Vertical fronts are also referred to as shocks and are formed when two characteristics curves (see footnote 3) intersect, at which point the solution becomes multi-valued [68, 89]. For

times greater than the time of intersection, $\partial h/\partial r$ becomes infinite after which h folds over and looks like a breaking wave [60]. The time at which the characteristics first intersect is referred to as the breaking point.

One way to overcome vertical wave fronts is the addition of diffusion terms into the equation, which would in effect smooth out the surface, eliminating infinite gradients. Addition of surface tension and gravity, which has such a smoothing effect would partially remove this problem [66, 69]. To demonstrate this, we will now carry out a linear stability analysis for a rotating thin film to show how surface tension and gravity effects influence wave evolution on a rotating thin film.

3.5 Linear stability analysis

In this section, we look at the evolution of waves when surface tension and gravity are included, and how these affect the stability of a film on a rotating substrate.

Suppose the radial flow of a liquid is subjected to small amplitude disturbances. Consider a disturbance such that the interface $h(r,t)$ of the film has the form

$$h = h_0 + \varepsilon e^{i\alpha r - st}\,, \tag{3.33}$$

where ε is a small positive number *i.e.* we introduce a wave on the free surface of the film which is periodic in r. We want to find s, the growth rate of the linear disturbance. The disturbance will obviously decay in time if s is positive and grow if s is negative.

Let the governing equation of the flow be the one derived in Section 3.3:

$$\frac{\partial h}{\partial t} + \frac{1}{r}\frac{\partial}{\partial r}\left[\frac{rh^3}{3}\left(C\frac{\partial}{\partial r}\left(\frac{1}{r}\frac{\partial}{\partial r}\left(r\frac{\partial h}{\partial r}\right)\right) - B\frac{\partial h}{\partial r} + r\right)\right] = 0\,. \tag{3.34}$$

Substituting (3.33) into equation (3.34), at leading order (ε^0) we obtain

$$\begin{aligned} 0 = \frac{1}{3r^3}\Bigg[&2h_0^3r^3 + 3h_0^2r^4\frac{\partial h_0}{\partial r} - B\left(h_0^3r^2\frac{\partial h_0}{\partial r} + 3h_0^2r^3\left(\frac{\partial h_0}{\partial r}\right)^2 + h_0^3r^3\frac{\partial^2 h_0}{\partial r^2}\right) \\ &+ C\left(h_0^3\frac{\partial h_0}{\partial r} - h_0^3r\frac{\partial^2 h_0}{\partial r^2} + 2h_0^3r^2\frac{\partial^3 h_0}{\partial r^3} - 3h_0^2r\left(\frac{\partial h_0}{\partial r}\right)^2 + 3h_0^2r^2\left(\frac{\partial^2 h_0}{\partial r^2}\right)\left(\frac{\partial h_0}{\partial r}\right)\right. \\ &\left. + 3h_0^2r^3\left(\frac{\partial^3 h_0}{\partial r^3}\right)\left(\frac{\partial h_0}{\partial r}\right) + h_0^3r^3\frac{\partial^4 h_0}{\partial r^4}\right)\Bigg]\,. \end{aligned} \tag{3.35}$$

The first order equation (ε^1) implies that

$$s = \frac{1}{3r^3}\Bigg[\left(6h_0^2r^3 + 6h_0r^4\frac{\partial h_0}{\partial r} + i3h_0^2r^4\alpha\right) + B\Bigg(h_0^3r^3\alpha^2 - 3h_0^2r^2\frac{\partial h_0}{\partial r} - 6h_0r^3\left(\frac{\partial h_0}{\partial r}\right)^2 - 3h_0^2r^3\frac{\partial^2 h_0}{\partial r^2} + i\left(-h_0^3r^2\alpha - 6h_0^2r^3\alpha\frac{\partial h_0}{\partial r}\right)\Bigg) + C\Bigg(3h_0^2\frac{\partial h_0}{\partial r} + h_0^3r\alpha^2 - 3h_0^2r^2\alpha^2\frac{\partial h_0}{\partial r} + h_0^3r^3\alpha^4 - 6h_0r\left(\frac{\partial h_0}{\partial r}\right)^2 - 3h_0^2r\frac{\partial^2 h_0}{\partial r^2} + 6h_0^2r^2\frac{\partial^3 h_0}{\partial r^3} + 3h_0^2r^3\frac{\partial^4 h_0}{\partial r^4} + 6h_0r^2\frac{\partial^2 h_0}{\partial r^2}\cdot\frac{\partial h_0}{\partial r} + 6h_0r^3\frac{\partial^3 h_0}{\partial r^3}\cdot\frac{\partial h_0}{\partial r} + i\Bigg(-2h_0^3r^2\alpha^3 + h_0^3\alpha - 3h_0^2r^3\alpha^3\frac{\partial h_0}{\partial r} - 6h_0^2r\alpha\frac{\partial h_0}{\partial r} + 3h_0^2r^2\alpha\frac{\partial^2 h_0}{\partial r^2} + 3h_0^2r^3\alpha\frac{\partial^3 h_0}{\partial r^3}\Bigg)\Bigg)\Bigg]. \tag{3.36}$$

Our interest is to evaluate the behaviour of the real part of the exponent s, the growth rate of the perturbation,

$$\mathbb{R}(s) = \frac{1}{3r^3}\Bigg[\left(6h_0^2r^3 + 6h_0r^4\frac{\partial h_0}{\partial r}\right) + B\left(h_0^3r^3\alpha^2 - 3h_0^2r^2\frac{\partial h_0}{\partial r} - 6h_0r^3\left(\frac{\partial h_0}{\partial r}\right)^2 - 3h_0^2r^3\frac{\partial^2 h_0}{\partial r^2}\right) + C\Bigg(3h_0^2\frac{\partial h_0}{\partial r} + h_0^3r\alpha^2 - 3h_0^2r^2\alpha^2\frac{\partial h_0}{\partial r} + h_0^3r^3\alpha^4 - 6h_0r\left(\frac{\partial h_0}{\partial r}\right)^2 - 3h_0^2r\frac{\partial^2 h_0}{\partial r^2} + 6h_0^2r^2\frac{\partial^3 h_0}{\partial r^3} + 3h_0^2r^3\frac{\partial^4 h_0}{\partial r^4} + 6h_0r^2\frac{\partial^2 h_0}{\partial r^2}\cdot\frac{\partial h_0}{\partial r} + 6h_0r^3\frac{\partial^3 h_0}{\partial r^3}\cdot\frac{\partial h_0}{\partial r}\Bigg)\Bigg]. \tag{3.37}$$

Equation (3.37) determines the conditions under which a disturbance will grow or decay. In general, it is difficult to interpret, however in the case of an initially flat film, *i.e.* h_0 constant, we find

$$\mathbb{R}(s) = \frac{1}{3r^3}\left(6h_0^2r^3 + Bh_0^3r^3\alpha^2 + C\left(h_0^3r\alpha^2 + h_0^3r^3\alpha^4\right)\right). \tag{3.38}$$

The terms involving surface tension, gravity and centrifugal force in (3.38) are all positive, so that the linear disturbance in (3.33) decays as $t \to \infty$, indicating that spin coating is a stable method with regard to linear disturbances, for an initially constant film. This is consistent with earlier findings. Note that for spin coating where the film is underneath the plate ($B < 0$), a disturbance can grow and destabilise the film.

The Emslie-Bonner-Peck analysis in the previous section showed that when $B = C = 0$, waves may evolve to produce vertical wave fronts. Setting $B = C = 0$ in equation (3.36), we have

$$\mathbb{R}(s) = 2h_0^2 + 2rh_0\frac{\partial h_0}{\partial r}. \tag{3.39}$$

From equation (3.39), we can see that a disturbance will decay if

$$\frac{\partial h_0}{\partial r} > -\frac{h_0}{r}, \tag{3.40}$$

otherwise it is unstable to linear disturbances. This result is similar to that of (3.31*b*). In that case, the result indicates when a wave evolves to a vertical wave front. Now we see that if the gradient is slightly larger, then the waves will also grow in time.

3.6 Numerical scheme

In Section 3.3, we derived the governing equation for a rotating thin Newtonian film under the influence of surface tension and gravity. The aim of this section is to develop a numerical method to solve equation (3.19). This equation is non-linear and the fourth-order surface tension term is numerically demanding, especially since we are dealing with polar coordinates. But before we set out to develop the numerical scheme, we wish to highlight some of the features which will make a suitable numerical scheme for the equation at hand.

Convergence, consistency and stability of the numerical scheme

The traditional convergence that is required of any numerical scheme is not easy to discuss in this case since the equation at hand is highly non-linear. However, we want the difference equation solution to converge to the 'correct' solution as $\Delta r \to 0$. A good numerical scheme must be consistent and accurately discretise the equation [88]. It must also be stable and not exhibit oscillations [12]. In a progressive scheme, where each new set of calculated values depends on previously calculated sets of values, there is a possibility that a small numerical error can be magnified by repeated calculation [97]. A build up of error is therefore undesirable and may lead to numerical instability. The developed scheme must, therefore, be able to suppress error growth with increasing number of time steps. If the numerical scheme is stable, the build up of errors will in some sense remain bounded.

Our objective in this section is therefore to develop a numerical scheme that reasonably meets the above criteria *i.e* the predicted film heights should 'converge' as $\Delta r \to 0$ and $\Delta t \to 0$ and there must be no oscillations. We also need to be certain that there is mass conservation of the fluid. To do this we will incorporate a procedure in the code to make sure mass is conserved. The Emslie-Bonner-Peck analysis showed that shocks are likely to develop at the moving front if $C = 0$. Therefore, to avoid this problem when $C \ll 1$, a simple upwind method (shock capturing scheme) will be employed in our numerical scheme.

A precursor film is assumed ahead of the flow, to prevent the stress singularity at the

contact line and ensure convergence under spatial refinement, as discussed in Section 1.5.1. In addition, since we are dealing with a finite film, the earlier assumption of an infinite disk simply means edge effects can be neglected [93].

Discretisation of the equation

The numerical scheme developed in this section solves equation (3.19) on a regular polar coordinate grid (in the radial direction), since we are dealing with 2D axisymmetric flow. The numerical domain considered is divided into cells of size Δr in the interior and two cells of size $\Delta r/2$, one at each boundary (see figure 3.5). Each cell is assigned a reference point called a nodal point or simply a node. The film height at the centre of the i^{th} cell (node) of the grid at time $t = k\Delta t$ is denoted h_i^k. A constant time step Δt is used.

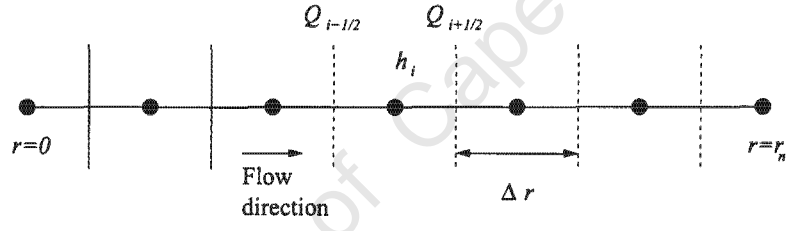

Figure 3.5: Cell centred grid on interval $[0\,, r_n]$.

The numerical scheme may be obtained by integrating equation (3.19) over a cell, between $r = r_{i-1/2}$ and $r = r_{i+1/2}$ in general, and between $r = 0$ and $r = r_{1/2}$ at the centre of the circle. This leads to:

$$\frac{r_{i+1/2}^2 - r_{i-1/2}^2}{2}\left(h_i^{k+1} - h_i^k\right) + \Delta t\left(r_{i+1/2}Q_{i+1/2} - r_{i-1/2}Q_{i-1/2}\right) = 0\,, \tag{3.41}$$

$$\frac{r_{1/2}^2}{2}\left(h_0^{k+1} - h_0^k\right) + \Delta t\left(r_{1/2}Q_{1/2}\right) = 0\,, \tag{3.42}$$

where $Q_{i+1/2}$ is the flux midway between the i^{th} and the $(i+1)^{th}$ points. The basic numerical scheme may be written as:

$$h_i^{k+1} = h_i^k - \frac{2\Delta t}{r_{i+1/2}^2 - r_{i-1/2}^2}\left(r_{i+1/2}Q_{i+1/2} - r_{i-1/2}Q_{i-1/2}\right)\,, \tag{3.43}$$

$$h_0^{k+1} = h_0^k - \frac{2\Delta t}{r_{1/2}^2}\left(r_{1/2}Q_{1/2}\right) = h_0^k - \frac{4\Delta t}{\Delta r}Q_{1/2}\,. \tag{3.44}$$

The outer boundary, between $r = r_{n-1/2}$ and $r = r_n$, is not crucial as we can take points far ahead of the main flow, assuming a precursor layer h_p, as will be later explained.

If the expressions of the fluxes only depend on values calculated at $k\Delta t$, the scheme is explicit. It is said to be implicit or semi-implicit otherwise. Equation (3.19) will be solved using a semi-implicit numerical scheme. The reason for this is that while explicit methods are much easier to implement and are conditionally stable, they are highly demanding in terms of step-size. If we choose Δt (or $\Delta t/\Delta r$) too large, the scheme becomes unstable and requires very small step-sizes [28]. The restriction placed on the time step for explicit schemes necessary to obtain stability for a given space step can sometimes be unrealistic, as the computations can take too long to be completed. With implicit methods, Δt can be large (therefore allowing faster computational times) and the scheme still remains stable. However, caution needs to be taken as you lose accuracy with increasing time step [89]. Therefore, there is need for a balance between acceptable error and speed of computation.

A fully implicit scheme would lead to a system of $n+1$ equations in $n+1$ unknowns. The solution to the fully implicit system of equations is very difficult to compute as our equation is highly non-linear. Therefore, an alternative semi-implicit scheme suggested by [63] will be implemented. This scheme involves calculating the derivatives of h at time $(k+1)\Delta t$ and the rest of the terms involving h at time $k\Delta t$, when calculating the fluxes. The flux will be discretised component by component. Using a 'test' upwind scheme, the flux may be written as:

$$Q_{i+1/2}^{k+1} = \frac{(h^k)^3}{3}\bigg|_{i+1/2}\left(C\frac{\partial}{\partial r}\left(\frac{1}{r}\frac{\partial}{\partial r}\left(r\frac{\partial h}{\partial r}\right)\right)_{i+1/2}^{k+1} - B\left(\frac{\partial h}{\partial r}\right)_{i+1/2}^{k+1} + r_{i+1/2}\right). \tag{3.45}$$

The term $h_{i+1/2}^k$ in the flux is taken to be $h_{i+1/2}^k = (h_i^k + h_{i+1}^k)/2$, but to capture the shock, the upwind scheme dictates that the leading term (centrifugal part) be taken as

$$r_{i+1/2}\frac{(h^k)^3}{3}\bigg|_{i+1/2} = \frac{r_{i+1/2}(h_i^k)^3}{3}.$$

The gravity and surface tension terms are discretised using a mixed explicit/implicit scheme. The gravity term is quite straightforward:

$$-B\frac{h^3}{3}\frac{\partial h}{\partial r}\bigg|_{i+1/2} = -\frac{B}{3}\left(\frac{h_i^k + h_{i+1}^k}{2}\right)^3\frac{h_{i+1}^{k+1} - h_i^{k+1}}{\Delta r}. \tag{3.46}$$

The surface tension term is more difficult to evaluate. Using second order approximations for the derivatives inside the domain, the term may be written as:

$$\begin{aligned}\Gamma_{i+1/2} &= C\frac{h^3}{3}\frac{\partial}{\partial r}\left(\frac{1}{r}\frac{\partial}{\partial r}\left(r\frac{\partial h}{\partial r}\right)\right)\bigg|_{i+1/2} \\ &= \frac{C}{3\Delta r^3}\left(\frac{h_i^k + h_{i+1}^k}{2}\right)^3\left(\frac{i+3/2}{i+1}h_{i+2}^{k+1} - \frac{3i+1/2}{i}h_{i+1}^{k+1} + \frac{3i+5/2}{i+1}h_i^{k+1} - \frac{i-1/2}{i}h_{i-1}^{k+1}\right).\end{aligned}$$

This approximation is valid for all interior points but not at the boundaries of the domain. Four boundary conditions are required to solve equation (3.19). Assuming the flow to be axisymmetric and a precursor layer, h_p, ahead of the main flow, we use the following boundary conditions:

$$Q(0) = 0\,, \qquad \left.\frac{\partial h}{\partial r}\right|_{r=0} = 0\,, \qquad h_\infty = h_p\,, \qquad \left.\frac{\partial h}{\partial r}\right|_{r=\infty} = 0\,, \tag{3.47}$$

where h_∞ is the film height far ahead of the moving front.

Near the centre at $r = \frac{1}{2}$, the flux must be calculated carefully using the points $\frac{3}{4}\Delta r$ and $\frac{1}{4}\Delta r$ to avoid division by zero. A second order approximation is given by:

$$\begin{aligned}\Gamma_{1/2} &= C\frac{h^3}{3}\frac{\partial}{\partial r}\left(\frac{1}{r}\frac{\partial}{\partial r}\left(r\frac{\partial h}{\partial r}\right)\right)\Bigg|_{1/2} \\ &= \frac{4C}{3\Delta r^3}\left(\frac{h_0^k + h_1^k}{2}\right)^3\left(\frac{2}{3}h_2^{k+1} - \frac{8}{3}h_1^{k+1} + 2h_0^{k+1}\right).\end{aligned}$$

At the other boundary, including a precursor film means if we take a point far ahead of the flow, the fluid height is constant over a small distance and the flux and its derivatives will all be equal zero.

Note that simply replacing the derivatives in equation (3.19) by equivalent finite difference expressions could lead to division by zero which is undesirable. Integrating over a cell as we have done, leads to the same result and we are able to apply boundary condition (3.47*b*) at the centre without dividing by zero.

Evaluating equations (3.43) and (3.44) at all the points of the domain gives a penta-diagonal matrix of coefficients. The system of equations can be expressed as a set of $n+1$ linear equations written as:-

$$\begin{pmatrix} a_{01} & a_{02} & a_{03} & 0 & \dots & \dots & 0 \\ a_{11} & \ddots & \ddots & \ddots & \ddots & \ddots & \vdots \\ a_{21} & \ddots & \ddots & \ddots & \ddots & \ddots & \vdots \\ 0 & \ddots & \ddots & \ddots & \ddots & \ddots & 0 \\ \vdots & \ddots & \ddots & \ddots & \ddots & \ddots & a_{n-2,n} \\ \vdots & \ddots & \ddots & \ddots & \ddots & \ddots & a_{n-1,n} \\ 0 & \dots & \dots & 0 & a_{n,n-2} & a_{n,n-1} & a_{n,n} \end{pmatrix} \begin{pmatrix} h_0^{k+1} \\ h_1^{k+1} \\ h_2^{k+1} \\ \vdots \\ \vdots \\ h_{n-1}^{k+1} \\ h_n^{k+1} \end{pmatrix} = \begin{pmatrix} h_0^k \\ h_1^k \\ h_2^k \\ \vdots \\ \vdots \\ h_{n-1}^k \\ h_n^k \end{pmatrix} - \Upsilon\,, \tag{3.48}$$

where the coefficients are calculated as follows:-

$$\begin{aligned}
a_{i,i-2} &= b_1 \frac{i-\frac{3}{2}}{i-1}\,, \\
a_{i,i-1} &= s_1 - b_2 \frac{i-\frac{1}{2}}{i} - b_1 \frac{3i-\frac{1}{2}}{i}\,, \\
a_{i,i} &= 1-(s_2+s_1) + b_2 \frac{3i+\frac{5}{2}}{i+1} + b_1 \frac{3i-\frac{5}{2}}{i-1}\,, \\
a_{i,i+1} &= s_2 - b_2 \frac{3i+\frac{1}{2}}{i} - b_1 \frac{i+\frac{1}{2}}{i}\,, \\
a_{i,i+2} &= b_2 \frac{i+\frac{3}{2}}{i+1}\,,
\end{aligned}$$

and

$$\begin{aligned}
b_1 &= \epsilon\left(i-\frac{1}{2}\right)\left(\frac{h_i^k+h_{i-1}^k}{2}\right)^3 \frac{C}{3\Delta r^3}\,, \\
b_2 &= \epsilon\left(i+\frac{1}{2}\right)\left(\frac{h_i^k+h_{i+1}^k}{2}\right)^3 \frac{C}{3\Delta r^3}\,, \\
s_1 &= -\epsilon\left(i-\frac{1}{2}\right)\left(\frac{h_i^k+h_{i-1}^k}{2}\right)^3 \frac{B}{3\Delta r}\,, \\
s_2 &= -\epsilon\left(i+\frac{1}{2}\right)\left(\frac{h_i^k+h_{i+1}^k}{2}\right)^3 \frac{B}{3\Delta r}\,,
\end{aligned}$$

where

$$\epsilon = \frac{2\Delta t}{\Delta r\left(\left(i+\frac{1}{2}\right)^2-\left(i-\frac{1}{2}\right)^2\right)}\,,$$

$$\Upsilon = \epsilon\frac{\Delta r}{3}\left[\left(i+\frac{1}{2}\right)^2\left(\frac{h_i^k+h_{i+1}^k}{2}\right)^3 - \left(i-\frac{1}{2}\right)^2\left(\frac{h_i^k+h_{i-1}^k}{2}\right)^3\right].$$

The film height h^{k+1} is then obtained from equation (3.48) using an LU factorisation of the form:-

$$A = \begin{pmatrix}
1 & 0 & \dots & \dots & \dots & \dots & 0 \\
\beta_1 & \ddots & \ddots & \ddots & \ddots & \ddots & \vdots \\
\alpha_1 & \ddots & \ddots & \ddots & \ddots & \ddots & \vdots \\
0 & \ddots & \ddots & \ddots & \ddots & \ddots & \vdots \\
\vdots & \ddots & \ddots & \ddots & \ddots & \ddots & \vdots \\
\vdots & \ddots & \ddots & \ddots & \ddots & \ddots & 0 \\
0 & \dots & \dots & 0 & \alpha_{n-2} & \beta_{n-1} & 1
\end{pmatrix}
\begin{pmatrix}
\gamma_1 & \zeta_1 & \eta_1 & 0 & \dots & \dots & 0 \\
0 & \ddots & \ddots & \ddots & \ddots & \ddots & \vdots \\
\vdots & \ddots & \ddots & \ddots & \ddots & \ddots & \vdots \\
\vdots & \ddots & \ddots & \ddots & \ddots & \ddots & 0 \\
\vdots & \ddots & \ddots & \ddots & \ddots & \ddots & \eta_{n-2} \\
\vdots & \ddots & \ddots & \ddots & \ddots & \ddots & \zeta_{n-1} \\
0 & \dots & \dots & \dots & \dots & 0 & \gamma_n
\end{pmatrix}$$

from which we can easily get h^{k+1} using forward and backward substitutions.

3.7 Preliminary results

3.7.1 Numerical scheme validation

To ensure the accuracy of the numerical scheme and the actual computations, we carry out a number of tests. These include mass conservation, convergence of solutions, as well as comparison with the Emslie-Boner-Peck model. The figures in this section show how the free surface of an initial film, described by $h(r) = 1 - r^2$, evolves after a given time. A precursor film, $h_p = 10^{-3}$, is assumed in all the simulations for the model developed. All simulations in this section are carried out using $\Delta r = 8 \times 10^{-4}$ and $\Delta t = 10^{-3}$.

Mass Conservation

The volume of the liquid

$$V = \sum_{i=0}^{nr-1} \int_{r_i}^{r_{i+1}} hr \, \mathrm{d}r \, , \tag{3.49}$$

(where h is approximated using a linear expression between two points) is continuously monitored during the computations by means of a function incorporated into the code. The surface tension term, being a third order derivative in polar coordinates, is not easy to solve numerically. Nevertheless, the change in volume during the computations is nominal. For example, the change in volume is in the range $3.596 \times 10^{-5}\,\% - 5.125 \times 10^{-6}\,\%$ for values of C in the range $8.8451 \times 10^{-2} - 8.8451 \times 10^{-6}$, respectively (using $\Delta r = 8 \times 10^{-4}$ and $\Delta t = 10^{-3}$). Consequently, mass loss/gain due to computational error or otherwise is minimal and mass is conserved. Note that mass conservation may not look obvious at a glance of the figures that will follow in this section, but the false impression one gets is due to the fact that we are dealing with polar coordinates.

Convergence of solution

Convergence of the computed solutions is made evident by the fact that the solution becomes insensitive to further refinement of the grid. Varying space and time steps were used in the solution, with Δr in the range $2 \times 10^{-4} - 2 \times 10^{-2}$ and Δt in the range $5 \times 10^{-4} - 1 \times 10^{-2}$. As the space and time steps were decreased to $\Delta r \leq 2 \times 10^{-4}$ and $\Delta t \leq 1 \times 10^{-3}$, there was no significant change in the volume. For example, when $\Delta r = 2 \times 10^{-4}$ and $\Delta t = 5 \times 10^{-4}$, the change in volume is only $10^{-6}\%$. Therefore, we can conclude that the solution converges.

Results when $B = 0$ and $C = 0$

The results of the numerical scheme developed in Section 3.6, with the surface tension and gravity terms set to zero, are compared to the Emslie-Bonner-Peck model (equations (3.25) & (3.28)) for an initial film described by $h(r) = 1 - r^2$. Figure 3.6 shows the predicted film height using the models at $t = 0, 0.5, 1.5, 5$ and 10. The corresponding curves are labelled (a), (b), (c), (d) and (e), respectively. For each case $(a) - (e)$, there are two curves corresponding to the numerical and analytical results.

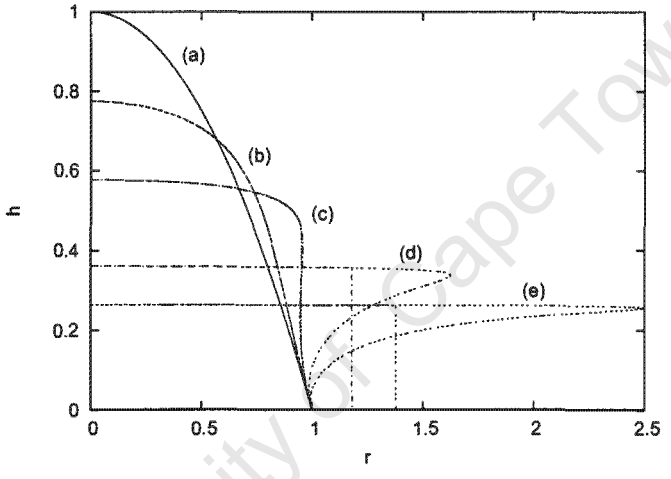

Figure 3.6: Comparisons of the Emslie-Bonner-Peck model and our model at various times.

Both models predict the same film height for most of the domain. In fact the two sets of curves (a) and (b) are virtually identical. The models are nearly the same for curves (c) but a slight difference is observed as the Emslie-Bonner-Peck model starts becoming multi-valued. For curves (d) and (e), the two models become very different at the front with the wave fully developed in the Emslie-Bonner-Peck model. The wave is obviously unphysical and violates the lubrication approximation ($h_r \ll 1$). The numerical scheme developed in Section 3.6 is able to avoid the development of this front wave due to the fact that an upwind scheme is employed.

The Emslie-Bonner-Peck model does not deal with contact line movement, but imposes a no-slip boundary condition on a dry substrate. This is evident in the non-movement of the front, which is clearly not realistic. The numerical scheme developed in this chapter, includes a precursor film ahead of the main flow. This allows movement of the front as figure 3.6 illustrates. Nevertheless, the film height predicted by the two models compares very well

over the central region, demonstrating that our numerical scheme agrees with the analytical solution of the Emslie-Bonner-Peck model for zero gravity and surface tension.

To set a basis for comparison with graphs in Sections 3.7.3 and 3.7.4, figure 3.7 shows the evolution of a rotating film due to centrifugal force alone, as predicted by our numerical scheme. Gravity and surface tension effects are again set to zero. Curves (a), (b), (c), (d) and (e) represent the profile at $t = 0, 0.5, 1.5, 5$ and 10. Unless otherwise indicated, this standard will be followed throughout the section.

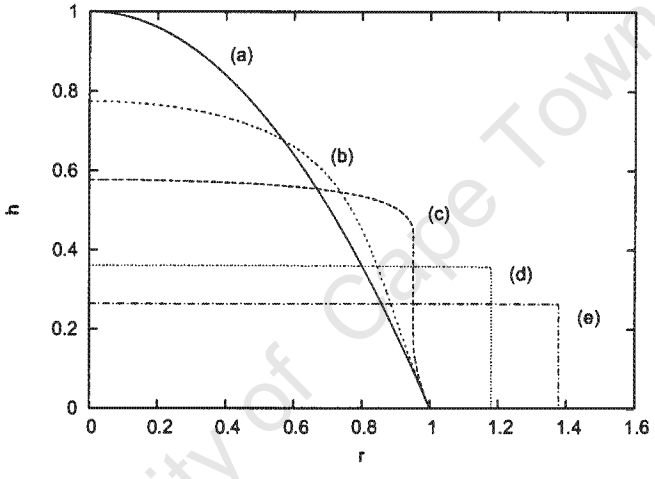

Figure 3.7: Evolution of Newtonian film with $B = 0$ and $C = 0$.

Figure 3.7 shows the evolution of the initial film into a uniform film profile, with $h \approx 0.264$ for all r at $t = 10$. Comparing how much thinning is achieved in intervals of 0.5, 1.5, 3.5 and 5 units of time, it is also obvious that the liquid film thins out much more quickly when it is relatively thick than when thin. Although the imposed film shape is not necessarily realistic (the initial fluid may be applied in a multitude of ways), it does show that uniform films can quickly be achieved when dealing with Newtonian spin coating.

3.7.2 Estimating parameters for the model

The height and length scales that are going to be used are of the order of magnitude common in spin coating applications such as CD manufacturing as well as experimental values taken from [9, 52]: $H = 1 \times 10^{-3}\,\mathrm{m}$, $L = 0.12\,\mathrm{m}$ and angular velocity is taken as $\Omega = 5.235\,\mathrm{rad/s}$ and $\Omega = 10.47\,\mathrm{rad/s}$. The values for the following Newtonian liquids (see table 3.1) are taken

from [53]. Water is included with the other Newtonian fluids for comparison reasons.

Liquid (20°C)	ν m^2/s	μ $N.s/m^2$	σ N/m
Water	1.00379×10^{-6}	1.002×10^{-3}	0.07275
Glycerin	1.1813×10^{-3}	1.49	0.0634
Mercury	1.145×10^{-4}	1.552	0.465

Table 3.1: Experimental values for viscosity and surface tension for three Newtonian fluids.

Using the values in table 3.1 we will now calculate the characteristic radial velocity, U, the Bond number, B, and the inverse capillary number, C, as specified in Section 3.3. The radial velocity is taken as $\Omega = 5.235\,\text{rad/s}$. These are presented in the following table (table 3.2).

	U	B	C
Water	3.2762	0.0248	1.2825×10^{-5}
Glycerin	0.0028	0.0248	8.8451×10^{-6}
Mercury	0.0287	0.0248	6.0368×10^{-6}

Table 3.2: Estimated values for U, B and C when $\Omega = 5.235\,\text{rad/s}$

Table 3.3 shows the values of U, B and C when the angular velocity, $\Omega = 10.47\,\text{rad/s}$. This table is presented to help us appreciate that these are not constant values and it also shows how quickly the different parameters can change when the angular velocity or some other aspect of the spinning process is changed. For example, when the angular velocity is doubled, the centrifugal force becomes more dominant and reduces surface tension and gravity effects to 25% of the original value. Note that as the dominant driving force, centrifugal force is scaled to 1.

	U	B	C
Water	13.105	0.0062	3.2062×10^{-6}
Glycerin	0.0111	0.0062	2.2113×10^{-6}
Mercury	0.1149	0.0062	1.5092×10^{-6}

Table 3.3: Estimated values for U, B and C when $\Omega = 10.47\,\text{rad/s}$

3.7.3 Results when $B \neq 0$ and $C = 0$

In this section, we try and establish the effect of adding gravity alone to the model. This will be carried out using two values of the Bond number, B.

Figure 3.8 shows results when $B = 0.0248$, corresponding to $\Omega = 5.235\,\text{rad/s}$ while figure 3.9 uses a slightly higher value ($B = 0.248$). This would be expected for example, when the film is thicker or rotational speed slower.

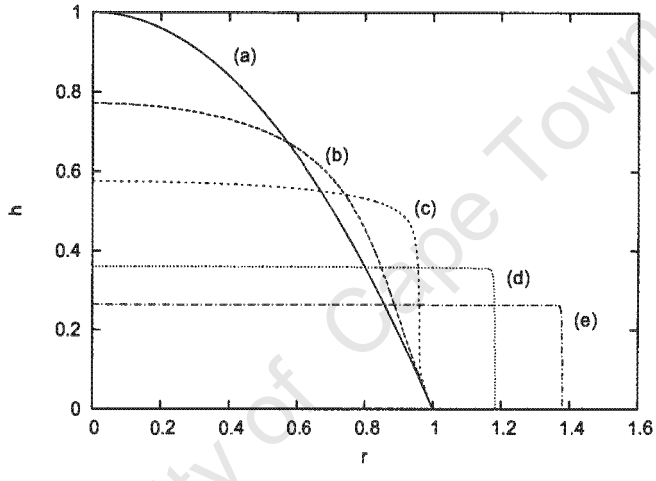

Figure 3.8: Evolution of Newtonian film with $B = 0.0248$ and $C = 0$.

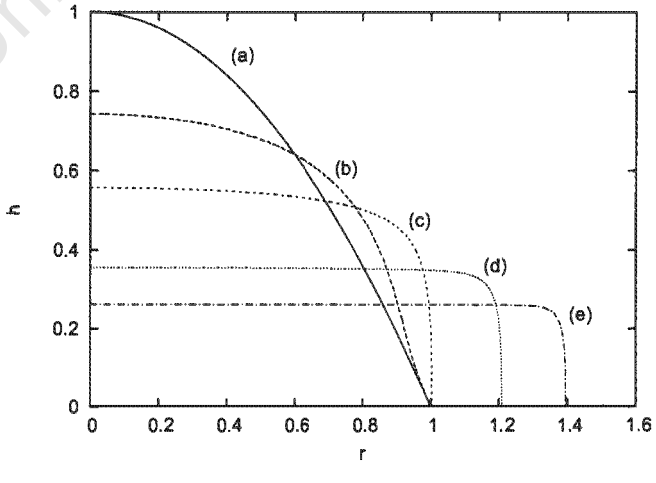

Figure 3.9: Evolution of Newtonian film with $B = 0.248$ and $C = 0$.

Comparing figures 3.8 and 3.9 to figure 3.7, the smoothing effect of gravity especially on the edges is evident in curves (c), (d) and (e). The film also spreads slightly further for a larger B. The two figures show that the reduction in the final film height is minimal with $h \approx 0.263$ and $h \approx 0.261$, respectively for all r at $t = 10$. However, for relatively thicker films (compare curves (b) and (c) in the two figures), gravity helps reduce the film heights. The smoothing effect observed is as a result of greater diffusion being added from the governing equation and also by the numerical scheme.

3.7.4 Results when $B \neq 0$ and $C \neq 0$

To demonstrate the effects of gravity and surface tension on the evolution of a rotating film, we will once again use parameters corresponding to $\Omega = 5.235\,\text{rad/s}$. Since the governing equation is non-dimensionalised, there is no need to try out the different parameters for all the fluids. Instead, we will make use of the values B and C for glycerin, then adjust these starting values to try and simulate the effects of gravity and surface tension on a rotating film. The results generated from the simulations for various values of B and C will now be presented to determine their influence on the resulting profiles.

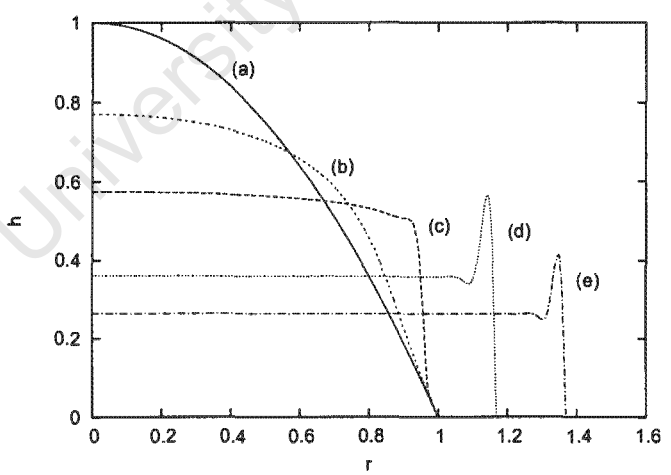

Figure 3.10: Evolution of Newtonian film at various times, with $B = 0.0248$ and $C = 8.8451 \times 10^{-6}$.

Figure 3.10 shows the predicted profiles at the various times during the process when $B = 0.0248$ and $C = 8.8451 \times 10^{-6}$. The results show a capillary ridge developing at about

$t = 1.5$, while the profiles for $t = 5$ onwards show a 'fully' developed capillary ridge. Away from the capillary ridge, the film quickly flattens as can be seen for $t \geq 5$ in figure 3.10.

The value of C that is used here is very small compared to that of B, which is also quite small in comparison to the centrifugal force which is of $\mathcal{O}(1)$. Therefore, we expect surface tension effects to be quite negligible in this flow so that the flattening process is achieved primarily by the centrifugal force. However, at the front the characteristic capillary ridge is evident, which results from the competition mainly between centrifugal and surface tension forces. This capillary ridge has been observed in many experimental studies, see [29, 57] for example.

Figures 3.11 and 3.12, show the evolution of the film when B is increased to 0.248 and then 1, respectively. We have left the value of C unchanged. Figure 3.11 shows a reduced capillary ridge as gravity effects are increased. When the value of B is increased to 1, the smoothing effects of gravity are even more evident at the front, see figure 3.12. The fluid also spreads further than was observed when B was smaller. This is to be expected as gravity acts to reduce the film and so helps the spreading.

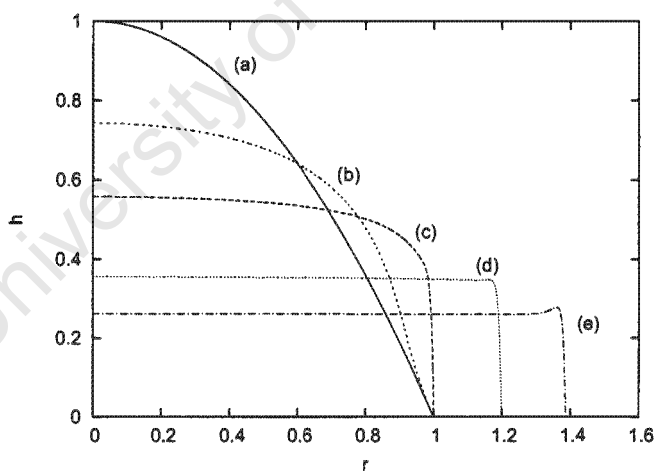

Figure 3.11: Evolution of Newtonian film with $B = 0.248$ and $C = 8.8451 \times 10^{-6}$.

Figures 3.13 and 3.14 show the effect of C being increased to 8.8451×10^{-5} and 8.8451×10^{-4} respectively, while keeping B at 0.0248. Comparing these two figures with figure 3.10, we note the obvious difference in the shape of the capillary ridge that forms at the front. The ridge gets thicker as surface tension effects are increased. Consequently, there is a reduction in the spread rate of the fluid. The rest of the film does not seem to be affected by this

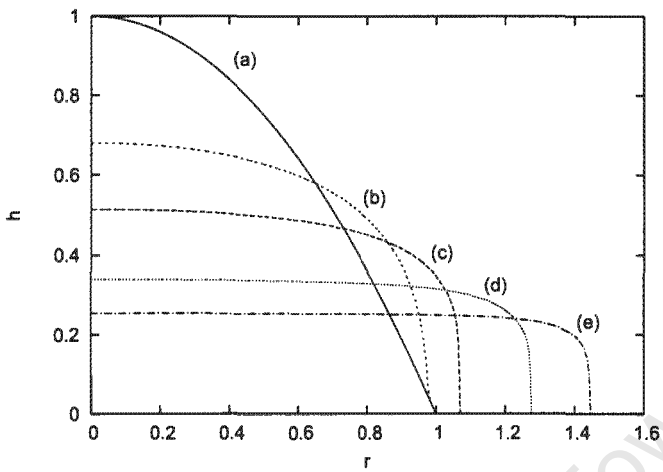

Figure 3.12: Evolution of Newtonian film with $B = 1$ and $C = 8.8451 \times 10^{-6}$.

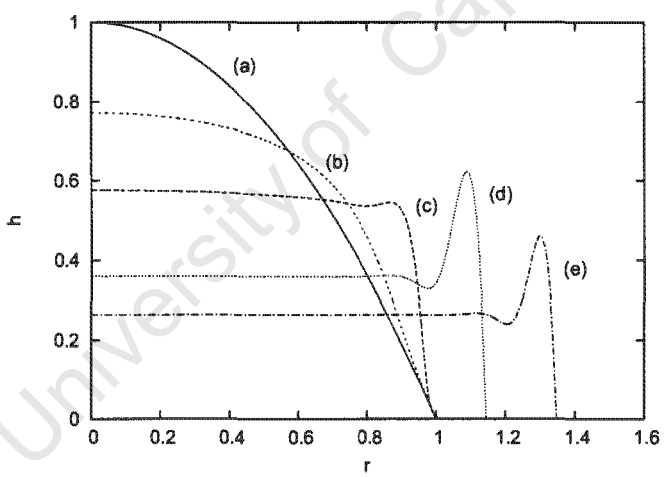

Figure 3.13: Evolution of Newtonian film with $B = 0.0248$ and $C = 8.8451 \times 10^{-5}$.

increase in surface tension effects, as can be seen from the predicted film height towards the central region.

Figures 3.15 and 3.16 show the predicted evolution when $C = 8.8451 \times 10^{-3}$ and $C = 8.8451 \times 10^{-2}$, respectively, and $B = 0.0248$. Both figures show a remarkable decrease in the spread of the fluid as the capillary ridge becomes even thicker. In the latter figure, the predicted film height at the centre is much higher than all the previous cases with smaller surface tension effects.

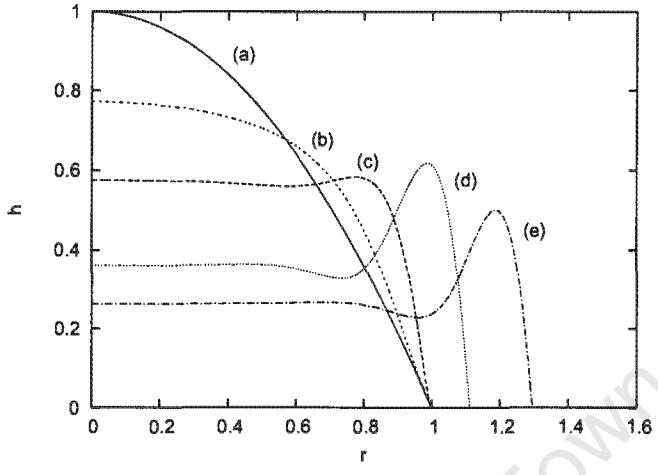

Figure 3.14: Evolution of Newtonian film with $B = 0.0248$ and $C = 8.8451 \times 10^{-4}$.

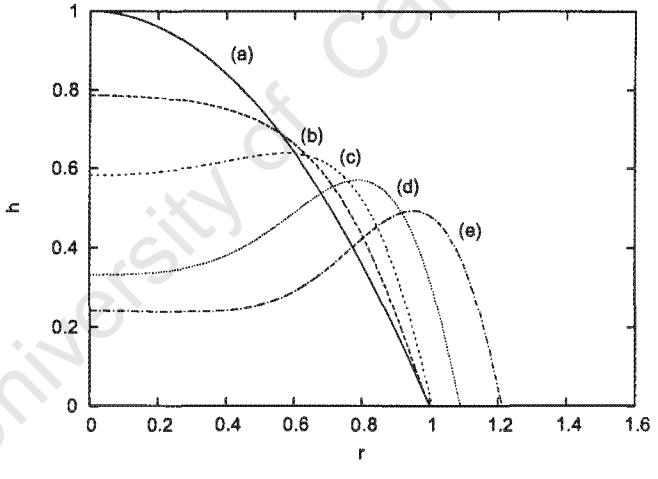

Figure 3.15: Evolution of Newtonian film with $B = 0.0248$ and $C = 8.8451 \times 10^{-3}$.

Figure 3.17 shows how increasing B to 1 at this point affects the film. This shows how gravity helps the film spread further and therefore thin quicker.

Figures 3.18 and 3.19 show different combinations of B and C. Taking gravity effects as significant ($B = 1$) and reducing surface tension effects shows the capillary ridge getting smaller and smaller. Therefore, the resulting shape of the capillary ridge clearly depends on the interaction between centrifugal force, surface tension and gravity.

From the figures, it is clear that increasing C shows a reduction in the spread rate of the fluid

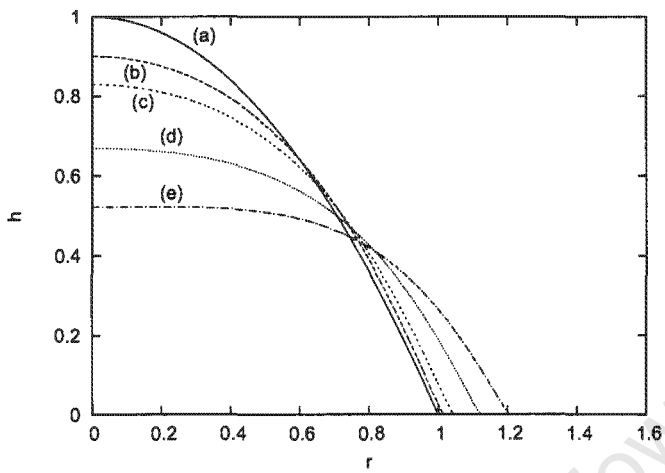

Figure 3.16: Evolution of Newtonian film with $B = 0.0248$ and $C = 8.8451 \times 10^{-2}$.

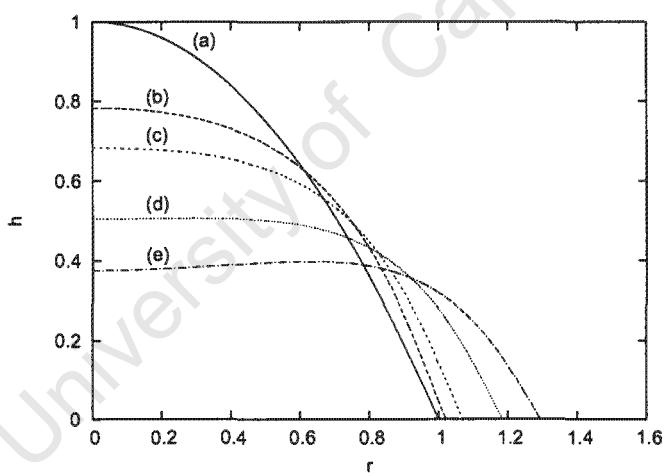

Figure 3.17: Evolution of Newtonian film with $B = 1$ and $C = 8.8451 \times 10^{-2}$.

which leads to much thicker films. This shows that an increase in surface tension does reduce the spread rate of the film as surface tension tends to hold the fluid together. On the other hand, gravity when significant helps the spread of the rotating film. The different shapes of the capillary ridge depicted in the various graphs also confirms how this is dependent on the interplay between centrifugal force, surface tension and gravity.

To study the effect of the precursor height on the resulting profiles, various precursor layer heights are tested in the scheme for various values of B and C. The results show that

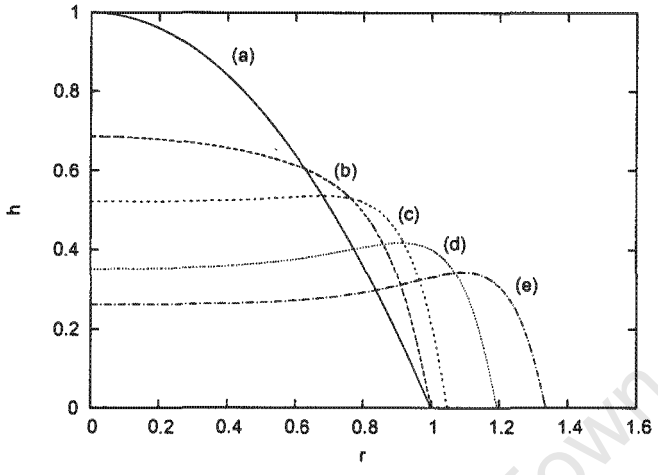

Figure 3.18: Evolution of Newtonian film with $B = 1$ and $C = 8.8451 \times 10^{-3}$.

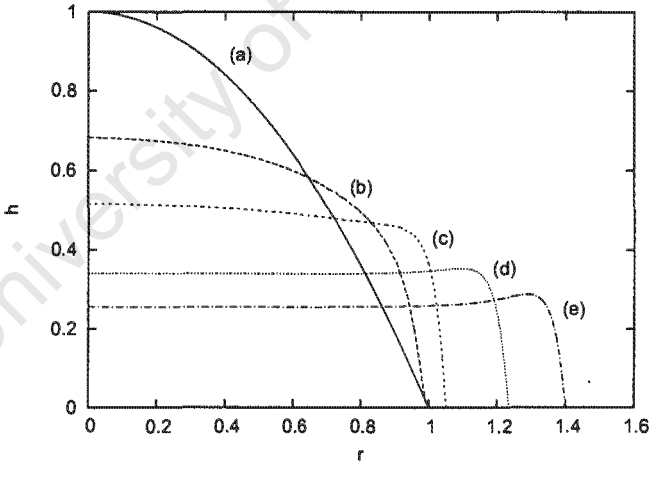

Figure 3.19: Evolution of Newtonian film with $B = 1$ and $C = 8.8451 \times 10^{-4}$.

changing the precursor height layer from $h_p = 10^{-2}$ through to $h_p = 10^{-7}$ does not produce any noticeable changes in the film height or the capillary ridge height. A precursor height of $h_p = 10^{-1}$ though gives impractical results, with negative heights on some portion of the domain.

Longer spinning times

Finally, to simulate spinning for longer times for Newtonian fluids, we take a final time of $t = 100$. The results are shown in figure 3.20. In this case, the curves (a), (b), (c), (d) and (e) represent predicted profiles at $t = 0, 25, 50, 75$ and 100, respectively.

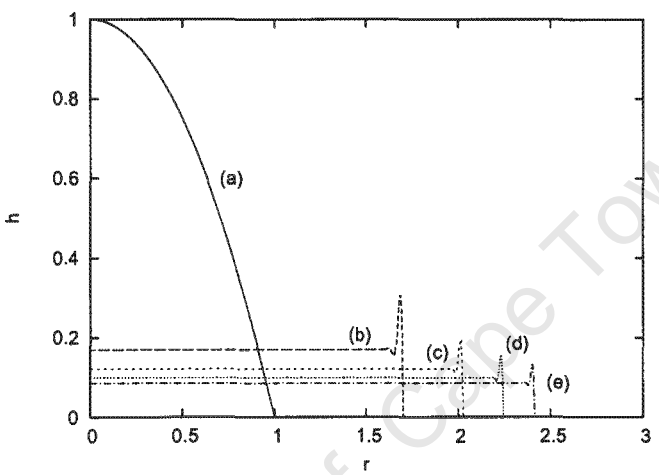

Figure 3.20: Evolution of Newtonian film $t = 25, 50, 75, 100$.

It can be seen from figure 3.20 that the Newtonian model predicts film profiles that continue to thin uniformly but ever more slowly with increasing t. Thus, if the initial film is constant the film would continue to thin uniformly with time. The results further show that the capillary ridge reduces with decreasing profiles, *i.e* it is proportional to the film height.

3.8 Conclusion

Equations modelling the flow of a thin axisymmetric Newtonian fluid layer on a rotating disk under the influence of centrifugal force, surface tension and gravity have been studied in this chapter. A mathematical model for this type of flow is developed.

When surface tension and gravity are neglected from the derived governing equation, the reduced form or the Emslie-Bonner-Peck model is obtained. We examined under what conditions formation of vertical fronts are likely to occur. Neglect of surface tension in this reduced form contributes to formation of waves for certain initial film profiles.

A stability analysis was undertaken to study the evolution of waves when surface tension and gravity are included and how these affect the stability of a film on a rotating substrate. The stability analysis carried out on an axisymmetric flow of a thin viscous Newtonian fluid layer shows that spin coating is a stable method with regard to linear disturbances, for an initially constant film. Surface tension and gravity (when the film is on top of the disk) contribute to this stability.

A numerical scheme was developed to solve the governing equation. The equation governing the flow of fluid on a rotating substrate is highly non-linear and contains a fourth order term. This governing equation was discretised using a semi-implicit numerical scheme that involved splitting the flux into two components. The terms involving high-order derivatives of the fluid height were estimated implicitly while the rest of the terms were calculated explicitly. This is the first time that such a scheme has been used in modelling spin coating. Mass conservation and convergence of the solution were ensured and reasonably satisfied by the developed scheme. In addition, the results obtained compare well with the Emslie-Bonner-Peck model.

Simulations were performed using parameter values of the order of magnitude found in experimental and spin coating applications, such as CD manufacturing. An initial profile was imposed and profiles generated at four time intervals as representative of the process. The fluid profiles predicted by these simulations compare well with existing simulations or experiments. From the figures in Section 3.7, it is easily verified that spin coating results in uniform films with films becoming more uniform as spinning is continued, regardless of the values of B and C used. Inclusion of surface tension and gravity however, does affect the shape of the film. The characteristic capillary ridge develops at the moving front where the curvature is high. Addition of gravity tends to smooth the film profile. This is most obvious at the moving front. Increasing gravity effects in the model also results in slightly reduced film profiles for relatively thicker films. The results further show that surface tension reduces the spread rate while gravity has the opposite effect.

The developed numerical scheme will be modified later to include non-Newtonian flows on a rotating disk.

Chapter 4

Role of Coriolis force on rotating thin films

4.1 Introduction

The role of the Coriolis force on the evolution of a thin film of Newtonian fluid on a rotating disk has been investigated and attracted debate [52, 60, 66, 82]. In [60], film flow subject to the lubrication restrictions is considered, where the dominant balance in the radial direction is between viscous resistance, centrifugal force and Coriolis force. In the azimuthal direction the balance is between viscous resistance and Coriolis force. In [66], it is shown that within the restrictions of lubrication theory the Coriolis force has the same order of magnitude as inertia in the radial direction. The basic assumption of lubrication theory is that the inertia terms in the Navier-Stokes equation can be neglected. Since, in the radial direction the Coriolis force has the same magnitude as inertia, any theory working within the restrictions of lubrication theory should therefore neglect the Coriolis force in the radial flow equation.

The conclusion in [66] is disputed in [52], where the authors carry out an experimental and analytical investigation of a rotating thin layer of fluid. According to their findings, existing analytical results which have centrifugal force as the only driving force, predict film heights which are slightly lower than experimental values near the centre of the disk (typically the worst error is around 10%). They conclude that the Coriolis force must be included into the radial velocity equation to accurately describe film heights.

In this chapter, we will show that both the conclusion in [52] and the analysis leading up

to it are flawed. The excellent agreement between the analytical and experimental results actually occurs because they do not correctly solve their model. Their analytical solution contains four unknowns which are determined uniquely by their four specified boundary conditions. However, they do not apply the boundary conditions. Instead they use a result of Lepehin & Riabchuk [51] obtained by assuming a power law relation and then fitting this to experimental data, hence the good agreement.

The aim of this chapter is to present an analysis that shows that the Coriolis force, together with the inertia term may only enter as a correction term to the classical solution of the height for the free surface. The experimental results detailed in [52] do indicate that as the film height increases, the classical relation between film height and flux will slightly under-predict the true height. By considering the neglected terms in the Navier-Stokes equations in a systematic manner we show that the appropriate terms to correct the solution are both Coriolis and inertia (not Coriolis alone). Including both sets of terms as corrections to the classical solution acts to increase the theoretical film height and so bring results closer to the experimental values.

In the following section we detail the governing equations. We then non-dimensionalise the system in order to highlight the appropriate dominant terms and solve the system to show how the classical solution may be modified to increase the film height prediction near the axis. In Section 4.3 we explain in more detail the errors in the analysis of Leshev & Peev and give the correct solution based on their balance. Finally we compare our results with the experimentally obtained formula of [51].

4.2 Derivation of the model

The physical set-up and co-ordinate system for the model are shown in Figure 4.1.

The components of the Navier-Stokes equations in the radial, azimuthal and z directions for a steady axisymmetric flow are:

$$u\frac{\partial u}{\partial r} + w\frac{\partial u}{\partial z} - \frac{v^2}{r} - 2\Omega v - \Omega^2 r = -\frac{1}{\rho}\frac{\partial p}{\partial r} + \nu\left(\frac{\partial^2 u}{\partial r^2} + \frac{1}{r}\frac{\partial u}{\partial r} + \frac{\partial^2 u}{\partial z^2} - \frac{u}{r^2}\right) \tag{4.1}$$

$$u\frac{\partial v}{\partial r} + w\frac{\partial v}{\partial z} + \frac{uv}{r} + 2\Omega u = \nu\left(\frac{\partial^2 v}{\partial r^2} + \frac{1}{r}\frac{\partial v}{\partial r} + \frac{\partial^2 v}{\partial z^2} - \frac{v}{r^2}\right) \tag{4.2}$$

$$u\frac{\partial w}{\partial r} + w\frac{\partial w}{\partial z} = -\frac{1}{\rho}\frac{\partial p}{\partial z} + \nu\left(\frac{\partial^2 w}{\partial r^2} + \frac{\partial^2 w}{\partial z^2}\right) \tag{4.3}$$

where the notation is the same as that of Section 3.3. For an incompressible fluid the equation

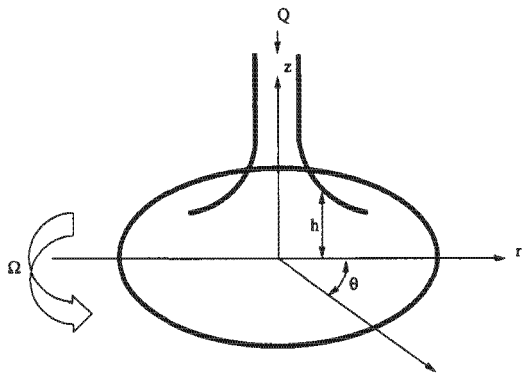

Figure 4.1: Coordinate system

of continuity is

$$\frac{1}{r}\frac{\partial}{\partial r}(ru) + \frac{\partial w}{\partial z} = 0\,. \tag{4.4}$$

These equations must be solved subject to the same boundary conditions as in Section 3.3 *i.e.* no-slip at the solid-liquid interface, zero shear stress and the standard kinematic condition holds at the free surface. The only difference is that at the free surface, $z = h(r)$, the fluid pressure equals the constant atmospheric pressure (surface tension is neglected)

$$p \;=\; p_0\,. \tag{4.5}$$

Non-dimensional analysis

Using the scales introduced in Section 3.3, we non-dimensionalise as before. Replacing dimensional variables in equations (4.1) - (4.3) with non-dimensional ones and dropping the primes to simplify the notation, the equations now become

$$\begin{aligned}\delta^2 Re\left(u\frac{\partial u}{\partial r} + w\frac{\partial u}{\partial z}\right) - \frac{H^2V^2}{\nu UL}\frac{v^2}{r} \;&-\; \frac{2\Omega V H^2}{\nu U}v - \frac{\Omega^2 LH^2}{\nu U}r = -\frac{1}{\rho}\frac{\partial p}{\partial r} \\ &+\; \delta^2\frac{\partial^2 u}{\partial r^2} + \frac{\delta^2}{r}\frac{\partial u}{\partial r} + \frac{\partial^2 u}{\partial z^2} - \delta^2\frac{u}{r^2} \end{aligned} \tag{4.6}$$

$$\delta^2 Re\left(u\frac{\partial v}{\partial r} + w'\frac{\partial v}{\partial z} + \frac{uv}{r}\right) + \frac{2\Omega U H^2}{\nu V}u \;=\; \delta^2\frac{\partial^2 v}{\partial r^2} + \frac{\delta^2}{r}\frac{\partial v}{\partial r} + \frac{\partial^2 v}{\partial z^2} - \delta^2\frac{v}{r^2} \tag{4.7}$$

$$\delta^4 Re\left(u\frac{\partial w}{\partial r} + w\frac{\partial w}{\partial z}\right) \;=\; -\frac{1}{\rho}\frac{\partial p}{\partial z} + \delta^4\frac{\partial^2 w}{\partial r^2} + \delta^2\frac{\partial^2 w}{\partial z^2}\,. \tag{4.8}$$

In the following we will use the values employed in the experiments described in [52] and shown in Table 4.1. The height and length-scales are of the order of magnitude exhibited in the experiments. The viscosity is taken for water.

Ω	ν	Q	H	L
10.47 rad/s	$1 \times 10^{-6}\mathrm{m}^2/\mathrm{s}$	$5.33 \times 10^{-6}\mathrm{m}^3/\mathrm{s}$	$1 \times 10^{-4}\mathrm{m}$	0.1m

Table 4.1: Experimental values for different parameters

Under the lubrication assumptions $\delta^2, \delta^2 Re \ll 1$ and so a number of terms in (4.6–4.8) are negligible. Using the values listed above we obtain $\delta^2 \approx 10^{-6}$, $Re = Q/\nu H \approx 5 \times 10^4$ and $\delta^2 Re \approx 5 \times 10^{-2}$. This indicates that neglecting terms of order δ^2 will lead to errors of around $10^{-4}\%$. Neglecting terms of order $\delta^2 Re$ will lead to typical errors of around 5%. If we were to focus on a region closer to the axis then the height scale would increase and the length-scale decrease. The contribution of terms involving $\delta^2 Re$ would be even larger and, in particular, could easily account for a 10% discrepancy between experiment and theory near the axis.

Since $\delta^2 Re \gg \delta^2$ we will now neglect terms of $\mathcal{O}(\delta^2)$ but retain terms of $\mathcal{O}(\delta^2 Re)$. We will also focus on flows where the centrifugal force drives the outward flow. This is described by the final term on the left hand side of equation (4.6) which shows that the typical velocity $U = \Omega^2 L H^2/\nu$. Substituting the appropriate values gives $U \sim 0.1\mathrm{m/s}$. We can verify that the average velocity is $U = Q/(2\pi LH)$. Using the experimental values again gives $U \sim 0.1\mathrm{m/s}$. Since the two estimates for U are of the same magnitude it may be inferred that centrifugal force does drive the outward flow in the experiments reported in [52].

There are three terms involving the azimuthal velocity scale V in equations (4.6, 4.7). These show that there are three possible azimuthal velocity scales:

$$V_1 = \frac{2\Omega U H^2}{\nu} \qquad V_2 = \frac{\nu U}{2\Omega H^2} \qquad V_3 = \sqrt{\frac{\nu U L}{H^2}}\,.$$

We will now investigate each case.

Case 1

The scaling $V = V_1$ is the case investigated by Myers & Charpin [66] and similar to the azimuthal velocity scale used by Reisfeld *et al.* [77]. In this situation the governing equations become:

$$\frac{\partial^2 u}{\partial z^2} = \frac{\partial p}{\partial r} - r + \epsilon\left(u\frac{\partial u}{\partial r} + w\frac{\partial u}{\partial z}\right) - 4\epsilon v - 4\epsilon^2\frac{v^2}{r} + \mathcal{O}(\delta^2) \tag{4.9}$$

$$\frac{\partial^2 v}{\partial z^2} = u + \epsilon\left(u\frac{\partial v}{\partial r} + w\frac{\partial v}{\partial z} + \frac{uv}{r}\right) + \mathcal{O}(\delta^2) \tag{4.10}$$

$$\frac{\partial p}{\partial z} = \mathcal{O}(\delta^2, \delta^2\epsilon)\ , \tag{4.11}$$

where $\epsilon = (H/E)^4$. In keeping with previous work we adopt the convenient notation where the reduced Reynolds number $\delta^2 Re$ is expressed as $(H/E)^4$, where $E = \sqrt{\nu/\Omega}$ is the Ekman number.

Equation (4.11) indicates that $p = p(r)$. In the absence of gravity and surface tension, boundary condition (4.5) then shows that p is constant everywhere. The pressure gradient in (4.9) may therefore be set to zero. The same is true for all following cases and so p will be neglected from now on. Equation (4.9) indicates that the outward flow is governed (to leading order) by the balance between viscous resistance and centrifugal force. The first order correction to this, of $\mathcal{O}(\epsilon)$, is caused by the inertia and Coriolis effects ($uu_r + wu_z$ and $4v$ respectively). Equation (4.10) shows that the leading order balance in the azimuthal direction is between viscous resistance and Coriolis force, with a first order correction due to inertia ($uv_r + wv_z + uv/r$).

Since $\epsilon \ll 1$ it is reasonable to look for a series solution of the form

$$u = u_0 + \epsilon u_1 + \mathcal{O}(\epsilon^2)$$
$$v = v_0 + \epsilon v_1 + \mathcal{O}(\epsilon^2)\ .$$

Substituting into the above equations gives the leading order system

$$\frac{\partial^2 u_0}{\partial z^2} = -r \qquad \frac{\partial^2 v_0}{\partial z^2} = u_0\ . \tag{4.12}$$

This is subject to the no-slip and zero shear stress boundary conditions, resulting in

$$u_0 = -\frac{1}{2}r\left(z^2 - 2zh\right) \tag{4.13}$$

$$v_0 = -\frac{rz}{24}\left(z^3 - 4z^2h + 8h^3\right)\ . \tag{4.14}$$

Integrating the continuity equation then gives the leading order velocity in the z-direction

$$w_0 = -\frac{1}{6}z^2\left(-2z + 6h + 3r\frac{\partial h}{\partial r}\right)\ . \tag{4.15}$$

The first order problem is

$$\frac{\partial^2 u_1}{\partial z^2} = u_0\frac{\partial u_0}{\partial r} + w_0\frac{\partial u_0}{\partial z} - 4v_0 \tag{4.16}$$

$$\frac{\partial^2 v_1}{\partial z^2} = u_1 + u_0\frac{\partial v_0}{\partial r} + w_0\frac{\partial v_0}{\partial z} + \frac{u_0 v_0}{r}\,, \tag{4.17}$$

which are also subject to no-slip and zero shear stress conditions. Our primary interest is in improving the relation between the flux and height. This requires calculating u_1. Since equation (4.16) only involves the leading order velocities, u_0, v_0, w_0, we may neglect the equation for v_1. Integrating (4.16) leads to

$$u_1 = \frac{r}{60}\left(\frac{z^6}{6} - hz^5 + \frac{40}{3}h^3z^3 + \frac{5}{2}hz^4 r\frac{\partial h}{\partial r} - 36h^5 z - 10h^4 r\frac{\partial h}{\partial r}z\right)\,. \tag{4.18}$$

The flux is determined by

$$\begin{aligned}\frac{Q}{2\pi r} &\approx \int_0^h u_0 + \epsilon u_1\, dz \\ &= \frac{1}{3}h^3 r - \frac{\epsilon}{2520}h^3 r\left(622h^4 + 189rh^3\frac{\partial h}{\partial r}\right)\,.\end{aligned} \tag{4.19}$$

This provides a relation between the flux and film height h which could be solved numerically. However if we let $h = h_0 + \epsilon h_1$ then we can obtain an analytical solution within the accuracy already specified:

$$\frac{Q}{2\pi r} = \frac{1}{3}rh_0^3 + rh_0^2\left(h_1 - \frac{3}{40}rh_0^4\frac{\partial h_0}{\partial r} - \frac{311}{1260}h_0^5\right)\epsilon + \mathcal{O}(\epsilon^2)\,. \tag{4.20}$$

Hence

$$h_0 = \left(\frac{3Q}{2\pi r^2}\right)^{1/3} \qquad h_1 = h_0^4\left(\frac{3}{40}r\frac{\partial h_0}{\partial r} + \frac{311}{1260}h_0\right)\,. \tag{4.21}$$

Substituting for h_0 in the second equation and rearranging shows $h_1 = 62h_0^5/315$. The height is therefore given by

$$h = h_0\left(1 + \epsilon\frac{62}{315}h_0^4\right) = \left(\frac{3Q}{2\pi r^2}\right)^{1/3}\left(1 + \epsilon\frac{62}{315}\left(\frac{3Q}{2\pi r^2}\right)^{4/3}\right)\,. \tag{4.22}$$

So, with this choice of scaling, the Coriolis term enters the azimuthal velocity equation, (4.10), at leading order, *i.e.* the Coriolis force is the dominant driving force in that direction. However, it only enters the radial velocity equation (4.9) at $\mathcal{O}(\epsilon)$. The inertia terms are also of $\mathcal{O}(\epsilon)$, indicating that the Coriolis force has the same magnitude as the inertia terms on

the radial flow. Studying the first order equations (4.16), (4.17) allows us to obtain the correction to the film height due to Coriolis and inertia terms, leading to equation (4.22).

The leading order solution, h_0, is exactly that found in the classical, purely centrifugal driven studies of Emslie *et al* [25] and Rauscher [75]. Since $h_1 \propto h_0^5 > 0$ we can see that the inclusion of the first order terms increases the film height (in keeping with the experimental observations).

Case 2

Now consider the case where $V = V_2 = \nu U/2\Omega H^2$. This reduces the governing equations to

$$\frac{\partial^2 u}{\partial z^2} = -r - v - \frac{v^2}{4r} + \epsilon\left(u\frac{\partial u}{\partial r} + w\frac{\partial u}{\partial z}\right) \tag{4.23}$$

$$\frac{\partial^2 v}{\partial z^2} = 4\epsilon u + \epsilon\left(u\frac{\partial v}{\partial r} + w\frac{\partial v}{\partial z} + \frac{uv}{r}\right) . \tag{4.24}$$

Again we look for a series solution. The leading order equations are

$$\frac{\partial^2 u_0}{\partial z^2} = -r - v_0 - \frac{v_0^2}{4r} \tag{4.25}$$

$$\frac{\partial^2 v_0}{\partial z^2} = 0 . \tag{4.26}$$

It now appears that the leading order radial flow is determined by the balance between viscous resistance, centrifugal and Coriolis forces. The azimuthal flow has no leading order balance. Since there is no driving force the solution to (4.26), subject to no-slip and zero shear stress is that $v_0 = 0$. In which case the radial equation, (4.25), reduces to a balance between viscous resistance and centrifugal force as studied in the previous case. Since the leading order velocity w_0 depends solely on u_0, both u_0 and w_0 are the same as in the previous section.

At first order

$$\frac{\partial^2 u_1}{\partial z^2} = \left(u_0\frac{\partial u_0}{\partial r} + w_0\frac{\partial u_0}{\partial z}\right) - v_1 \tag{4.27}$$

$$\frac{\partial^2 v_1}{\partial z^2} = 4u_0 . \tag{4.28}$$

Now to determine u_1 we must first determine v_1. However, in this case we note that v_1 is simply four times v_0 from the previous section, see equation (4.12), consequently u_1 satisfies exactly the same equation as before, equation (4.16). To first order the velocities u_1 are therefore identical for the two cases and so the same expressions for height and flux will be obtained.

Case 3

When $V = V_3 = \sqrt{\nu UL/H^2}$ we obtain the same leading order equations as in Case 2. At first order

$$\frac{\partial^2 u_1}{\partial z^2} = \left(u_0 \frac{\partial u_0}{\partial r} + w_0 \frac{\partial u_0}{\partial z}\right) - 2v_1 \tag{4.29}$$

$$\frac{\partial^2 v_1}{\partial z^2} = 2u_0 \, . \tag{4.30}$$

Again it is obvious that the same result as in Case 1 will be obtained.

In summary, the effect of the Coriolis force enters through three terms in the Navier-Stokes equations. Each one has been investigated and in each case the Coriolis force is of the same order of magnitude as inertia. Although in Cases 2, 3 it appears Coriolis enters the leading order equations these terms actually reduce to zero. Within the restrictions of lubrication theory, the Coriolis force is therefore negligible. However, if its effect is to be investigated, in order to correct the leading order theory, then inertia terms must also be included since these are of the same magnitude. The correct relation for $h(r)$, within lubrication theory, is determined by the classic relation for h_0 given by equation (4.21). For films where ϵ is relatively large, *i.e.* thick films, low viscosity fluids or very rapidly rotating films, then this classic expression may be corrected by the first order term to give a film height described by equation (4.22).

4.3 The model with centrifugal and Coriolis forces at leading order

Leshev & Peev [52] investigate a model with centrifugal and Coriolis forces entering the leading order balance. We will now go through the same type of model, but will not copy their analysis for the following reasons. Their governing equations have an incorrect sign for the Coriolis terms, the solution to the governing equations is incorrect (for both correct and incorrect versions of the governing equations) and if their subsequent boundary conditions are imposed correctly the solution is that their radial and azimuthal velocities are zero everywhere. Their expression for film height variation in terms of the model parameters is obtained by integrating the velocity to obtain the flux and then substituting an approximation to the constants of integration (which as mentioned in their model should be zero, in the correct model they are already uniquely determined). The dependence on ω and ν does

not follow between the equations but the final expression, which is taken from [51], does agree well with experiments.

Momoniat & Mason [60] have analysed the same leading order balance as Leshev & Peev. An analysis of their work, which is more systematic, shows that the balance occurs by assuming the azimuthal velocity scale is of the same order as the radial velocity scale, *i.e.* the fluid moves round at a similar velocity to that at which it is thrown outwards. In a thin film, subject to zero shear stress at the free surface, it is clear that in the steady-state the fluid will move around at a similar velocity to the substrate, so the relative azimuthal velocity must be small. In fact, this balance of terms is equivalent to balancing the pressure gradient $r^{-1}\partial p/\partial\theta$ with viscous resistance in the azimuthal direction. Since the flow is assumed to be axisymmetric this pressure gradient is zero and the azimuthal velocity scale should in fact be zero (as expected on physical grounds).

In the current notation Momoniat & Mason [60] study the leading order system

$$\frac{\partial^2 u}{\partial z^2} = -r - 2\left(\frac{H}{E}\right)^2 v = -r - 2\epsilon^{1/2} v \tag{4.31}$$

$$\frac{\partial^2 v}{\partial z^2} = 2\left(\frac{H}{E}\right)^2 u = 2\epsilon^{1/2} u \,. \tag{4.32}$$

Subject to no-slip and zero shear stress boundary conditions this results in

$$u = \frac{r}{2\sqrt{\epsilon}}\left[\frac{\sinh(\epsilon^{1/4}z)\sin(\epsilon^{1/4}(2h-z)) + \sin(\epsilon^{1/4}z)\sinh(\epsilon^{1/4}(2h-z))}{\cosh(2\epsilon^{1/4}h) + \cos(2\epsilon^{1/4}h)}\right] \tag{4.33}$$

$$v = \frac{r}{2\sqrt{\epsilon}}\left[\frac{\cosh(\epsilon^{1/4}z)\cos(\epsilon^{1/4}(2h-z)) + \cos(\epsilon^{1/4}z)\cosh(\epsilon^{1/4}(2h-z))}{\cosh(2\epsilon^{1/4}h) + \cos(2\epsilon^{1/4}h)} - 1\right]. \tag{4.34}$$

Integrating the radial velocity across the film leads to the flux expression

$$Q = \frac{\pi r^2}{2\epsilon^{3/4}}\frac{\sinh(2\epsilon^{1/4}h) - \sin(2\epsilon^{1/4}h)}{\cosh(2\epsilon^{1/4}h) + \cos(2\epsilon^{1/4}h)} = \frac{\pi r^2}{2\epsilon^{3/4}} g(\epsilon^{1/4}h) \,. \tag{4.35}$$

As $\epsilon^{1/4}h \to 0$ the function $g \to 4\epsilon^{3/4}h^3/3$ and

$$Q \to \frac{2\pi r^2}{3}h^3 \qquad\qquad h \to \left(\frac{3Q}{2\pi r^2}\right)^{1/3} \,. \tag{4.36}$$

This is the leading order result given by equation (4.21).

Equations (4.33) - (4.35) represent the velocities and flux that Leshev & Peev should obtain through their analysis. Note, there are no free parameters in the expression for flux, since it results from integrating two second order equations and applying four boundary conditions.

However, when they write down an expression for film height as a function of the model parameters they obtain excellent agreement with experiment. This is achieved by not applying their own boundary conditions. By neglecting the specified conditions they retain a degree of freedom and may therefore choose an appropriate constant in the flux expression (4.36) to match the experimental results. Their result does not follow from the model (4.31, 4.32).

Now consider the approximation used by Leshev & Peev and derived by Lepehin & Riabchuk, namely that $Q/r^2 \sim h^{2.87}$. Equation (4.35) gives $Q/r^2 \sim g(h)$ and the standard solution is $Q/r^2 \sim h^3$. These three relations are shown on figure 4.3 for $h \in [0, 1.3]$ (corresponding to the appropriate experimental range). It is clear that for small h all curves are similar. As h increases $h^{2.87}$ is obviously a better approximation to h^3 than it is to $g(h)$. Of course an appropriate constant could be introduced $Q/r^2 \sim Ah^{2.87}$ to force the curve closer to $g(h)$ in a given region, however, the general form of g is different and good agreement will never be achieved over a large range of h. Therefore the power law fit, $h^{2.87}$, is better suited as a correction to h^3 than $g(h)$ and consequently the standard solution should provide a better approximation to the film height than that with Coriolis at leading order.

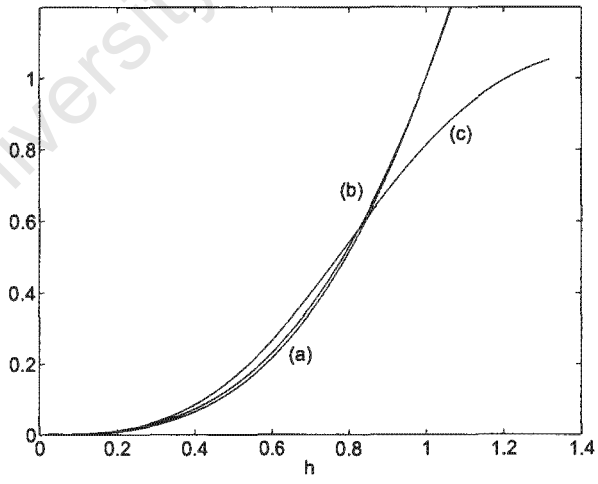

Figure 4.2: Comparison of formulae for Q/r^2, a) h^3, b) $h^{2.87}$, c) $g(h)$.

4.4 Dimensional results

The model described by equation (4.22) may be written in terms of dimensional variables by substituting back for the appropriate scales:

$$h = h_0\left(1+\frac{62}{315}\frac{\Omega^2 h_0^4}{\nu^2}\right) = \left(\frac{3\nu Q}{2\pi\Omega^2 r^2}\right)^{1/3}\left(1+\frac{62}{315}\frac{\Omega^2}{\nu^2}\left(\frac{3\nu Q}{2\pi\Omega^2 r^2}\right)^{4/3}\right) . \tag{4.37}$$

We now see that the leading order solution also depends on the fluid viscosity and rotation rate, $h \sim \nu^{1/3}, \Omega^{-2/3}$. The correction to this standard relation, proportional to h_0^5, shows a different dependence on the fluid parameters, $h_1 \sim \nu^{-1/3}, \Omega^{-4/3}$. The model described in Section 4.3 becomes

$$\begin{aligned} Q &= \frac{\pi r^2}{2}(\nu\,\Omega)^{1/2}\,\frac{\sinh(2h/E)-\sin(2h/E)}{\cosh(2h/E)+\cos(2h/E)} \\ &= \frac{\pi r^2}{2}(\nu\,\Omega)^{1/2} g(h/E) . \end{aligned} \tag{4.38}$$

This clearly exhibits a much more complex relation between the film height and fluid parameters. As the film height decreases both models reduce to the standard solution

$$h = h_0 = \left(\frac{3\nu Q}{2\pi\Omega^2 r^2}\right)^{1/3} . \tag{4.39}$$

Finally, according to [52] the result obtained [51] is

$$h = 0.886 Q^{0.348}\nu^{0.328}\Omega^{-0.676}r^{-0.7} , \tag{4.40}$$

which fits well with the experimental data presented in [52].

Figure 4.3 contains four curves depicting the various solutions. The data is taken from the experiments described in [52], with $Q = 5.33\times10^{-6}\mathrm{m}^3/\mathrm{s}$, $\nu = 1\times10^{-6}\mathrm{m}^2/\mathrm{s}$, $\Omega = 10.47\,\mathrm{rad/s}$ (see their Figure 3, curve (a)). Curves (a) and (b) are the classical and corrected solutions given by equations (4.39), (4.37) respectively. For small h (large r) these solutions are indistinguishable. As r decreases curve (b) can be clearly seen to have larger values than curve (a). When $r \approx 3.5$ cm curve (b) crosses curve (c), which represents the experimental power law formula. The final curve, (d), the solution of (4.38), is indistinguishable from (a) and (b) for large r. In fact it closely follows (b) as the centre is approached but crosses curve (c) earlier, around $r = 4\,\mathrm{cm}$, and then rapidly increases above all the other curves.

In figures 4.4 and 4.5 we present two more results, where curves (a-d) represent the same formula as in figure 4.3. The first uses experimental data $Q = 5.33\times10^{-6}\mathrm{m}^3/\mathrm{s}$, $\nu =$

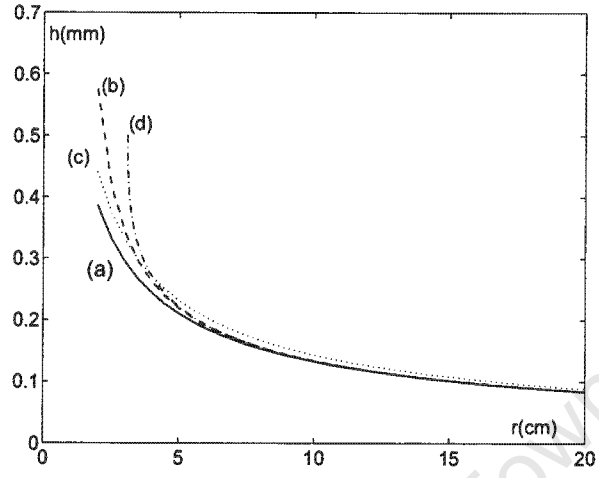

Figure 4.3: Comparison of height formulae with $Q = 5.33 \times 10^{-6}\mathrm{m}^3/\mathrm{s}$, $\nu = 1 \times 10^{-6}\mathrm{m}^2/\mathrm{s}$, $\Omega = 10.47\,\mathrm{rad/s}$.

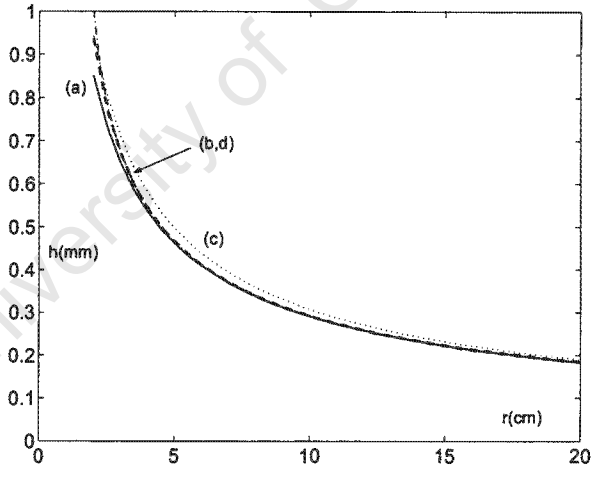

Figure 4.4: Comparison of height formulae with $Q = 5.33 \times 10^{-6}\mathrm{m}^3/\mathrm{s}$, $\nu = 1.063 \times 10^{-5}\mathrm{m}^2/\mathrm{s}$, $\Omega = 10.47\,\mathrm{rad/s}$.

$1.063 \times 10^{-5}\mathrm{m}^2/\mathrm{s}$, $\Omega = 10.47\,\mathrm{rad/s}$, (see [52] figure 3c) the second has increased flux, viscosity and rotation $Q = 1 \times 10^{-5}\mathrm{m}^3/\mathrm{s}$, $\nu = 5 \times 10^{-6}\mathrm{m}^2/\mathrm{s}$, $\Omega = 50\,\mathrm{rad/s}$. In figure 4.4 again we see that all curves coincide for large r. As r decreases (a,b,d) are indistinguishable until around $r = 6\,\mathrm{cm}$, subsequently curves (b,d) move closer to the experimental/data fitted result. These two curves only differ at the very smallest values of r where curve (d) increases

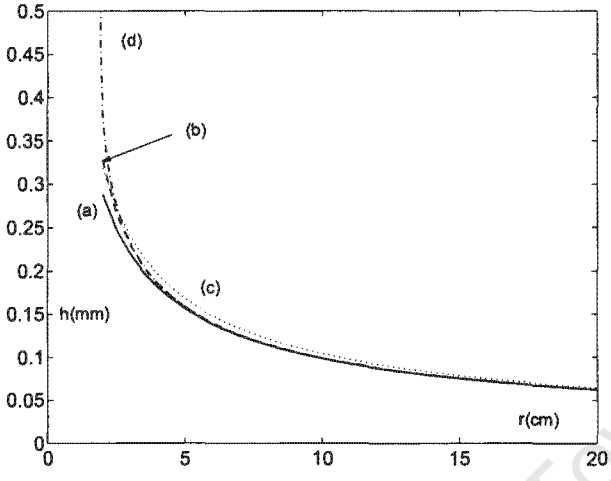

Figure 4.5: Comparison of height formulae with $Q = 1 \times 10^{-5}\mathrm{m}^3/\mathrm{s}$, $\nu = 5 \times 10^{-6}\mathrm{m}^2/\mathrm{s}$, $\Omega = 50\,\mathrm{rad/s}$.

rapidly above all other results. Figure 4.5 is similar, but now it is clear that the result including Coriolis rapidly increases above the other curves, whereas the corrected model comes very close to the power law formula.

The range of validity of the above solutions is an important issue. As discussed earlier, all the analytical models require δ^2, $\delta^2 Re \ll 1$. As the centre is approached, $r \to 0$, the $1/r^n$ dependence means that all the quoted solutions (including the experimentally verified one) will become invalid and so it is important for anyone using these models to verify that the restrictions are not broken. When using (4.37) the correction term brings in a further restriction. Equation (4.37) is derived on the assumption that the correction is small, *i.e.*

$$\frac{62}{315}\frac{\Omega^2}{\nu^2}\left(\frac{3\nu Q}{2\pi\Omega^2 r^2}\right)^{4/3} = \frac{62}{315}\Omega^{-2/3}Q^{4/3}\nu^{-2/3}r^{-4/3} \ll 1\ .$$

It is not difficult to construct an example where this does not hold. In figure 4.6 we keep all parameters the same as in figure 4.5 except for the flux which increases by a factor of 5, $Q = 5 \times 10^{-5}\mathrm{m}^3/\mathrm{s}$. The 'small' term now equals 1.16 at $r = 2\,\mathrm{cm}$ and the correction term is of the same magnitude as the leading order solution, hence the model is clearly invalid. From the figure the result appears reasonable for $r > 4\,\mathrm{cm}$ and it can be verified that when $r = 4\,\mathrm{cm}$ the correction term is 0.18 and indeed the approximation can still be applied there, however it clearly degrades rapidly as r decreases.

Increases in Q or decreases in ν, Ω and r all act to increase the size of the correction term

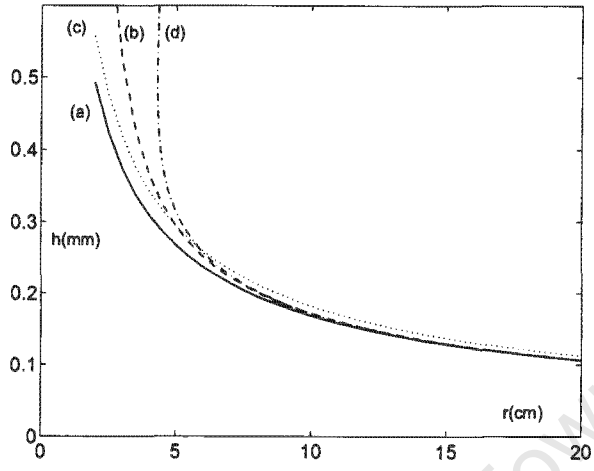

Figure 4.6: Comparison of height formulae with $Q = 5 \times 10^{-5}\mathrm{m}^3/\mathrm{s}$, $\nu = 5 \times 10^{-6}\mathrm{m}^2/\mathrm{s}$, $\Omega = 50\,\mathrm{rad/s}$.

and so invalidate the model. However, this was discussed in the initial stages of the model. When the correction term becomes large it mean that the Coriolis force is important and if this must be included at leading order then so must inertia. So, if the corrected model is invalid then the model with Coriolis at leading order is also invalid. This is clear from figure 4.6 where curve (d) is an even worse approximation to the power law curve than the corrected model.

4.5 Conclusion

The main result of this chapter is that the Coriolis force does not affect the leading order relation between flux and film height obtained via lubrication theory. However, together with inertia the Coriolis force may enter as a correction term to the classical solution.

The classical solution which requires a thin fluid layer, cannot hold throughout the domain of interest. In particular, for the current problem, fluid is poured on near the centre of the disk. High above the disk the flow will be described by a standard water jet solution and so the fluid does not react to the disk rotation. As the disk is approached the fluid will start to rotate. The centrifugal force, which is proportional to the distance from the axis, will be small in this region and therefore the dominant balance will be between viscous resistance, inertia and Coriolis forces. The classical rotating thin film solution describes the flow away

from this region. In order to determine a full solution these two regions must be matched by at least one intermediate region, where the dominant balance must involve all of the above terms.

When using thin film models, far from the centre the classical solution will give a good approximation to the true film height. The current analysis permits the analytical solution to be taken closer to the centre but it will also break down. This will occur when the correction term becomes of the same order as the classical solution.

Chapter 5

Rotating non-Newtonian thin films

5.1 Introduction

In Chapter 1, we highlighted some industrial applications of spin coating. These provided a motivation for our study. So far our analysis has focused on Newtonian flow models. However, in reality many of these applications involve non-Newtonian fluids. For example, the fluids that are used as coating materials in the CD manufacturing and the electronics industries include photoresist, acrylic plastic, organic dye polymer and so forth, all of which are non-Newtonian [2, 6, 58]. Therefore, in this chapter, we will focus on spin coating of non-Newtonian fluids and highlight how their behaviour differs from that of Newtonian fluids, and how the different viscosity models compare with each other. We are particularly interested in investigating the effect of including surface tension and gravity on the resulting film profiles in non-Newtonian models.

In this chapter, we consider spin coating of non-Newtonian fluids described by some commonly used non-Newtonian viscosity models, namely power-law and Ellis models (as detailed in Section 1.3). These models are used to describe the dynamic viscosity of shear-thinning fluids. The power-law is considered because several analytical solutions are possible as a result of its simplicity. Its popularity too makes it a good starting point in the analysis, but we keep in mind its limitations *i.e.* the predicted apparent viscosity tending to infinity as shear rates approach zero [20]. The Ellis model is relatively easy to use and allows us to derive explicit expressions for the film height. Many analytical results are available for this model. A number of these analytical results can be found in [56].

In Section 5.2, we will derive governing equations for axisymmetric flow for thin power-law

and Ellis fluid layers, under the influence of centrifugal force, surface tension and gravity. A direct extension of the Newtonian scheme (that involves splitting of the flux) developed for Newtonian fluids in Chapter 3 is not possible to implement because of the expression for the flux in the non-Newtonian models. Therefore, the numerical scheme for Newtonian fluids will be modified to include non-Newtonian fluids, by introducing a normalisation of the flux. This results in a numerical scheme that is straightforward to implement as an extension of the Newtonian scheme.

In Section 5.3, the power-law version of the numerical scheme is developed and a number of tests carried out to validate the scheme. Simulations of the fluid height will be carried out for three values of the power-law index.

In Section 5.4, we will consider the modified numerical scheme and results for the Ellis model. The numerical results for the power-law and Ellis models will then be compared for thin film flow on a rotating disk, when surface tension and gravity are included in the models.

5.2 Governing equations

The Navier-Stokes equations for rotating incompressible fluids, including Coriolis and centripetal forces, were given in Section 3.2. Since we are dealing with non-Newtonian fluids, with a shear-rate-dependent viscosity, we now replace $\mu\nabla^2\mathbf{u}$ in equation (3.1) by $\nabla\cdot\tau$, where τ is the shear stress. The Navier-Stokes equations and continuity equations are therefore given by

$$\rho\left(\frac{\partial\mathbf{u}}{\partial t}+(\mathbf{u}\cdot\nabla)\mathbf{u}\right) = -\nabla p+\nabla\cdot\tau+\rho\left[2\Omega\times\mathbf{u}+\Omega\times(\Omega\times\mathbf{r})+\mathbf{g}\right], \tag{5.1}$$

$$\nabla\cdot\mathbf{u} = 0\,. \tag{5.2}$$

We now make the following assumptions:

- the plane is smooth and rotates at a constant angular velocity,
- gravitational and capillary forces are significant,
- air shear and evaporation are negligible,
- the liquid is non-Newtonian (shear-thinning), axisymmetric and thin.

Since the film is thin, the components u_z and τ_{rz} are much larger than the other respective components in (5.1). This is equivalent to u_{zz} dominating in the Newtonian case. In Chapter

4, it was shown that the Coriolis force does not affect the leading order relation between the flux and film height obtained via lubrication theory. Therefore, the Coriolis force is neglected.

The lubrication approximation to the Navier-Stokes equations (5.1) gives the leading order terms as

$$0 = -p_r + \frac{\partial}{\partial z}(\tau_{rz}) + \rho\Omega^2 r \,, \tag{5.3}$$

$$0 = -p_z - \rho g \,. \tag{5.4}$$

Integrating (5.3) subject to the no-shear boundary condition ($\tau_{rz} = \eta u_z = 0$) and equation (5.4), subject to the surface tension boundary condition (3.8) on the free surface, we have

$$\tau_{rz} = (-p_r + \rho\Omega^2 r)(h - z) \,, \tag{5.5}$$

$$p = p_a - \rho g(z - h) - \sigma\kappa \,. \tag{5.6}$$

Given that τ_{rz} is related to u_z, equation (5.5) can be integrated and the necessary boundary condition (no-slip) imposed, to obtain the radial velocity u. Integrating the continuity equation, and using Leibnitz's rule and the kinematic condition gives the fluid height as

$$\frac{\partial h}{\partial t} + \frac{1}{r}\frac{\partial (rQ)}{\partial r} = 0 \,, \tag{5.7}$$

where

$$Q = \int_0^h u \, \mathrm{d}z \,, \tag{5.8}$$

is the flux per unit length of circumference. To proceed further, we must relate the shear stress, τ_{rz}, to the velocity, u. This comes from the relation

$$\tau_{rz} = \eta u_z \,. \tag{5.9}$$

Therefore, we must consider the different viscosity models to determine η.

5.2.1 Power-law fluid

With power-law fluids, the dynamic viscosity may be described by

$$\eta = \kappa |\dot{\gamma}|^{n-1} \,, \tag{5.10}$$

where $\dot{\gamma}$ is the shear rate (for two-dimensional flow) given by

$$\dot{\gamma} = \sqrt{\left|\frac{\partial u}{\partial z}\right|^2 + \left|\frac{\partial u}{\partial r}\right|^2} \,. \tag{5.11}$$

Since we are dealing with a thin film, $|\partial u/\partial z| \gg |\partial u/\partial r|$ and we may set $\dot{\gamma} \approx \partial u/\partial z$.

Using equation (5.9) and the power-law constitutive model (5.10), equation (5.5) can then be written as

$$\kappa \left| \frac{\partial u}{\partial z} \right|^{n-1} \frac{\partial u}{\partial z} = (-p_r + \rho \Omega^2 r)(h - z) \; . \tag{5.12}$$

In this case, the velocity gradient is positive since the fluid is moving outwards. Therefore, equation (5.12) simplifies to

$$u_z = \left(\frac{(-p_r + \rho \Omega^2 r)(h - z)}{\kappa} \right)^{1/n} \; . \tag{5.13}$$

Integrating (5.13) with respect to z, subject to the no-slip boundary condition on the substrate, we obtain an expression for the velocity in terms of the unknown film height, h,

$$u = \frac{n}{n+1} \left(\frac{-p_r + \rho \Omega^2 r}{\kappa} \right)^{1/n} \left(h^{(n+1)/n} - (h - z)^{(n+1)/n} \right) \; . \tag{5.14}$$

The flux per unit length of circumference, Q^P, is then given by

$$Q^P = \int_0^h u \, \mathrm{d}z = \left(\frac{n}{2n+1} \right) \left(\frac{-p_r + \rho \Omega^2 r}{\kappa} \right)^{1/n} h^{(2n+1)/n} \; , \tag{5.15}$$

where

$$\frac{\partial p}{\partial r} = \rho g \frac{\partial h}{\partial r} - \sigma \frac{\partial}{\partial r} \left(\frac{1}{r} \frac{\partial}{\partial r} \left(r \frac{\partial h}{\partial r} \right) \right) \; . \tag{5.16}$$

The equation for the film thickness of a power-law thin film on a rotating disk, under the influence of surface tension and gravity, is therefore given by

$$\frac{\partial h}{\partial t} + \frac{1}{r} \frac{\partial}{\partial r} \left(\frac{n}{2n+1} \left[\frac{1}{\kappa} \left(\sigma \frac{\partial}{\partial r} \left(\frac{1}{r} \frac{\partial}{\partial r} \left(r \frac{\partial h}{\partial r} \right) \right) - \rho g \frac{\partial h}{\partial r} + \rho \Omega^2 r \right) \right]^{1/n} r h^{(2n+1)/n} \right) = 0 \; . \tag{5.17}$$

To non-dimensionalise this equation, we introduce characteristic scales used in Section 2.3 and let the characteristic velocity be

$$U = \left(\frac{\rho \Omega^2 L H^{n+1}}{\kappa} \right)^{1/n} \; . \tag{5.18}$$

Using non-dimensional parameters, the viscosity may be written as

$$\eta = \bar{\eta} \left(\frac{\partial u}{\partial z} \right)^{n-1} \; , \qquad \text{where} \qquad \bar{\eta} = \kappa \left(\frac{U}{H} \right)^{n-1} \tag{5.19}$$

is the viscosity scale. The non-dimensional form of (5.17) is then given as

$$\frac{\partial h}{\partial t} + \frac{1}{r} \frac{\partial}{\partial r} \left(\frac{n}{2n+1} \left[C \frac{\partial}{\partial r} \left(\frac{1}{r} \frac{\partial}{\partial r} \left(r \frac{\partial h}{\partial r} \right) \right) - B \frac{\partial h}{\partial r} + r \right]^{1/n} r h^{(2n+1)/n} \right) = 0 \; , \tag{5.20}$$

where $C = \sigma H^3 / \bar{\eta} U L^3$ and $B = \rho g H^3 / \bar{\eta} U L$. When $n = 1$, equation (5.20) reduces to the governing equation obtained for the Newtonian fluid in Chapter 3.

Analytical solution

When surface tension and gravity are neglected, it is possible to obtain an analytical solution similar to that obtained in Section 3.4 for the Newtonian model. In this case, neglecting surface tension and gravity reduces equation (5.20) to

$$\frac{\partial h}{\partial t} + \frac{1}{r}\frac{\partial}{\partial r}\left(\frac{n}{2n+1} r^{\frac{n+1}{n}} h^{\frac{2n+1}{n}}\right) = 0 \,. \tag{5.21}$$

This equation may be solved using the method of characteristics as follows: let $r = r(t)$ and $h = h(r(t), t)$ describe the evolution of the surface contour with time. By the chain rule,

$$\frac{dh}{dt}(r(t), t) = \frac{\partial h}{\partial t} + \frac{\partial h}{\partial r}\frac{dr}{dt} \,. \tag{5.22}$$

Equation (5.21) may be written as

$$-\frac{n+1}{2n+1} r^{\frac{1-n}{n}} h^{\frac{2n+1}{n}} = \frac{\partial h}{\partial t} + r^{\frac{1}{n}} h^{\frac{1+n}{n}} \frac{\partial h}{\partial r} \,. \tag{5.23}$$

Comparing (5.22) and (5.23), it follows that

$$\frac{dh}{dt} = -\frac{n+1}{2n+1} r^{\frac{1-n}{n}} h^{\frac{2n+1}{n}} \,, \qquad \frac{dr}{dt} = r^{\frac{1}{n}} h^{\frac{1+n}{n}} \,. \tag{5.24}$$

Assuming the solution has a form similar to the Newtonian case, we let

$$h(t) = h_0 (1 + \beta t)^{\gamma} \qquad r(t) = r_0 (1 + \beta t)^{\alpha} \,, \tag{5.25}$$

where (r_0, h_0) denotes the initial position of a particle ($t = 0$) and α, β and γ are unknown constants. Differentiating (5.25), we obtain

$$\frac{dh}{dt}(r(t), t) = h_0 \beta \gamma (1 + \beta t)^{\gamma - 1} \qquad \frac{dr}{dt} = r_0 \alpha \beta (1 + \beta t)^{\alpha - 1} \,. \tag{5.26}$$

Equating the expressions (5.24) and (5.26) and replacing h and r with equivalent terms from (5.25), we have the following relations:

$$\gamma - 1 = \alpha\frac{1-n}{n} + \gamma\frac{2n+1}{n} \,, \qquad \beta = \frac{1}{\alpha} r_0^{\frac{1-n}{n}} h_0^{\frac{n+1}{n}} \,,$$

$$\alpha - 1 = \frac{\alpha}{n} + \gamma\frac{1+n}{n} \,, \qquad \beta = -\frac{1}{\gamma}\frac{n+1}{2n+1} r_0^{\frac{1-n}{n}} h_0^{\frac{n+1}{n}} \,.$$

We have 4 equations for 3 unknowns, from which we obtain

$$\gamma = -\frac{n+1}{3n+1} \,, \qquad \alpha = \frac{2n+1}{3n+1} \qquad \text{and} \qquad \beta = \frac{3n+1}{2n+1} \,.$$

Note that this solution only exists if there is a certain relationship satisfied by h_0 and r_0, which in this case is

$$r_0^{\frac{1-n}{n}} h_0^{\frac{1+n}{n}} = \alpha\beta = 1. \tag{5.27}$$

Therefore, the analytical solution for (5.21) given by

$$h(t) = h_0 \left(1 + \frac{3n+1}{2n+1} h_0^{\frac{1+n}{n}} r_0^{\frac{1-n}{n}} t\right)^{-\frac{n+1}{3n+1}}, \tag{5.28}$$

$$r(t) = r_0 \left(1 + \frac{3n+1}{2n+1} h_0^{\frac{1+n}{n}} r_0^{\frac{1-n}{n}} t\right)^{\frac{2n+1}{3n+1}} \tag{5.29}$$

can be simplified further using the relationship (5.27). Equations (5.28) and (5.29) give the coordinates (r, h) after time t, of a particle initially at (r_0, h_0).

The analytical solution obtained using the method of characteristics will be compared with the numerical solution for power-law fluids in Section 5.3. This comparison will be useful in validating the numerical solution that will be developed.

5.2.2 Ellis fluid

For a fluid obeying the Ellis viscosity model, the viscosity is described by

$$\frac{1}{\eta} = \frac{1}{\eta_0} \left(1 + \left|\frac{\tau_{rz}}{\tau_{1/2}}\right|^{\alpha-1}\right) . \tag{5.30}$$

Combining equations (5.5) and (5.9) leads to

$$u_z = \frac{1}{\eta} \left(-p_r + \rho\Omega^2 r\right)(h - z) , \tag{5.31}$$

and using the Ellis constitutive law (5.30), we have

$$u_z = \frac{1}{\eta_0} \left(1 + \left|\frac{\tau_{rz}}{\tau_{1/2}}\right|^{\alpha-1}\right) (-p_r + \rho\Omega^2 r)(h - z) . \tag{5.32}$$

The velocity gradient is positive, since the fluid is moving outwards. Therefore, τ_{rz} is positive. Replacing τ_{rz} in (5.32) with ηu_z taken from (5.31) and rearranging gives

$$u_z = \frac{1}{\eta_0} \left[\left(-p_r + \rho\Omega^2 r\right)(h - z) + \frac{\left(-p_r + \rho\Omega^2 r\right)^{\alpha} (h - z)^{\alpha}}{\tau_{1/2}^{\alpha-1}}\right] . \tag{5.33}$$

Integrating this with respect to z, subject to the no-slip boundary condition, we have

$$u = \frac{1}{\eta_0}\left[\frac{1}{2}\left(-p_r + \rho\Omega^2 r\right)\left(2hz - z^2\right) + \frac{\left(-p_r + \rho\Omega^2 r\right)^{\alpha}\left(h^{\alpha+1} - (h-z)^{\alpha+1}\right)}{(\alpha+1)\,\tau_{1/2}^{\alpha-1}}\right], \tag{5.34}$$

from which an expression for the flux, Q^E, per unit length of circumference is obtained as

$$Q^E = \int_0^h u\,\mathrm{d}z = \frac{1}{\eta_0}\left[\frac{\left(-p_r + \rho\Omega^2 r\right)h^3}{3} + \frac{\left(-p_r + \rho\Omega^2 r\right)^{\alpha} h^{\alpha+2}}{(\alpha+2)\,\tau_{1/2}^{\alpha-1}}\right]. \tag{5.35}$$

The expression for the pressure gradient, p_r, is given by (5.16). The governing equation for the thickness of a thin film layer of an Ellis fluid on a rotating disk, under the influence of surface tension and gravity, may therefore be expressed as

$$\frac{\partial h}{\partial t} + \frac{1}{r}\frac{\partial\left(rQ^E\right)}{\partial r} = 0\,, \tag{5.36}$$

where

$$Q^E = Q^{E_1} + Q^{E_2},$$

the two components of the flux being given as

$$Q^{E_1} = \frac{h^3}{3\eta_0}\left[\sigma\frac{\partial}{\partial r}\left(\frac{1}{r}\frac{\partial}{\partial r}\left(r\frac{\partial h}{\partial r}\right)\right) - \rho g\frac{\partial h}{\partial r} + \rho\Omega^2 r\right], \tag{5.37}$$

and

$$Q^{E_2} = \frac{h^{\alpha+2}}{\eta_0(\alpha+2)\,\tau_{1/2}^{\alpha-1}}\left[\sigma\frac{\partial}{\partial r}\left(\frac{1}{r}\frac{\partial}{\partial r}\left(r\frac{\partial h}{\partial r}\right)\right) - \rho g\frac{\partial h}{\partial r} + \rho\Omega^2 r\right]^{\alpha}. \tag{5.38}$$

Using non-dimensional scales introduced in Section 2.3, we have

$$Q^{E_1} = \frac{h^3}{3}\left[\frac{\rho\Omega^2 LH^2}{\eta_0 U}r - \frac{\rho g H^3}{\eta_0 UL}\frac{\partial h}{\partial r} + \frac{\sigma H^3}{\eta_0 UL^3}\frac{\partial}{\partial r}\left(\frac{1}{r}\frac{\partial}{\partial r}\left(r\frac{\partial h}{\partial r}\right)\right)\right], \tag{5.39}$$

$$Q^{E_2} = \frac{h^{\alpha+2}}{(\alpha+2)\,\tau_{1/2}^{\alpha-1}}\left[\frac{\rho\Omega^2 LH^{\frac{\alpha+1}{\alpha}}}{(\eta_0 U)^{1/\alpha}}r - \frac{\rho g H^{\frac{2\alpha+1}{\alpha}}}{(\eta_0 U)^{1/\alpha}L}\frac{\partial h}{\partial r} + \frac{\sigma H^{\frac{2\alpha+1}{\alpha}}}{(\eta_0 U)^{1/\alpha}L^3}\frac{\partial}{\partial r}\left(\frac{1}{r}\frac{\partial}{\partial r}\left(r\frac{\partial h}{\partial r}\right)\right)\right]^{\alpha}. \tag{5.40}$$

From equations (5.39) and (5.40), there are two possible choices for U,

$$U_1 = \frac{\rho\Omega^2 LH^2}{\eta_0}\,, \qquad \text{and} \qquad U_2 = \frac{\rho^{\alpha}\Omega^{2\alpha}L^{\alpha}H^{\alpha+1}}{\eta_0\tau_{1/2}^{\alpha-1}}\,,$$

which are the characteristic velocities for low and high shear rates respectively. The characteristic velocity, U_1, is the Newtonian velocity scale obtained in Chapter 3 by balancing centrifugal and viscous forces. Since the Ellis viscosity model describes shear-thinning at

moderate to high shear rates, allowing a Newtonian viscosity at low shear rates, we will choose U_2 as the velocity scale.

We non-dimensionalise the viscosity as follows. The viscosity of an Ellis fluid may be written as:

$$\eta = \eta_0 \left(1 + \left| \frac{\tau_{rz}}{\tau_{1/2}} \right|^{\alpha-1} \right)^{-1} . \tag{5.41}$$

From equation (5.9), the shear stress τ_{rz} may be expressed as

$$\tau_{rz} = \bar{\eta} \frac{U}{H} \left(\eta \frac{\partial u}{\partial z} \right) .$$

Non-dimensionalising (5.41), we have

$$\bar{\eta}\eta = \eta_0 \left(\frac{H\tau_{1/2}}{\bar{\eta}U} \right)^{\alpha-1} \left[\beta + \left(\eta \frac{\partial u}{\partial z} \right)^{\alpha-1} \right]^{-1} , \tag{5.42}$$

where

$$\beta = \left(\frac{H\tau_{1/2}}{\bar{\eta}U} \right)^{\alpha-1} . \tag{5.43}$$

This leads to

$$\bar{\eta} = \eta_0^{1/\alpha} \left(\frac{H\tau_{1/2}}{U} \right)^{(\alpha-1)/\alpha} . \tag{5.44}$$

Upon non-dimensionalising and letting $U = U_2$, we have

$$Q^{E_2} = \frac{h^{\alpha+2}}{(\alpha+2)} \left[C \frac{\partial}{\partial r} \left(\frac{1}{r} \frac{\partial}{\partial r} \left(r \frac{\partial h}{\partial r} \right) \right) - B \frac{\partial h}{\partial r} + r \right]^{\alpha} , \tag{5.45}$$

and the Newtonian component of the flux then becomes,

$$Q^{E_1} = \frac{\beta h^3}{3} \left[C \frac{\partial}{\partial r} \left(\frac{1}{r} \frac{\partial}{\partial r} \left(r \frac{\partial h}{\partial r} \right) \right) - B \frac{\partial h}{\partial r} + r \right] , \tag{5.46}$$

where $B = \rho g H^3/\bar{\eta} UL$ and $C = \sigma H^3/\bar{\eta} UL^3$. When $\alpha = 1$, $\beta = 1$ and we have $Q^{E_2} = Q^{E_1}$. In this case, the resulting governing equation is similar to the Newtonian case with $\eta = \eta_0/2$. Note that the velocity scale chosen (U_2) to obtain (5.45) and (5.46) does not really matter as the value of β can be chosen in such a way that in effect, is like taking $U = U_1$.

The Ellis model basically describes shear thinning but unlike the power-law model, at low shear rates we expect Newtonian flow to dominate. Thus we can expect Q^{E_2} to dominate away from the centre and the free surface, but near the centre and the free surface Q^{E_1} should influence the flow more significantly. Therefore, β tells us at what level in the layer $Q^{E_1} \simeq Q^{E_2}$ and where each dominates.

5.3 Numerical scheme and results for power-law fluids

Equation (5.20) derived for power-law fluids is a fourth order differential equation that can not be solved analytically, therefore we now devise a numerical scheme. In general, the governing equations derived for non-Newtonian viscosity models are more complicated than that of the Newtonian model. The main difference in the governing equations between the Newtonian and the power-law model is the power, $1/n$, in the flux of the power-law model. The expression for the flux makes it impossible for us to implement directly a semi-implicit scheme as was carried out for Newtonian fluids in Section 3.6. An alternative method must therefore be employed.

Calculating the flux in the power-law scheme

The governing equation for a rotating power-law thin film is given as

$$\frac{\partial h}{\partial t} + \frac{1}{r}\frac{\partial \left(rQ^P\right)}{\partial r} = 0 \,, \tag{5.47}$$

where the expression for the flux, Q^P, is given by

$$Q^P = \left[\frac{n}{2n+1}\left(C\frac{\partial}{\partial r}\left(\frac{1}{r}\frac{\partial}{\partial r}\left(r\frac{\partial h}{\partial r}\right)\right) - B\frac{\partial h}{\partial r} + r\right)^{1/n}\right] h^{(2n+1)/n} \,. \tag{5.48}$$

We introduce a normalisation of the flux and express equation (5.47) as

$$\frac{\partial h}{\partial t} + \frac{1}{r}\frac{\partial \left(r\frac{Q^N}{Q^N}Q^P\right)}{\partial r} = 0 \,, \tag{5.49}$$

where

$$Q^N = \frac{h^3}{3}\left[C\frac{\partial}{\partial r}\left(\frac{1}{r}\frac{\partial}{\partial r}\left(r\frac{\partial h}{\partial r}\right)\right) - B\frac{\partial h}{\partial r} + r\right] \tag{5.50}$$

is the Newtonian flux. Equation (5.49) can be written as

$$\frac{\partial h}{\partial t} + \frac{1}{r}\frac{\partial \left(rFQ^N\right)}{\partial r} = 0 \,, \tag{5.51}$$

where F is the ratio between the non-Newtonian and Newtonian fluxes, Q^P/Q^N. Equation (5.47) is thus reduced to a more manageable form similar to the Newtonian case (see equation (3.19)). Consequently, the numerical scheme developed in Section 3.6 will be slightly modified to now include F, the ratio of the fluxes. The basic numerical scheme is therefore

given by

$$h_i^{k+1} = h_i^k - \frac{2\Delta t}{r_{i+1/2}^2 - r_{i-1/2}^2}\left(r_{i+1/2}F_{i+1/2}Q_{i+1/2}^N - r_{i-1/2}F_{i-1/2}Q_{i-1/2}^N\right), \quad (5.52)$$

$$h_0^{k+1} = h_0^k - \frac{4\Delta t}{\Delta r}F_{1/2}Q_{1/2}^N. \quad (5.53)$$

The parameter F is defined as

$$F_{i+1/2} = \frac{3n}{2n+1}h_{i+1/2}^{(1-n)/n}\left[\lambda_i - B\frac{h_{i+1}-hi}{\Delta r} + \left(\frac{2h_i}{h_{i+1}+h_i}\right)^{2n+1} r_{i+1/2}\right]^{(1-n)/n}, \quad (5.54)$$

where

$$\lambda_i = \frac{C}{\Delta r^3}\left(\frac{i+3/2}{i+1}h_{i+2} - \frac{3i+1/2}{i}h_{i+1} + \frac{3i+5/2}{i+1}h_i - \frac{i-1/2}{i}h_{i-1}\right),$$

and

$$\left(\frac{2h_i}{h_{i+1}+h_i}\right)^{2n+1}$$

is a correction factor to implement an upwind scheme in the non-Newtonian factor. The expression $F_{i+1/2}$ is calculated explicitly *i.e.* all film heights are evaluated at $t = k\Delta t$, and the ratio is then incorporated in the semi-implicit scheme developed for Newtonian fluids. The overall numerical scheme is therefore, still a semi-implicit scheme. This scheme will now be used to model spinning power-law fluids.

Simulations for the fluid height will be carried out for three values of the power-law index, n. The values of n that will be used are for two non-Newtonian fluids: Hydroxethylcellulose ($n = 0.5088$) and Blood ($n = 0.6$), taken from the table of parameters for viscosity models found in [65], as well as a theoretical $n = 0.8$ to help bridge the gap in the n values for the power-law fluids and the Newtonian fluid the Newtonian fluid ($n = 1$).

Scheme validation

Before carrying out any simulations, we need to be certain the scheme reasonably satisfies the requirements of mass conservation and convergence, as discussed in Section 3.7.1. The change of volume for a wide range of space and time steps was found to be very small, in the range $10^{-5} - 10^{-6}$ %. Convergence is also satisfied and is evidenced in the solution being insensitive to further grid refinement, for example for Δr in the range $3.125\times10^{-5} - 2.5\times10^{-3}$.

A further check comes through comparison with the analytical solution given by equations (5.28) and (5.29). In figure 5.1 we show results obtained via the numerical scheme, with

surface tension and gravity terms set to zero and also the analytical solution. Results are shown for $t = 0, 1, 2.5, 5$ and 10. We have chosen $n = 0.6$ to illustrate the example, although the correspondence was equally close for other values tested.

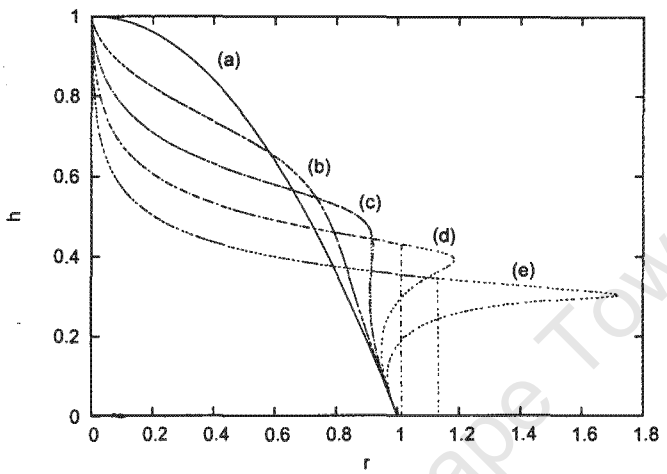

Figure 5.1: Comparison of analytical and numerical solutions, for $n = 0.6$.

For each case $(a) - (e)$, there are two curves corresponding to the numerical and analytical results. The solution (a) and (b) are virtually identical. Curve (c) exhibits a slight difference at the front where the analytical solution becomes double-valued. This is more apparent on curves (d) and (e), where the analytical solution develops the front wave. As discussed in Section 3.7.1, this is obviously unrealistic. However, it is clear that in the bulk of the fluid the two sets of results match.

Our final check on the scheme is to let $n = 1$ and compare with earlier numerical results for Newtonian fluids. Results are shown in figure 5.2 for $B = 0$ and $C = 0$ at times $t = 0, 1, 2.5, 5$ and 10.

Again curves $(a) - (e)$ each show two results. However, in this case the Newtonian and non-Newtonian results are identical for all t. Therefore, the Newtonian model is recovered from the power-law model by letting $n = 1$. At $t = 10$, the film height $h \sim 0.264$ for all r.

With the numerical scheme validated, we now present some results starting with the simplest case, where both gravity and surface tension are neglected, so that the fluid spreads under the influence of centrifugal force only. Afterwards, we will add gravity and then surface tension to the model. We will plot some profiles to show how the free surface of an initial film described by $h(r) = 1 - r^2$ (up to the point where $h = h_p$), of a power-law fluid evolves

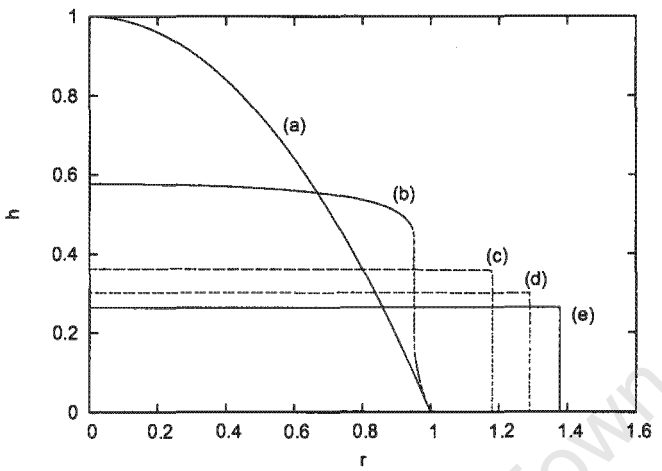

Figure 5.2: Comparison of the evolution of Newtonian and power-law fluid when $n = 1$.

with time. Unless otherwise stated, the curves (a), (b), (d) and (e), represent the predicted film heights at $t = 0, 1, 5$ and 10, respectively. The curve (c) will depict different times, t, for the three values of n to show the development of the capillary ridge. The reason for choosing the different times is that when surface tension is included, the start of the capillary ridge is best illustrated at slightly different times for different n. Therefore, the curve (c) will represent the film profile at $t = 2$ for $n = 0.8$, $t = 2.5$ for $n = 0.6$ and $t = 3$ for $n = 0.5088$.

5.3.1 Results when $B = 0$ and $C = 0$

In this section, we set B and C to zero to simulate the fluid height for power-law fluids when gravity and surface tension are neglected in the model, with $n = 0.8, 0.6$ and 0.5088. The results are presented in the following three figures.

Figure 5.3 shows the predicted film height for a power-law fluid with $n = 0.8$. It can be seen that not only is there a peak in the centre but the final height ($t = 10$) is also greater than that predicted for a Newtonian fluid, with a maximum film height, $h_{\max} \sim 0.59$ and a minimum film height, $h_{\min} \sim 0.29$. We define $h_{\min}$ as the minimum film height of the fluid before the vertical front.

Figures 5.4 and 5.5 give profiles for power-law fluids with $n = 0.6$ and $n = 0.5088$, respectively. The peaks at the centre and the final film heights are predicted to be even higher than those for $n = 0.8$, with $h_{\max} \sim 0.96, 0.99$ and $h_{\min} \sim 0.34, 0.38$, respectively.

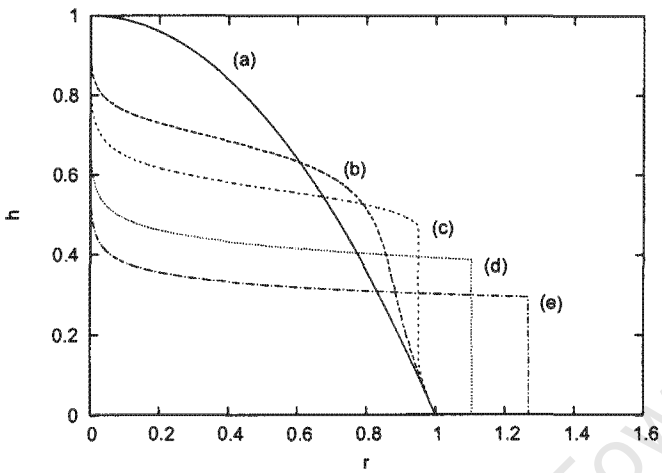

Figure 5.3: Evolution of a power-law fluid, $n = 0.8$, $B = 0$ and $C = 0$.

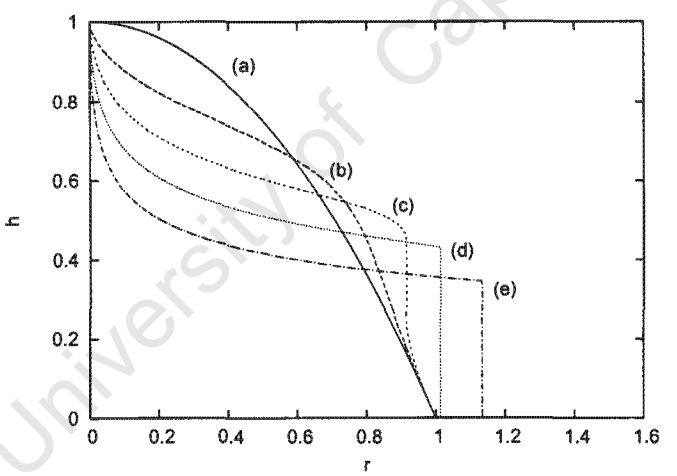

Figure 5.4: Evolution of a power-law fluid, $n = 0.6$, $B = 0$ and $C = 0$.

From figures 5.3 – 5.5 it is evident that unlike the Newtonian model, the power-law predicts films which do not thin uniformly but instead leave peaks at the centre [38]. It is observed that the peaks at the centre tend to be higher with decreasing values of n, *i.e.* as the fluid becomes more "non-Newtonian". This is due to the non-uniform shear experienced by the fluid, which is zero at the centre and increases radially. The zero shear at the centre leads to infinite viscosity, which would theoretically imply no movement there. Clearly, when $n = 0.5088$ (figure 5.5), there is very little change in the film height at the centre. The rate of spreading is also observed to reduce with decreasing values of n. This is because of

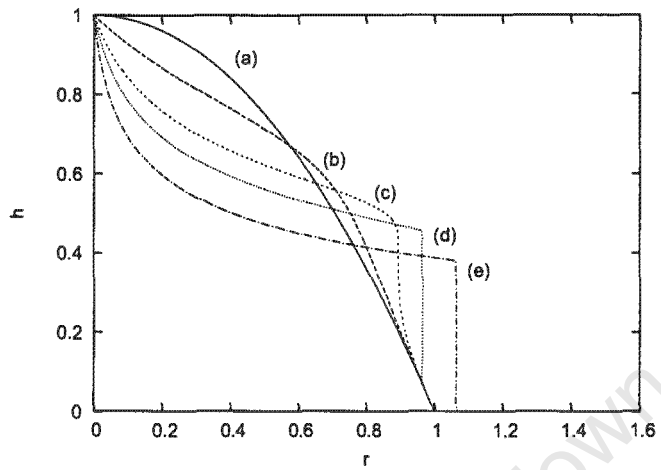

Figure 5.5: Evolution of a power-law fluid, $n = 0.5088$, $B = 0$ and $C = 0$.

a reduction in shear rates which results in an increase in the apparent viscosity, therefore leading to a reduced rate of spreading.

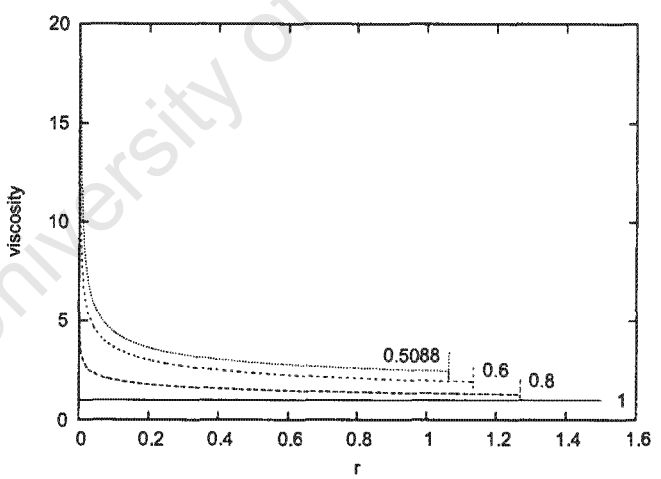

Figure 5.6: Viscosity, η, for various values of n at $z = h_p$ at $t = 10$.

Figure 5.6 shows a plot of the viscosity at height $z = h_p$ for four values of n, including the Newtonian fluid ($n = 1$). The Newtonian viscosity is constant throughout the fluid layer. The power-law viscosity on the other hand, is not constant but increases as r decreases. As a result, the viscosity is highest at the centre. The high viscosity around the centre leads to the peaks illustrated in earlier results (figures 5.3 – 5.5). This effect at the centre has

previously been observed theoretically [38]. Since $\eta \sim u_z^{n-1}$, the profiles reflect the fact that $u_z \to 0$ as $r \to 0$. If we were to examine the profiles at higher values of z we would find η steadily increasing until we reach the free surface, where $u_z = 0$ and η is infinity everywhere.

For $n < 1$, the viscosity decreases at the moving front and then increases as the film height becomes equal to the precursor layer height. In fact, the jump on the right hand side of the curves in figure 5.6 indicates where the precursor film starts. Thus, the increased viscosity in the precursor layer means the precursor layer remains on the substrate without being thrown off by the centrifugal force. The viscosity curves for different n further show that the power-law fluid with $n = 0.5088$ has the highest viscosity throughout the region while the Newtonian fluid has the lowest. Therefore, it appears the viscosity also increases with decreasing values of n. This is what leads to the higher profiles obtained over the whole domain, for lower values of n.

The power-law model does not accurately model the rotating film at the centre when $B, C = 0$, because of the high peaks it predicts at the centre. Therefore, the power-law model is not appropriate for spin coating, but things change with $B, C \neq 0$.

5.3.2 Results when $B \neq 0$ and $C = 0$

We will now include gravity effects in the model, with $B = 0.0248$ (taken from table 3.2).

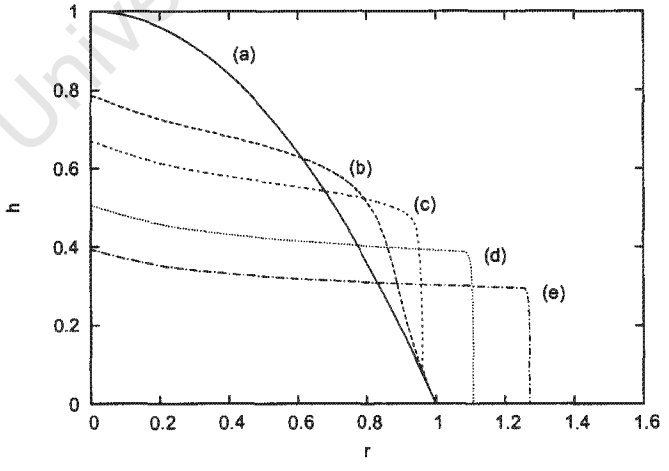

Figure 5.7: Evolution of a power-law fluid, $n = 0.8$, $B = 0.0248$.

Figures 5.7 – 5.9 show the predicted film heights at $t = 0, 1, 2$ (2.5 or 3), 5 and 10, when

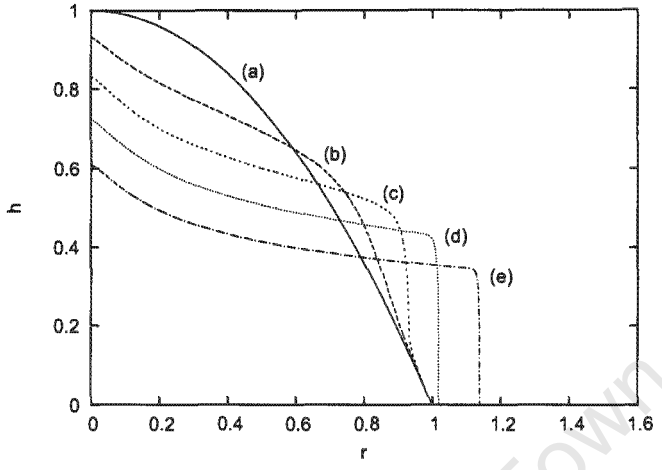

Figure 5.8: Evolution of a power-law fluid, $n = 0.6$, $B = 0.0248$.

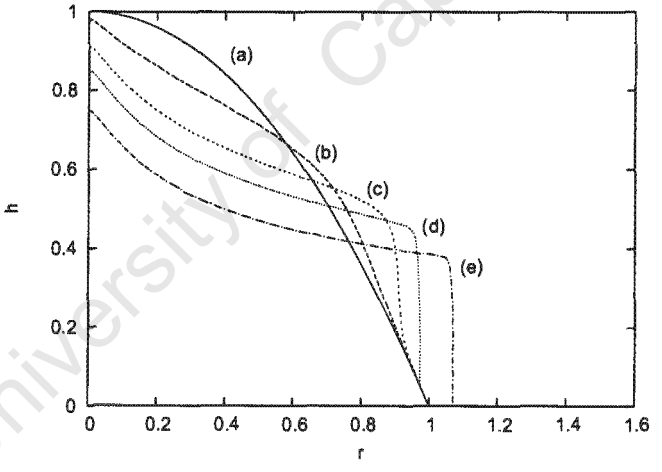

Figure 5.9: Evolution of a power-law fluid, $n = 0.5088$, $B = 0.0248$.

gravity effects are included in the model. It is interesting to note that adding gravity results in peaks that are remarkably reduced. For $n = 0.8, 0.6, 0.5088$, we have $h_{\max} \sim 0.39, 0.61, 0.75$ and $h_{\min} \sim 0.29, 0.31, 0.34$, respectively. The peaks in these results have been reduced by approximately between $25\% - 37\%$ when compared to the peak height predicted when gravity is neglected. However, there is very little reduction away from the centre with the minimum heights being reduced by about $0\% - 10\%$ which is not very significant when compared to the reduction at the centre. The difference in the height reduction at the centre and away from the centre is due to gravity induced diffusion, which affects the film height more where

the film is angular than where it is flat or nearly flat. Therefore, the addition of gravity on a film is more likely to be significant in areas where the film is less flat.

The value of B used in these simulations is relatively small ($B \ll 1$) yet it results in smoother films and peaks at the centre that are significantly reduced than when $B = 0$. Jenekhe & Schuldt [38], in their theoretical investigation of spin coating of power-law fluids, obtain results in which the fluid is stuck at the centre, thereby leaving peaks. However, results obtained using our model show that the introduction of gravity into the model results in greater diffusion, helping to reduce the peaks considerably to produce profiles closer to what is observed experimentally.

5.3.3 Results when $B \neq 0$ and $C \neq 0$

The surface tension comes into the governing equation as a fourth order term, causing addition of capillary forces difficult to deal with numerically. However, we are primarily interested in investigating whether surface tension is worth including in the model. Therefore, in this section, simulations will be carried out for various values of C using the same values of n as in the preceding sections. We also wish to compare the changes that occur as surface tension is included in the model, to what was observed for Newtonian fluids.

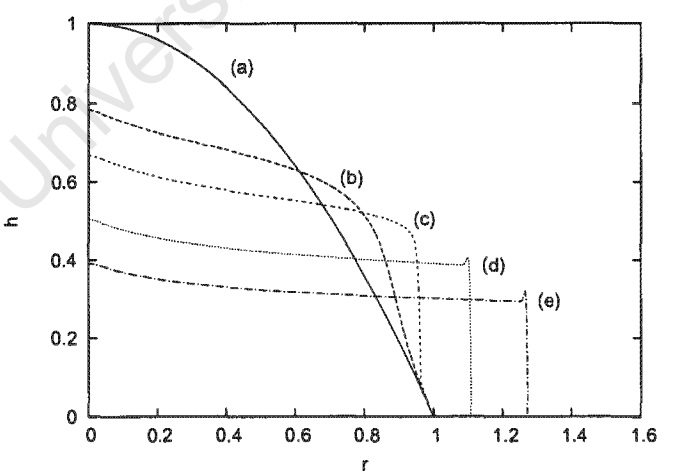

Figure 5.10: Evolution of a power-law fluid, $n = 0.8$, $B = 0.0248$ and $C = 8.8451 \times 10^{-8}$.

Figures 5.10 – 5.12 show the predicted film heights for a power-law fluid with $n = 0.8$, at $t = 0, 1, 2, 5$ and 10, when both gravity and surface tension effects are included in the model.

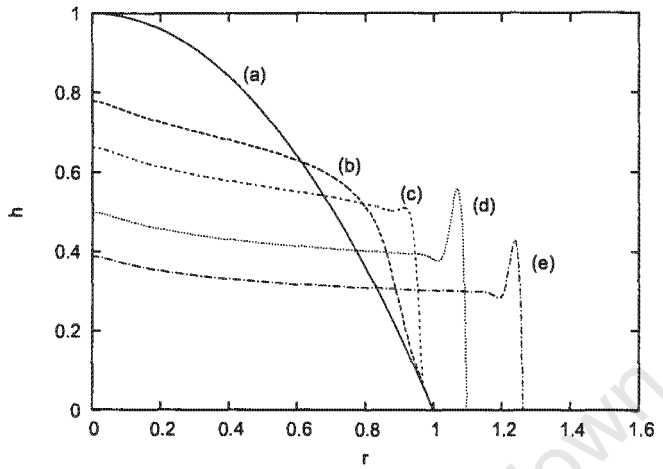

Figure 5.11: Evolution of a power-law fluid, $n = 0.8$, $B = 0.0248$ and $C = 8.8451 \times 10^{-6}$.

The value of C is increased in stages from $C = 8.8451 \times 10^{-8}$, $C = 8.8451 \times 10^{-6}$, and finally $C = 8.8451 \times 10^{-4}$.

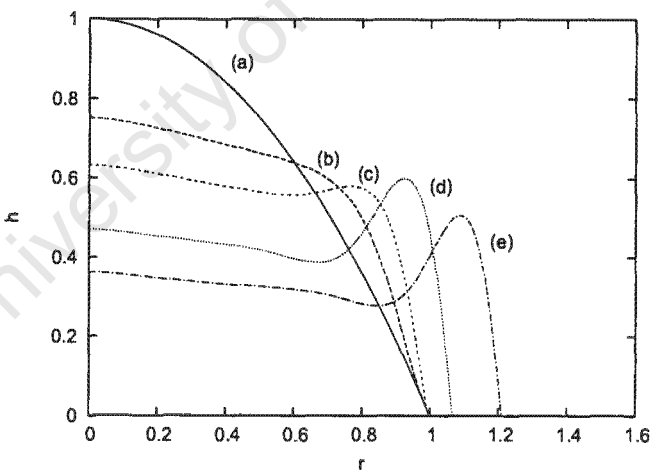

Figure 5.12: Evolution of a power-law fluid, $n = 0.8$, $B = 0.0248$ and $C = 8.8451 \times 10^{-4}$.

Figure 5.10 shows a small capillary ridge at $t = 5$ and $t = 10$. As surface tension is increased, its effect on the resulting profiles becomes evident, as shown in figures 5.11 and 5.12. The increase in surface tension results in a bigger capillary ridge as well as a more flattened centre, reducing the height at the centre. The capillary ridge obtained in these results is not unusual and has been observed in previous studies of Newtonian spin coating [66, 98].

The difference in the final height resulting from an increase in surface tension is more clearly show in figure 5.13, where the curves (1), (2), (3), (4) and (5) represent the final film height ($t = 10$) for five different values of C: $C = 8.8451 \times 10^{-4}$, $C = 8.8451 \times 10^{-5}$, $C = 8.8451 \times 10^{-6}$, $C = 8.8451 \times 10^{-7}$, $C = 8.8451 \times 10^{-8}$, respectively.

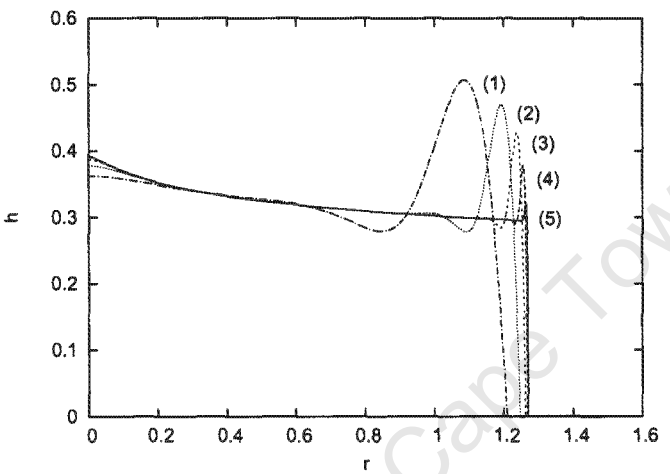

Figure 5.13: Evolution of a power-law fluid, $n = 0.8$ for various values of C.

It is interesting to note that the five curves have the same film height in the mid region. The main difference in the curves is at the front where the capillary gets bigger with increasing C. There is also a slight reduction in the film height at the centre as C is increased. This is because of the high curvature there. At the front, as surface tension is increased the fluid gets pulled back slightly, so that the fluid layer with the highest value of C spreads the least. Therefore, surface tension slightly reduces the rate of spread of the fluid layer. However, the film height away from the centre and ridge is not significantly affected by the addition of surface tension (see figure 5.13).

Figures 5.14−5.16 depict similar results for different values of C, for $n = 0.6$ at $t = 0, 1, 2.5, 5$ and 10. Figure 5.14 shows that for $C = 8.8451 \times 10^{-8}$, the capillary ridge is hardly noticeable at $t = 10$. As C is increased, figures 5.15 and 5.16 show a 'fully' developed capillary ridge at the front for $t = 5$ and 10.

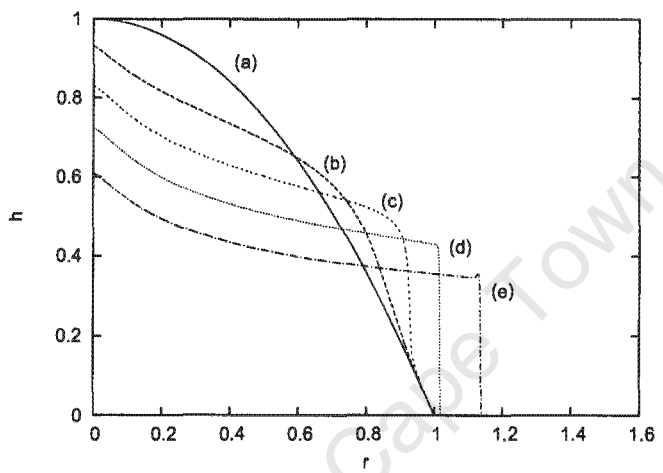

Figure 5.14: Evolution of a power-law fluid, $n = 0.6$, $B = 0.0248$ and $C = 8.8451 \times 10^{-8}$.

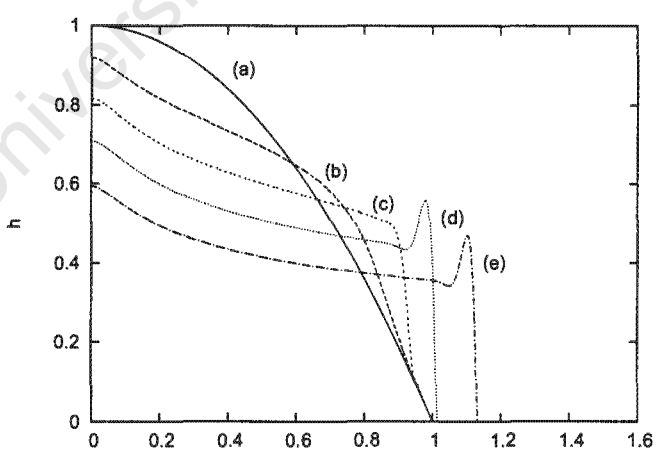

Figure 5.15: Evolution of a power-law fluid, $n = 0.6$, $B = 0.0248$ and $C = 8.8451 \times 10^{-6}$.

The film height at the centre is nearly the same for $C = 8.8451 \times 10^{-8}$ and $C = 8.8451 \times 10^{-6}$. However, there is a slight reduction as C is increased to 8.8451×10^{-4}. The figures therefore,

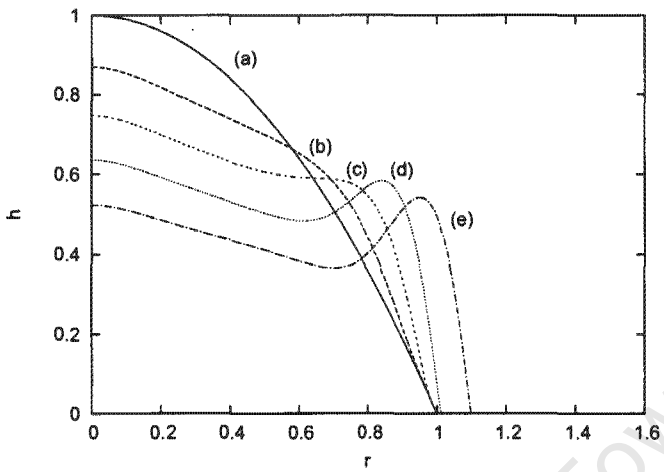

Figure 5.16: Evolution of a power-law fluid, $n = 0.6$, $B = 0.0248$ and $C = 8.8451 \times 10^{-4}$.

show that an increase in surface tension not only results in a reduced rate of spreading when $n = 0.6$, but reduces the film height at the centre as well.

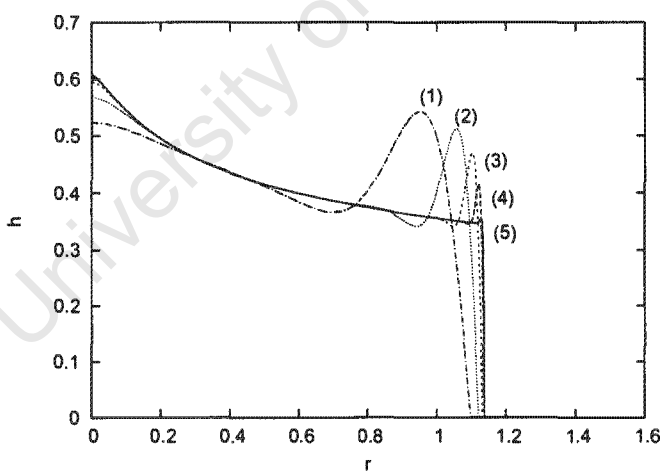

Figure 5.17: Evolution of a power-law fluid, $n = 0.6$ for various values of C.

This is more evident in the results shown in figure 5.17, where again the curves (1), (2), (3), (4) and (5) represent the final film height ($t = 10$) for five different values of C: $C = 8.8451 \times 10^{-4}$, $C = 8.8451 \times 10^{-5}$, $C = 8.8451 \times 10^{-6}$, $C = 8.8451 \times 10^{-7}$, $C = 8.8451 \times 10^{-8}$, respectively.

The curves show a reduced rate of spreading and bigger capillary ridge when C is increased.

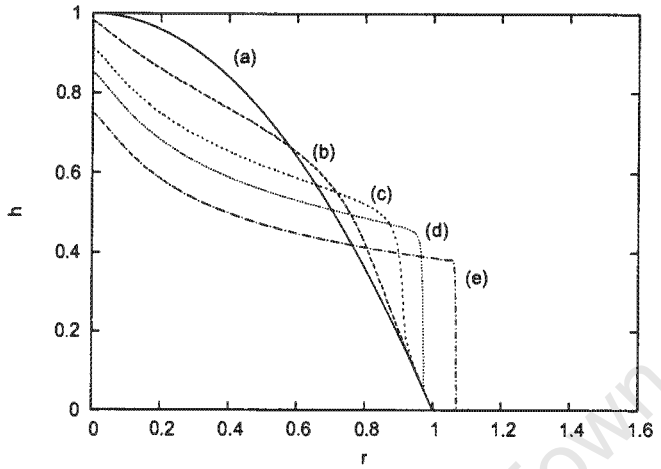

Figure 5.18: Evolution of a power-law fluid, $n = 0.5088$, $B = 0.0248$ and $C = 8.8451 \times 10^{-8}$.

However, the difference in the rate of spreading for the five different values of C is now reduced. This can be attributed to the increased viscosity for this smaller value of n.

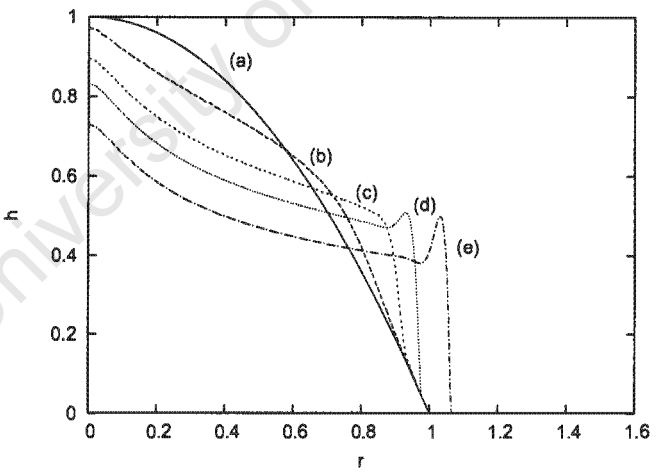

Figure 5.19: Evolution of a power-law fluid, $n = 0.5088$, $B = 0.0248$ and $C = 8.8451 \times 10^{-6}$.

Figures $5.18 - 5.20$ show results generated for $n = 0.5088$ at $t = 0, 1, 3, 5$ and 10, for three different values of C. Similar trends to the previous two values of n are observed. The figures also give evidence of a reduced rate of spreading and larger capillary ridges at the front. At the centre, the fluid height is observed to reduce slightly as well.

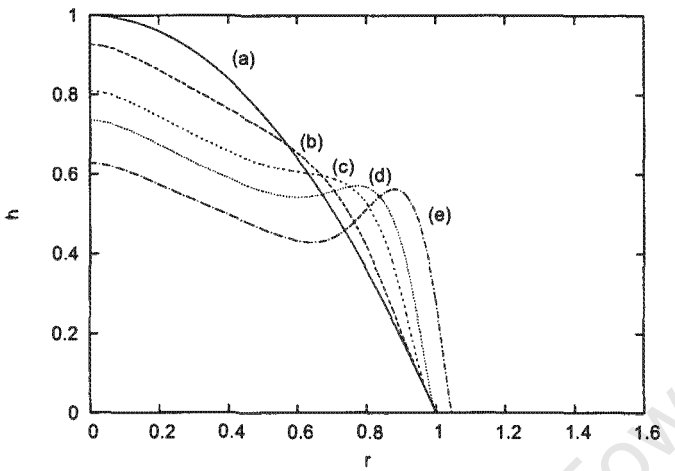

Figure 5.20: Evolution of a power-law fluid, $n = 0.5088$, $B = 0.0248$ and $C = 8.8451 \times 10^{-4}$.

Figure 5.21 shows curves (1), (2), (3), (4) and (5) representing the final film height ($t = 10$) again for five different values of C: $C = 8.8451 \times 10^{-4}$, $C = 8.8451 \times 10^{-5}$, $C = 8.8451 \times 10^{-6}$, $C = 8.8451 \times 10^{-7}$, $C = 8.8451 \times 10^{-8}$, respectively. For this value of n, the rate of spreading for the different curves is even reduced further due to the smaller value of n. As already mentioned, shear rates decrease with decreasing n, which in turn increases the viscosity, reducing the flow rate.

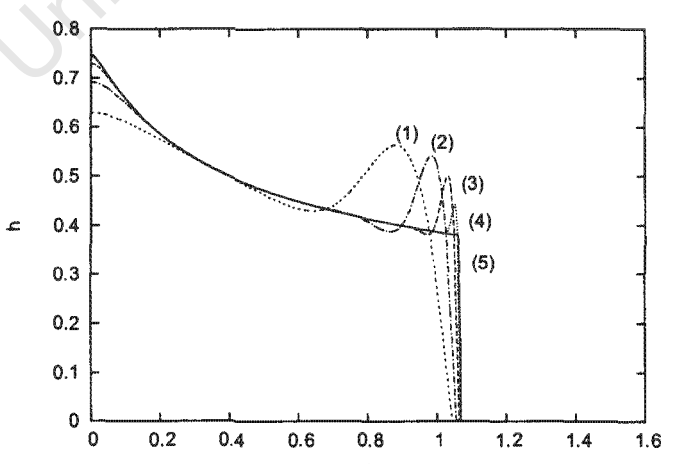

Figure 5.21: Evolution of a power-law fluid, $n = 0.5088$ for various values of C.

We have chosen $n = 0.6$ to illustrate the effect of gravity, when surface tension is kept constant. Nevertheless, the effect of gravity on the film profiles using the other values of n was found to be very similar.

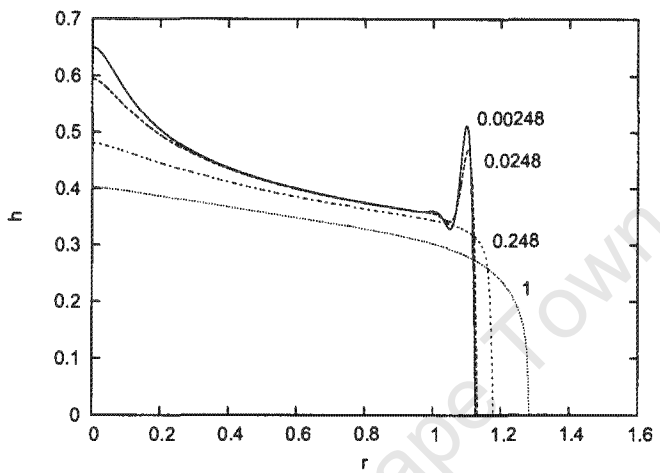

Figure 5.22: Evolution of a power-law fluid, $n = 0.6$, $C = 8.8451 \times 10^{-6}$ and various values of B.

Figure 5.22 shows the film profiles at $t = 10$ for various values of B, while keeping surface tension constant. An increase in gravity results in greater diffusion. This results in reduced film heights at the centre and a smaller capillary ridge. In fact, as gravity is increased further, the capillary ridge disappears completely producing a smooth film profile at the front.

The results in this section show that including surface tension and gravity in the model does make a difference in the resulting profiles. Gravity results in greater diffusion and thereby reduces the film heights and enhances the spreading of the fluid layer. While surface tension does not significantly influence the fluid height in the mid region, it does have an affect on the film profile at the front where the capillary ridge develops. This also shows that shape of the capillary ridge in power-law fluids is still dependent on the interaction between centrifugal force, gravity and capillary forces. Because surface tension tends to hold fluid together, the rate of spreading is slightly reduced as surface tension is increased. Gravity on the other hand, has the opposite effect as it acts to reduce the film and so helps the spreading of the fluid. The high peaks resulting from the use of the power-law model are also significantly reduced by the addition of surface tension and gravity.

Previously power-law models, when employed in modelling spin coating, have predicted peaks

at the centre due to the infinite viscosity there. However, including surface tension helps reduce the fluid height at the centre. Consequently, it can be seen that surface tension leads to more plausible predictions for the power-law model by reducing the effects of increased viscosity at the centre.

In general, the power-law model though, even with inclusion of gravity and surface tension still predicts higher film profiles than those obtained for Newtonian fluids for similar times. This is expected as the low shear rate regions have a high viscosity, thereby reducing the flow rate of the fluid outwards. In addition, the fluid height at the centre is always higher than any other part of the domain, as this is where the shear rate is lowest throughout the film. Therefore, we will now investigate whether the film height becomes more uniform with increasing t.

Longer spinning times

To investigate how power-law fluids thin with increasing t, profiles were generated for longer spinning times ($t = 100$). The curves (a), (b), (c), (d) and (e) in the following 3 graphs represent the profiles for $t = 10, 25, 50, 75$ and 100, respectively. The values for gravity and surface tension are taken as $B = 0.0248$ and $C = 8.8451 \times 10^{-6}$.

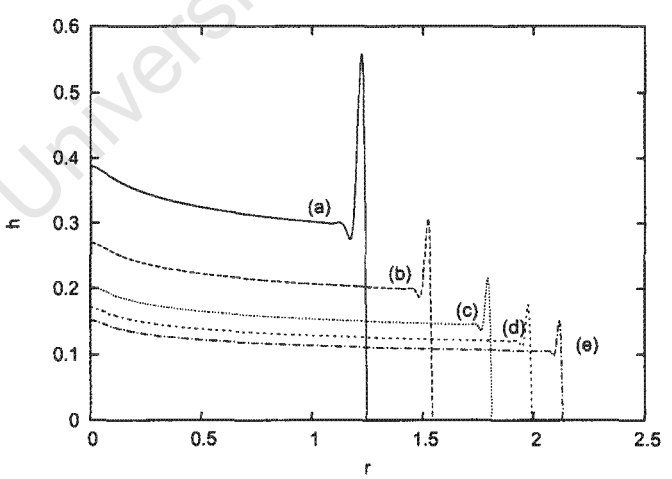

Figure 5.23: Evolution of a power-law fluid, $n = 0.8$, at $t = 10, 25, 50, 75, 100$.

The results shown in figures 5.23 – 5.25 clearly show that even longer spinning times for power-law fluids do not produce uniform films as the film height at the centre remains much

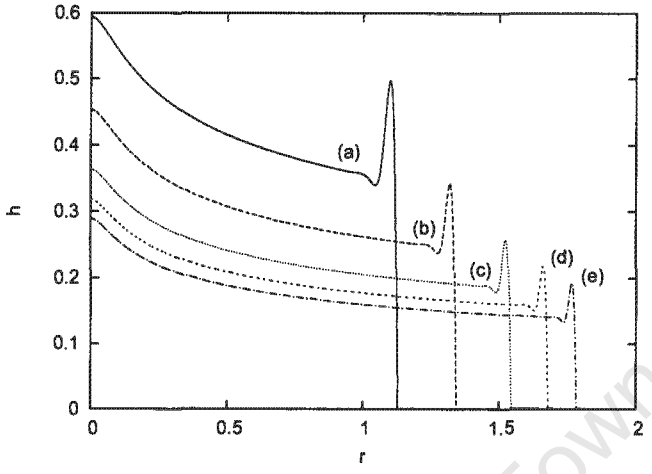

Figure 5.24: Evolution of a power-law fluid, $n = 0.6$, at $t = 10, 25, 50, 75, 100$.

higher than everywhere else in the domain. The film depicting the power-law fluid with $n = 0.5088$ spreads the least and has the highest 'peak'. The power-law fluid with $n = 0.8$ has profiles closest to a uniform profile and spreads furthest.

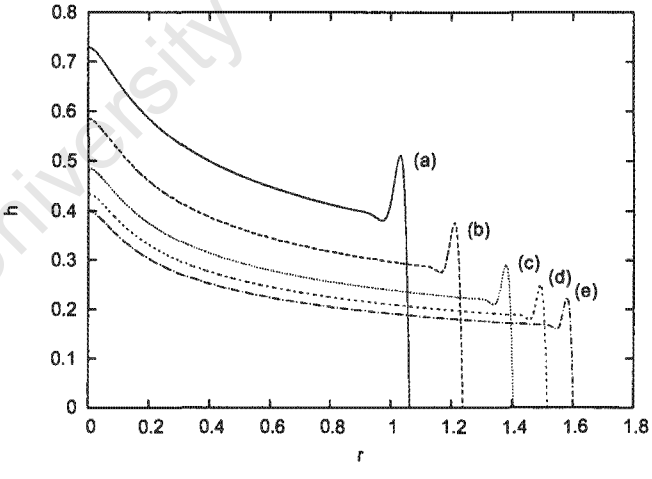

Figure 5.25: Evolution of a power-law fluid, $n = 0.5088$, at $t = 10, 25, 50, 75, 100$.

The developed scheme though, proves to be numerically more demanding for small values of n when surface tension is taken into account. As n becomes smaller, the code struggles and refinement of the space grid becomes very difficult especially when the value of C becomes large. Therefore, this places a lower limit on the space step, Δr, that can be used in the

numerical scheme for small n ($n < 0.5$). However, reducing the time step, Δt, permits further refinement of the space step. Thus, the non-Newtonian scheme with small n is not able to use space steps as small as the ones employed in the Newtonian code and consequently, there is a loss in accuracy. The most obvious disadvantage of using larger space steps, is that some features (the capillary ridge in particular) are lost. This was observed for space steps, $\Delta r > 2 \times 10^{-2}$, for example.

Previous studies on spin coating with power-law fluids have neglected surface tension and gravity and consequently resulted in large spikes at the centre. The inclusion of surface tension and gravity leads to reduced peaks and a capillary ridge at the front. However, as can be clearly seen from the results obtained in this section, the limitations of the power-law model are evident in that the low shear at the centre still leads to film heights that are relatively high there even when surface tension and gravity are included in the model. Therefore, we will now consider the Ellis model.

5.4 Numerical scheme and results for Ellis fluids

The numerical scheme developed for power-law fluids in Section 5.3 can easily be extended to model Ellis fluids. For the Ellis fluids, we have

$$\frac{\partial h}{\partial t} + \frac{1}{r}\frac{\partial \left(rQ^E\right)}{\partial r} = 0 \,, \tag{5.55}$$

where the flux, Q^E, is made up of the two components Q^{E_1} and Q^{E_2} given by equations (5.46) and (5.45), respectively. Using the normalisation introduced in equation (5.49), equation (5.55) can be written as

$$\frac{\partial h}{\partial t} + \frac{1}{r}\frac{\partial \left(r\, GQ^N\right)}{\partial r} = 0 \,, \tag{5.56}$$

where G is the ratio of the fluxes, Q^E/Q^N. The expression for Q^{E_2} is basically like the power-law expression with $1/n$ now replaced by α. So the flux can be calculated in the same way as was carried out for power-law fluids in Section 5.3. The expression Q^{E_1} takes the same format as the Newtonian case of Section 3.6, multiplied by a factor β and can therefore be easily incorporated into the numerical scheme developed for power-law fluids.

The basic numerical scheme to be implemented is then given by:-

$$h_i^{k+1} = h_i^k - \frac{2\Delta t}{r_{i+1/2}^2 - r_{i-1/2}^2}\left(r_{i+1/2}\, G_{i+1/2} Q_{i+1/2}^N - r_{i-1/2}\, G_{i-1/2} Q_{i-1/2}^N\right) \,, \tag{5.57}$$

$$h_0^{k+1} = h_0^k - \frac{4\Delta t}{\Delta r} G_{1/2} Q_{1/2}^N \,, \tag{5.58}$$

which is clearly an extension of the power-law scheme. The ratio of the fluxes, G, can further be simplified as

$$G = \beta + \frac{Q^{E_2}}{Q^N} .$$

The ratio Q^{E_2}/Q^N in the expression for G is calculated in the same way as F in the power-law scheme (5.54).

Values for β

In the previous section, we used n from two fluids (hydroxyethylcellulose and blood). Therefore, we will do corresponding graphs to the power-law section. According to parameters for the Ellis model taken from table 1 of Myers [65], the 2 fluids have the Ellis parameter, α, equal to 2.073 and 3.4, respectively.

From equation (5.43), the value of β can be written as $\beta = (\tau_{1/2}/(\rho\Omega^2 LH))^{\alpha-1}$. Therefore, β is dependent on the angular velocity and film thickness, among other parameters. We will use scales introduced in Section 3.7.2 to provide estimates for values of β. For example, using hydroxyethylcellulose which has $\alpha = 2.073$, we have $\beta = 1.5441$ when $\Omega = 5.235$, $\beta = 0.3489$ when $\Omega = 10.47$ and $\beta = 0.0788$ when $\Omega = 20.94$. The value of ρ is taken as 1000kg/m^3. Previously, simulations were carried out using an angular velocity scale of $\Omega = 5.235$ and $\Omega = 10.47$. Therefore, a value of β in the range $0 < \beta < 1.5$ is well within the velocity scale used in previous simulations.

In the following two figures, we try and establish the effects of β on the film height at $t = 10$. We let $B = 0$ and $C = 0$. Figures 5.26 and 5.27 show profiles simulated at $t = 10$ for various values of β, for $\alpha = 3.4$ and $\alpha = 2.073$, respectively. For very small values of β, the curves are similar to power-law results with the height at the centre now reduced. Figure 5.26 shows solutions for the film height for $0 < \beta < 2$, which are flat near the centre and slanting towards the moving front. Figure 5.27 on the other hand, shows curves for the same values of β that are not necessarily flat at the centre (especially for $\beta < 1$), but significantly reduced when compared to the power-law solutions. It is interesting though, to note that the height at the centre is the same for the two non-Newtonian fluids. The predicted profiles, generally, for $\beta \geq 1$ show that the resulting film heights are similar to the Newtonian case with uniform (or nearly uniform) films. The only difference is in the actual film height attained for each case, which decreases with increasing values of β.

Note that even though the same values of β are used, the fluid with $\alpha = 2.073$ shows more non-Newtonian features in that the centre is not as 'flat' as in the previous case. This is

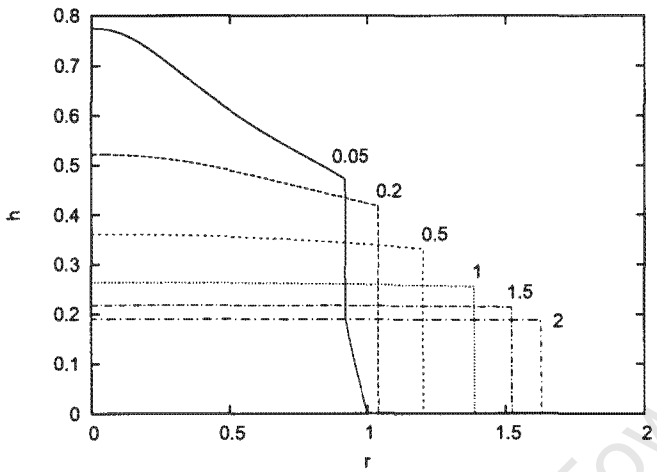

Figure 5.26: Film height at $t = 10$ for various values of β, $\alpha = 3.4$.

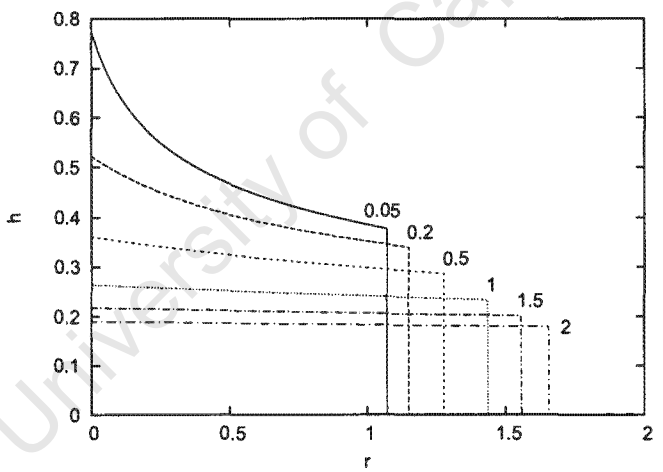

Figure 5.27: Film height at $t = 10$ for various values of β, $\alpha = 2.073$.

probably due to the influence of the Newtonian component of the flux being greater for $\alpha = 3.4$ as a result of the $h^{\alpha+2}$ term in the expression.

It has therefore been established that for $\beta \geq 1$, the resulting films are more Newtonian in character and expected to be uniform. Therefore, in the following simulations we will use two values, one such that $0 < \beta < 1$ (0.5) and the other value such that $\beta > 1$ (1.2), to demonstrate how the Ellis model compares with the Newtonian and power-law models. As β increases, we can expect a transition of the thinning process from power-law ($n < 1$) to

Newtonian ($n = 1$). However, it should be noted though that the transition from power-law to Newtonian is ill-defined [49]. For any $n < 1$, at the free surface the shear, $u_z = 0$, implies infinite viscosity which decreases as $z \to 0$ but when $n = 1$, continuous viscosity implies a switch from infinite to non-infinite viscosity.

To be able to compare the results from the Ellis model with the power-law model results, we will show the evolution of the film at three time intervals as was done in the previous section with curves (a), (b), (c), (d) and (e) representing $t = 0, 1, 2.5, 5$ and 10, respectively.

5.4.1 Results when $B = 0$ and $C = 0$

We will first present the results for an Ellis fluid with $\alpha = 1$, which implies $\beta = 1$. In this instance $Q^{E_2} = Q^{E_1}$.

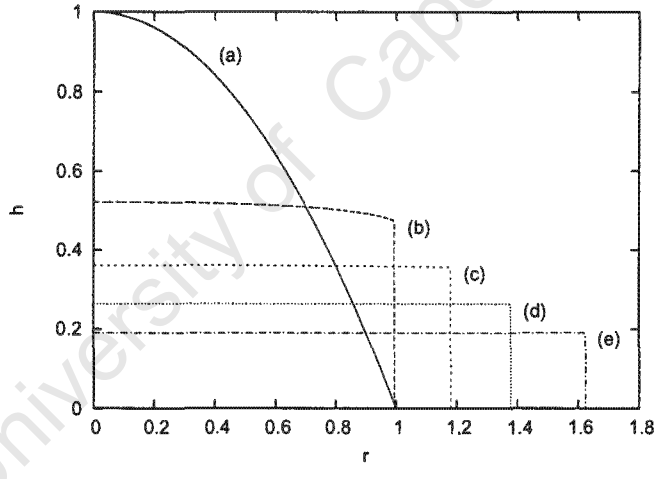

Figure 5.28: Evolution of Ellis fluid, $\alpha = 1$, $\beta = 1$, $B = 0$ and $C = 0$.

Figure 5.28 shows results for the case $\alpha = 1$ to be very similar to the Newtonian case, except the viscosity is now $\eta = \eta_0/2$. Consequently, the fluid thins much faster and further than the Newtonian fluid (figure 5.2). At $t = 10$, the film height is $h \sim 0.19$ for all r.

Figure 5.29 shows the evolution of the film height obtained for $\alpha = 3.4$ and $\beta = 0.5$. This result corresponds to the power-law fluid result in figure 5.4. However, in this Ellis result the film profiles obtained show film heights that thin without leaving high peaks at the centre. The final height at the centre for $t = 10$ is approximately 0.36 units.

The obvious difference that is observed between the power-law and Ellis models is the absence

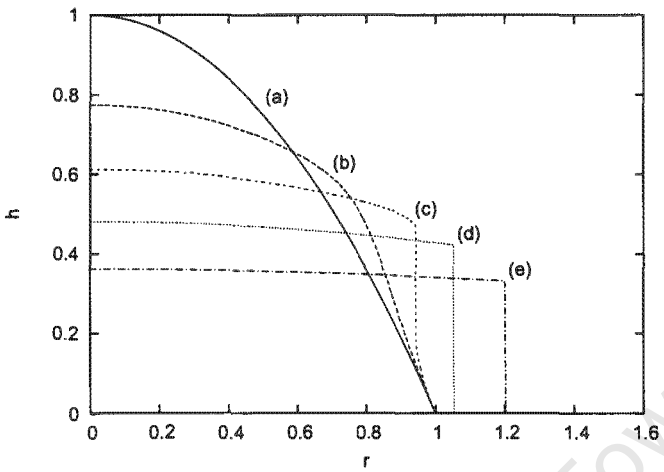

Figure 5.29: Evolution of Ellis fluid, $\alpha = 3.4$, $\beta = 0.5$, $B = 0$ and $C = 0$.

of high 'peaks' at the centre in the latter. This is because the Ellis model allows Newtonian behaviour at low shear rates with a transition to power-law shear-thinning at moderate rates. Therefore, as shear rates become smaller, the Newtonian component will dominate the flow, resulting in a more flattened central region.

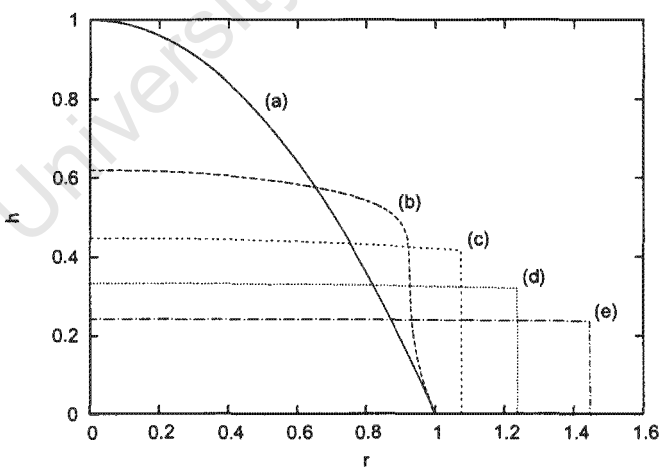

Figure 5.30: Evolution of Ellis fluid, $\alpha = 3.4$, $\beta = 1.2$, $B = 0$ and $C = 0$.

Figure 5.30 shows the effect of increasing β, keeping α constant. The results show that increasing β helps the film profiles thin faster and consequently spread further. The final film height is nearly uniform, with h slightly varying ($0.235 \leq h \leq 0.242$). Therefore,

for $\beta = 1.2$, the final film height obtained is slightly lower than that for a Newtonian fluid ($\simeq 0.264$). This is not unusual as experiments on spin coating of polymer resists [27], indicate non-Newtonian fluids produce thinner films than Newtonian fluids.

Figures 5.31 and 5.32 show results obtained when $\alpha = 2.073$ for $\beta = 0.5$ and $\beta = 1.2$, respectively. The value $\alpha = 2.073$ corresponds to the power-law fluid with $n = 0.5088$. In fact, when β is set to zero, the result obtained is very similar to the power-law result with $n = 0.5088$. Comparing the Ellis and power-law results shows a significant reduction in the peak at the centre (see figure 5.5). The final film height, h, is in the interval ($0.287 \leq h \leq 0.361$) for $\beta = 0.5$ and ($0.219 \leq h \leq 0.242$) for $\beta = 1.2$.

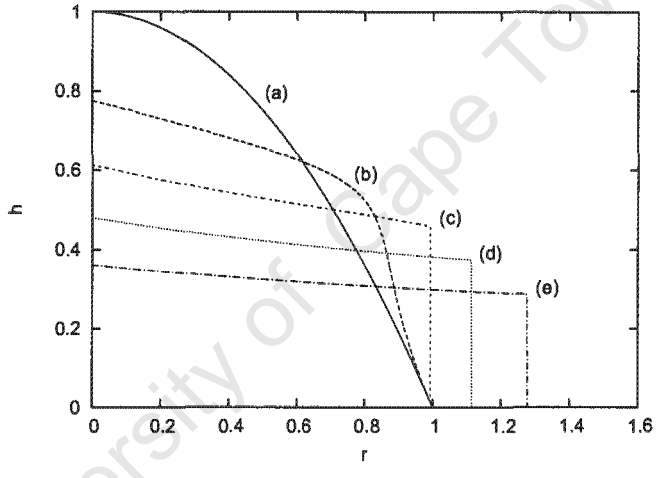

Figure 5.31: Evolution of Ellis fluid, $\alpha = 2.073$, $\beta = 0.5$, $B = 0$ and $C = 0$.

Figures 5.31 and 5.32 differ slightly with the results obtained using $\alpha = 3.4$. These profiles show film heights that continuously decrease radially. Away from the axis, the decrease in the film height (easily noticeable for small values of β) is characteristic of power-law fluids. The reason for this decrease in the height away from the axis is the non-uniform shear rate, which increases radially. Since we are dealing with shear-thinning fluids, the viscosity will decrease with increasing shear rate. This causes the fluid away from the axis to flow more readily than near the axis, where the shear rate is smaller.

Nevertheless, the profiles generated by the Ellis model show great improvement when compared to the power-law results in the previous section. Experimental investigations of non-Newtonian spin coating show no evidence of unusually high peaks at the centre [27].

Comparing the two figures shows clearly the effect on the profiles of increasing β, namely

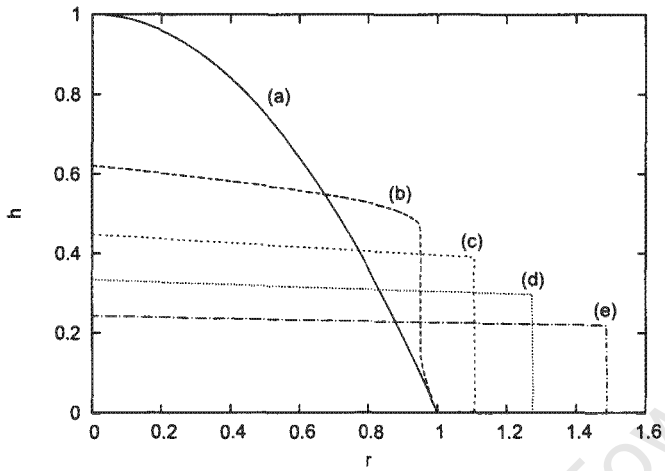

Figure 5.32: Evolution of Ellis fluid, $\alpha = 2.073$, $\beta = 1.2$, $B = 0$ and $C = 0$.

that the fluid spreads further resulting in thinner film heights. In addition, the film is far more inclined with small values of β, indicating that the non-Newtonian effects are dominant. When $\beta > 1$, the films predicted by the Ellis model are thinner than Newtonian films for the same time. This result is in agreement with what has been observed experimentally. According to experiments on spin coating of polymer resists [27], approximation of the fluid (non-Newtonian) by a Newtonian constitutive equation leads to inaccurate predictions as the Newtonian model predicts too thick a film. If this be the case, then it would be logical to assume the values of β would generally be greater than 1, in which case the Ellis model would predict films that are uniform but thinner than the Newtonian model.

5.4.2 Results when $B \neq 0$ and $C \neq 0$

In this section, in line with previous models, we will investigate the effect of including surface tension and gravity to the Ellis model. For gravity effects, we will use $B = 0.0248$ throughout the remaining simulations for the fluid height. Initially, $C = 8.8451 \times 10^{-6}$ will be used to simulate surface tension effects. The same values of β, as in the previous section, will be used so that we can compare with previous results (figures $5.29 - 5.32$).

Figure 5.33 shows the predicted profile when $\alpha = 3.4$, $\beta = 0.5$ at $t = 0, 1, 2.5, 5$ and 10. With surface tension and gravity included in the model, the capillary ridge becomes evident in the profiles as t increases. The height at centre for $t = 10$ (~ 0.36 units) is not affected

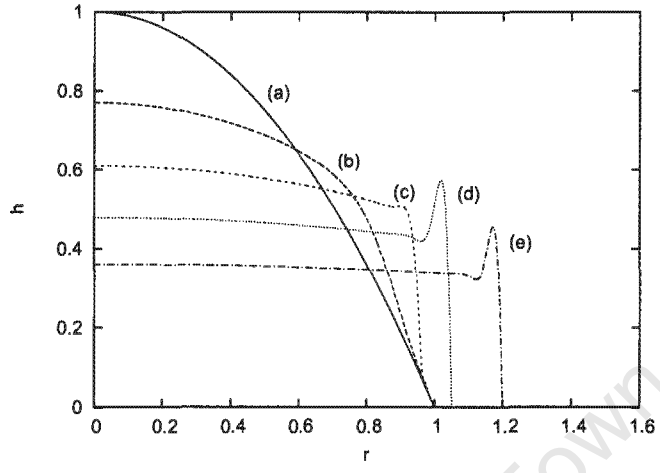

Figure 5.33: Evolution of Ellis fluid, $\alpha = 3.4$, $\beta = 0.5$, $B = 0.0248$ and $C = 8.8451 \times 10^{-6}$.

by the addition of surface tension and gravity. However, at the moving front the capillary ridge results in a slight reduction in the rate of spreading of the fluid.

Figure 5.34 shows results when β is increased to 1.2. Using a larger value of β evidently makes the predicted profiles to be flatter and nearly uniform. For this value of β, the final film height is approximately 0.24 and slightly lower than the Newtonian fluid with the same values of B and C (figure 3.10). On the other hand, comparing figures 5.33 and 5.34 to the power-law equivalent (figure 5.15) shows the superiority of the Ellis model to the power-

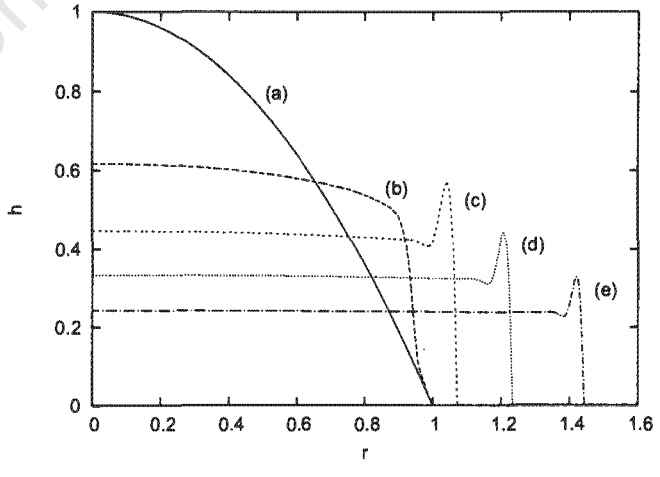

Figure 5.34: Evolution of Ellis fluid, $\alpha = 3.4$, $\beta = 1.2$, $B = 0.0248$ and $C = 8.8451 \times 10^{-6}$.

law, in that the Ellis model does not leave very high film heights at the centre. The Ellis model therefore, provides more realistic results, which are closer to what has been observed experimentally [27].

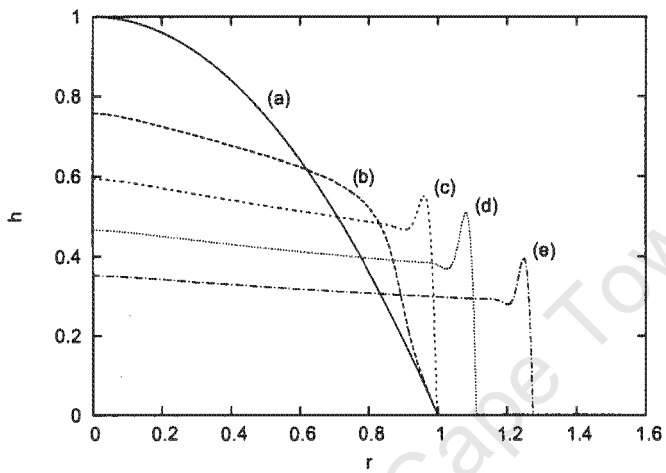

Figure 5.35: Evolution of Ellis fluid, $\alpha = 2.073$, $\beta = 0.5$, $B = 0.0248$ and $C = 8.8451 \times 10^{-6}$.

Figures 5.35 and 5.36 show results for the non-Newtonian fluid with $\beta = 0.5$ and $\beta = 1.2$ (Ellis parameter, $\alpha = 2.073$). The final film height at the centre for both figures is not affected by adding surface tension and gravity to the model. Comparing these two figures with the corresponding power-law result (figure 5.19) shows a remarkable decrease in the peaks at the centre.

The profiles predicted for $\beta = 1.2$ show the capillary ridge developing earlier than when $\beta = 0.5$ (compare 5.35 & 5.35). The reason for this is that for $\beta > 1$, the Newtonian component is expected to dominate the flow. As shear rates decrease, a Newtonian fluid will have lower viscosity than a power-law shear-thinning fluid (whose viscosity increases as shear rates decrease) causing flow to occur more easily. This promotes the outward flow of the fluid, causing the capillary ridge to develop earlier in time. This further demonstrates the fact that larger values of β will increase the rate of spreading in the Ellis model.

In order to show more clearly the effect of increasing surface tension on the profiles, figures $5.37 - 5.40$ compare the profiles for five different values of C, for the same time ($t = 10$).

The curves (1), (2), (3), (4) and (5) represent $C = 8.8451 \times 10^{-4}$, $C = 8.8451 \times 10^{-5}$, $C = 8.8451 \times 10^{-6}$, $C = 8.8451 \times 10^{-7}$ and $C = 8.8451 \times 10^{-8}$, respectively.

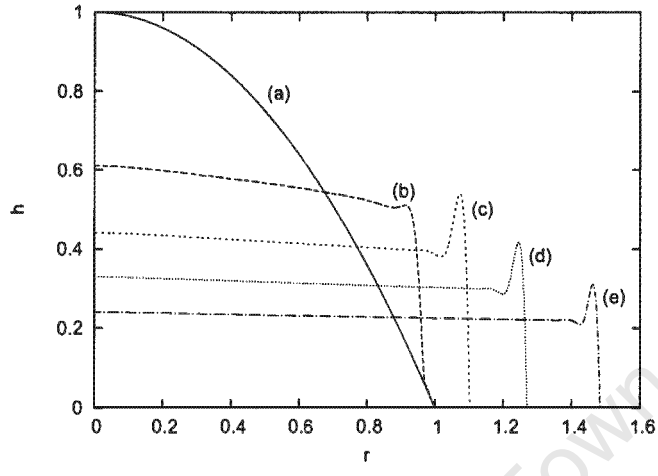

Figure 5.36: Evolution of Ellis fluid, $\alpha = 2.073$, $\beta = 1.2$, $B = 0.0248$ and $C = 8.8451 \times 10^{-6}$.

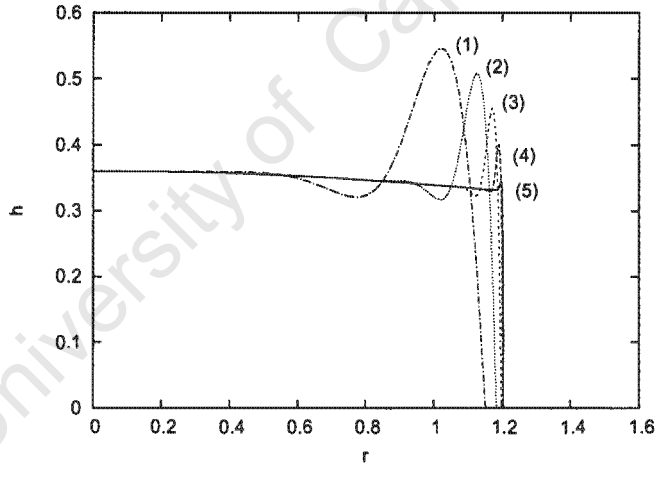

Figure 5.37: Evolution of Ellis fluid, $\alpha = 3.4$, $\beta = 0.5$, $B = 0.0248$ & various values of C.

The results in figures $5.37 - 5.40$ show that an increase in surface tension, as with earlier results, brings about the formation of a larger capillary ridge and reduces the rate of spreading. For smaller values of β (and α) a slight reduction in the film height at the centre may be observed, for large C (figure 5.39). However, in reality the surface tension term would be expected to be lower than $C = 8.8451 \times 10^{-4}$. Therefore, there is not much evidence to suggest that surface tension affects the film height in the central region for the Ellis fluid.

Comparing these figures with earlier results shows that surface tension does affect the profile

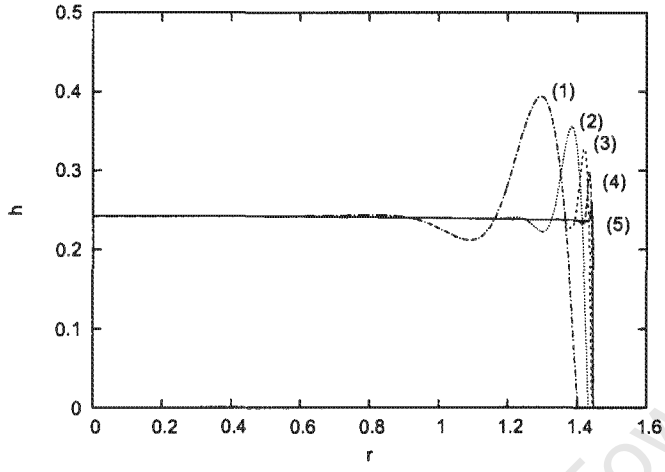

Figure 5.38: Evolution of Ellis fluid, $\alpha = 3.4$, $\beta = 1.2$, $B = 0.0248$ & various values of C.

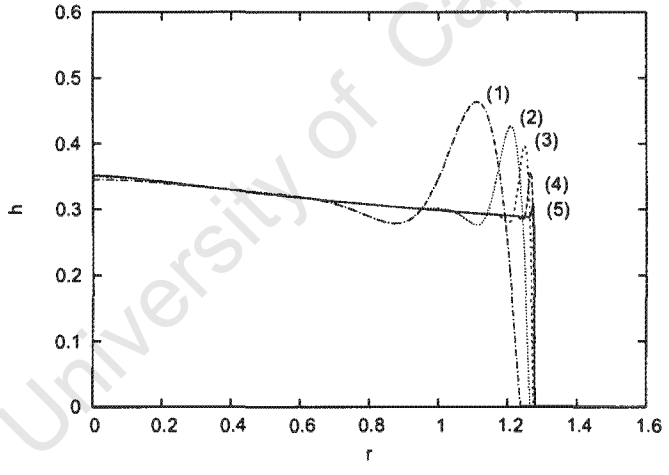

Figure 5.39: Evolution of Ellis fluid, $\alpha = 2.073$, $\beta = 0.5$, $B = 0.0248$ & various values of C.

of the film. An increase in surface tension leads to a larger capillary ridge and a slightly reduced rate of spreading.

From the foregoing results, it has been shown that larger values of both α and β help flatten and reduce the film profiles. The results further show that using larger values of β (1.2) leads to results that are nearly uniform in character, except at moving front where a capillary ridge is present. As earlier demonstrated, using $\beta > 1$, not only leads to uniform films, but film profiles that are even thinner than the Newtonian films.

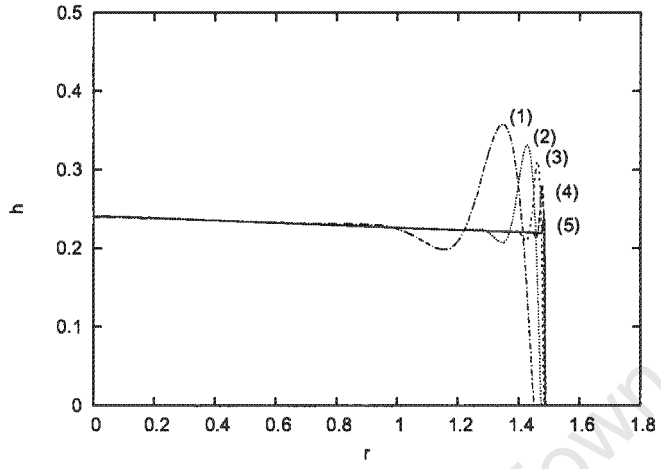

Figure 5.40: Evolution of Ellis fluid, $\alpha = 2.073$, $\beta = 1.2$, $B = 0.0248$ & various values of C.

Longer spinning times

We now compare the Ellis model with the power-law model for longer spinning times. Figures 5.41 and 5.42 show the predicted profiles obtained from the Ellis model for $\alpha = 3.4$ and $\alpha = 2.073$, respectively. The fluid height is simulated for a final time of $t = 100$ and $\beta = 0.5$. The curves (a), (b), (c), (d) and (e) represent the profiles for $t = 10, 25, 50, 75$ and 100, respectively.

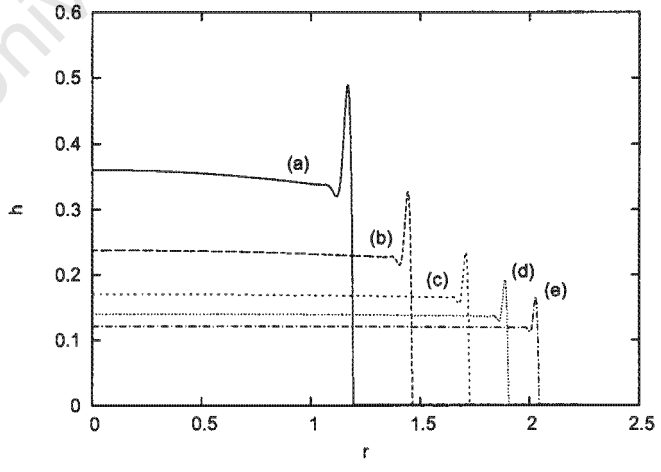

Figure 5.41: Evolution of Ellis fluid, $\alpha = 3.4$, $\beta = 0.5$, at $t = 10, 25, 50, 75, 100$.

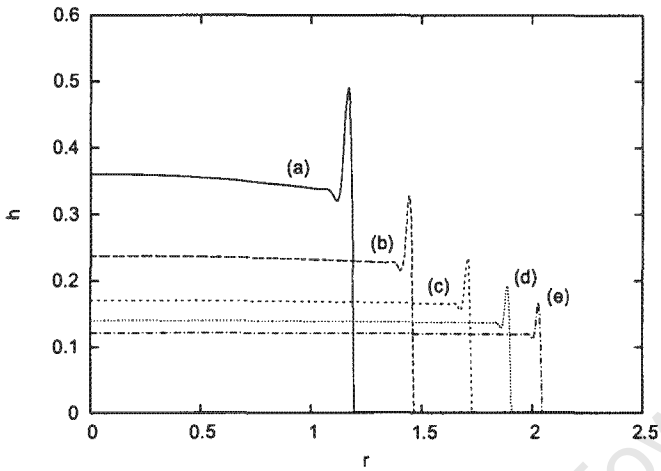

Figure 5.42: Evolution of Ellis fluid, $\alpha = 2.073$, $\beta = 0.5$, at $t = 10, 25, 50, 75, 100$.

From the results, it can be seen that even for a low value of β, the Ellis model provides more realistic results for longer spinning times than the power-law. In fact, the advantage of using the Ellis model over the power-law seems to improve with increasing t as the film profiles obtained for $t = 100$ are almost uniform, when compared to those for shorter times. Therefore, the results obtained for $t = 100$ suggest that profiles modelled using the Ellis viscosity model will become uniform for longer spinning times.

From the results that have been considered in this section, the Ellis model does prove to be a more realistic model than the power-law, since it reduces to the Newtonian model at low shear rates, thereby predicting profiles that are closer to what is observed in experiments. Depending on what values of β are used, the Ellis model can be made to predict profiles that are similar to the Newtonian thin films in every way.

5.5 Conclusion

In this chapter, we have derived equations governing the flow of a thin axisymmetric non-Newtonian fluid layer under the influence of surface tension and gravity. Mathematical models for spin coating have been developed using the power-law and Ellis viscosity models.

A numerical scheme was developed to solve the derived governing equations. The scheme is an extension of the numerical scheme implemented in Chapter 3. Since a direct implementation of the semi-implicit scheme was not possible, because of the expression for the

flux, an alternative method was introduced to circumvent this problem. A normalisation of the flux was therefore introduced. This resulted in an innovative numerical scheme for modelling non-Newtonian flow on a rotating disk, that was simple to apply as an extension of the Newtonian scheme..

Simulations were performed using similar scales to those used in the Newtonian model. For the power-law model, the numerical results obtained when surface tension and gravity are neglected show thinning profiles that leave peaks at the centre, with the smallest value of n giving the highest peak. Theoretically, this is to be expected for the power-law model as the zero shear at the centre leads to infinite viscosity. The results also showed that the rate of spreading reduces with decreasing values of n, and the film heights are correspondingly greater. The numerical results revealed that the addition of gravity to the power-law model brings down the peaks at the centre significantly and in general tends to smooth the film. Consequently, the inclusion of gravity slightly increases the spread of the fluid. However, its influence on very thin films is found to be minimal. When surface tension is included in the power-law model, the effect of the capillary force was observed primarily at the moving front, where a capillary ridge forms, and at the centre where the peaks were significantly reduced.

The numerical results of the Ellis model on the other hand, provided more realistic film profiles in the sense that the central peak was not observed. The model includes a parameter, $\beta > 0$, that characterizes the onset of Newtonian behaviour. For larger values of this parameter ($\beta \geq 1$), the Ellis model predicted profiles that were similar to the Newtonian films but thinner. This is in agreement with spin coating experiments of polymer resists. However, even for smaller values of β, the Ellis model predicted films that did not have peaks at the centre, thereby giving more realistic results than the power-law model. And, as was observed in the other models, the introduction of surface tension results in a capillary ridge at the moving front.

Therefore, we have successfully included surface tension effects in non-Newtonian models, by developing an innovative numerical scheme that was used to solve the governing equations.

Chapter 6

Conclusions and further work

In this thesis, we have investigated spin coating of both Newtonian and non-Newtonian fluids. The main objective was to develop mathematical models of the spin coating process that take into account surface tension and gravity and to investigate what effect, if any, these have on the predicted profile and film height. The role of the Coriolis force on the evolution of a thin film of Newtonian fluid on a rotating disk was also investigated.

In Chapter 3, the standard equation modelling the flow of a thin axisymmetric Newtonian fluid layer on a rotating disk under the influence of surface tension and gravity was derived.

Neglect of surface tension and gravity from this equation, led to a reduced form (the Emslie-Bonner-Peck model). We explored under what conditions formation of vertical fronts was likely to occur. Neglect of surface tension in this reduced form contributes to formation of waves for certain initial film profiles. This provided further motivation for including surface tension in the spin coating models.

A stability analysis was also carried out to study the evolution of waves when surface tension and gravity are included in the model. The analysis revealed that spin coating is a stable method with regard to linear disturbances, for an initially constant film, and surface tension and gravity contribute to this stability.

A numerical scheme was developed to solve the governing equation, using a semi-implicit scheme that was obtained by integrating the flux over a cell. Earlier studies of spin coating show that shocks are likely to develop at the moving front. To avoid this, the flux was discretised using a simple upwind scheme to capture the shock. Before the scheme could be used for the main simulations of the fluid height, it was validated. To do this, a number

of tests were carried out to ensure accuracy. This included ensuring conservation of mass, convergence of the solution, as well as comparing the results with the analytical solution of the Emslie-Bonner-Peck model. Upon satisfying the preceding conditions, the numerical scheme was then used to simulate the height of the fluid on a rotating disk. The simulations were carried out using different magnitudes of surface tension and gravity effects to help us understand how they are likely to affect the final profile of the film.

The simulations for Newtonian fluids predicted film profiles that agreed qualitatively with what has been previously observed in experiments. The films quickly became uniform upon spinning, and the characteristic capillary ridge developed at the moving front. The simulations showed that the shape of this ridge is determined by the competition between centrifugal force, surface tension and gravity. The results further revealed that surface tension tended to hold the fluid together, and therefore reduced the rate of spreading. Gravity on the the other hand, acted to reduce the film height and therefore helped spread the fluid. However, its influence on very thin films was found to be minimal.

In Chapter 4, the governing equations for a rotating thin film, were modified to investigate the role of the Coriolis force on this type of flow. The motivation for this investigation was a previous study in the literature, by Leshev and Peev [52]. According to their findings, existing analytical results which have centrifugal force as the only driving force, predicted film heights near the centre of the disk which were slightly lower than experimental values. They concluded that the Coriolis force should be included in the radial velocity equation. However, a closer look at their work revealed that the analysis leading up to this conclusion was flawed. The model was not correctly solved and the agreement between the analytical and experimental results was as a result of assuming a power-law relation and fitting this to experimental data.

In this thesis, we systematically showed that the Coriolis force was negligible at leading order. Therefore, the main conclusion of this analysis was that the Coriolis force did not affect the leading order relation between the flux and film height obtained via lubrication theory. However, together with inertia the Coriolis force may enter as a correction term to the classical solution.

In Chapter 5, the numerical scheme developed for the Newtonian spin coating model was extended to non-Newtonian fluids. This was carried out using two constitutive models, namely the power-law and Ellis models. The power-law was considered (bearing in mind its limitations) because of its simplicity, the availability of previous results and also as a

starting point in the analysis. The power-law and Ellis model equations both contained an expression for the flux that made it very difficult to implement a numerical scheme that involved splitting of the flux, as was carried out for the Newtonian scheme. To overcome this, a special normalisation of the flux was introduced. This made the expression for the non-Newtonian flux to be incorporated in a ratio that was calculated explicitly, leaving only the Newtonian flux which could easily be split and implemented as before. This resulted in an innovative numerical scheme for modelling non-Newtonian flow on a rotating disk, that was simple to apply as an extension of the Newtonian scheme. The numerical scheme was checked for mass conservation and convergence, which were found to be very good. In addition to comparing well with the analytical result, the Newtonian solution could be easily recovered from the power-law and Ellis model equations by an appropriate choice of parameters.

Simulations to determine the fluid height using the power-law version of the non-Newtonian scheme was carried out for three values of the power-law parameter, two using parameter values for documented non-Newtonian fluids and the third being a theoretical one that was chosen to help bridge the gap in the n values for the power-law and Newtonian fluid. When surface tension and gravity were neglected in the power-law model, the profiles had a peak at the centre. These occurred as a result of the infinite viscosity at $r = 0$. Addition of gravity, significantly reduced these peaks. Surface tension also had some measurable influence in reducing the film height at the centre due to the curvature there. However, the most significant effect of including surface tension seemed to be at the front, where the capillary ridge developed. Surface tension is known to slightly reduce the rate of spreading for Newtonian fluids, and this was observed too in power-law fluids.

Simulations to determine the film height using the Ellis model were carried out using two values of the Ellis model parameter, for the same non-Newtonian fluids used in the power-law simulations. The Ellis model is one of several viscosity models that attempt to describe power-law shear-thinning at large shear rates, with a transition to Newtonian behaviour at low shear rates. Therefore, the governing equation for the Ellis model includes a parameter, referred to as β (> 0) in this thesis, that characterizes the onset of Newtonian behaviour. The Ellis model with $0 < \beta < 1$, provided more realistic film profiles than the power-law in the sense that the central peak was not observed. For larger values of $\beta \geq 1$, the Ellis model showed film heights that were not only uniform but thinner than the Newtonian film. This is in agreement with experimental observations, using polymer resists.

The fourth order surface tension term led to numerical difficulties in the Newtonian model.

Addition of this term to the non-Newtonian models added further complexity. However, the results showed the important role surface tension plays in the shape and spreading of the film, especially in the immediate vicinity of the contact line for both fluids and near the centre for power-law fluids. Therefore, surface tension should be included in the spin coating model, particularly if the front is to be modelled accurately.

In this thesis, we successfully included surface tension effects in non-Newtonian models, by developing an innovative numerical scheme that was used to solve the governing equations. Results obtained for the numerical scheme using power-law fluids, with surface tension and gravity neglected, were in agreement with previous theoretical investigations. The Ellis model predicted more realistic profiles that did not leave peaks at the centre, in line with experimental observations. For $\beta > 1$, the Ellis model predicted film profiles that were thinner than the Newtonian films. This too, is in agreement with previous experimental work.

Further work

The models and numerical schemes developed in this thesis have provided insight into the spin coating process, especially of non-Newtonian models. However, several features of this study could be further investigated:

- The numerical scheme for a power-law fluid has convergency problems when $n < 0.5$. This requires the use of larger space steps ($\Delta r > 1.25 \times 10^{-2}$) compared to those employed in the other numerical schemes ($\Delta r \leq 5 \times 10^{-4}$). This compromises the accuracy of the scheme and in extreme cases can result in the loss of certain features (the capillary ridge in particular). The numerical scheme should therefore be developed further to overcome this deficiency.

- Comparison with experimental data. It would be extremely useful to combine this work with an experimental investigation to verify the results presented for practical application.

- Fingering is a problem that occurs at the moving contact line and can result in uneven coating. Our analysis requires axisymmetric flow. To model fingering would involve adapting the model to asymmetric flow. However, the numerical method would not change greatly.

- A common form of non-Newtonian fluids are the viscoplastic or "yield stress" fluids. Extending the models and numerical scheme to deal with these types of fluids would significantly increase the applicability of this work.

****

Bibliography

[1] http://www.disctronics.co.uk/technology/manuf/rep_metlac.htm. Last accessed 21/09/05.

[2] http://www.cinram.com/cd/tech/cdmake.pdf. Last accessed 19/03/06.

[3] http://www.mfdigital.com/2004/06/cd-manufacturing-replication.html. Last accessed 19/03/06.

[4] http://www.pctechguide.com/08cd-rom-The-disc.htm. Last accessed 21/09/05.

[5] http://www.cdman.com/technical/howdocdswork8.html. Last accessed 19/03/06.

[6] http://www.osta.org/technology/dvdqa/dvdqa13.htm. Last accessed 19/03/06.

[7] http://www.synthemedia.com/mtc/qa/overview.html. Last accessed 19/03/06.

[8] http://www.medialinenews.com/issues/2001/news/0314/0314.1.shtml. Last accessed 19/03/06.

[9] http://www.cise.columbia.edu/clean/process/spintheory.pdf. Last accessed 19/03/06.

[10] D. J. Acheson. *Elementary Fluid Dynamics.* Clarendon Press, Oxford, 1990.

[11] A. Acrivos, M. J. Shah, and E. E. Pertersen. On the flow of a non-Newtonian fluid on a rotating disk. *J. Appl. Phys.*, 31:963–968, 1960.

[12] W. F. Ames. *Numerical Methods for Partial Differential Equations.* Academic Press, 2nd edition, 1977.

[13] S. I. Betelú and M. A. Fontelos. Capillarity driven spreading of circular drops of shear-thinning fluid. *Math. & Comp. Modelling*, 40:729–734, 2004.

[14] R. B. Bird. Useful non-Newtonian models. *Annual Review of Fluid Mech.*, 8:13–34, 1976.

[15] R. B. Bird, R. C. Armstrong, and O. Hassager. *Dynamics of polymeric liquids*, volume 1. J.Wiley & Sons, 1977.

[16] D. E. Bornside, C. W. Macosko, and L. E. Scriven. On the modelling of spin coating. *J. Imag. Sci. Tech.*, 13:122–130, 1987.

[17] S. J. Chapman, A. D. Fitt, and C. P. Please. Extrusion of power-law shear-thinning fluid with small exponent. *Int. J. Non-Linear Mech.*, 32(1):187–199, 1997.

[18] J. P. F. Charpin. *Water flow on accreting ice surfaces.* PhD thesis, Cranfield University, UK, 2002.

[19] A. F. Charwat, R. E. Kelly, and C. Gazley. The flow and stability of thin liquid films on a rotating disk. *J. Fluid Mech.*, 53(2):227–255, 1972.

[20] N. P. Cheremisinoff, editor. *Rheology and Non-Newtonian Flows*, volume 7 of *Encyclopedia of Fluid Mechanics.* Gulf Publishing Co., 1988.

[21] W. J. Daughton and F. L. Givens. An investigation of the thickness variation of spun-on thin films commonly asociated with the semi-conductor industry. *J. Electrochem. Soc.*, 129:173–179, 1982.

[22] V. E. B. Dussan. The moving contact line: the slip boundary condition. *J. Fluid Mech.*, 77:665–684, 1976.

[23] V. E. B. Dussan. On the spreading of liquids on solid surfaces: Static and dynamic contact lines. *Ann. Rev. Fluid Mech.*, 11:371–400, 1979.

[24] V. E. B. Dussan and S. H. Davis. On the motion of a fluid-fluid interface along a solid interface. *J. Fluid Mech.*, 65:71–95, 1974.

[25] A. G. Emslie, F. T. Bonner, and L. G. Peck. Flow of a viscous liquid on a rotating disk. *J. Appl. Phys.*, 29(5):858–862, 1958.

[26] H. Espig and R. Hoyle. Waves in a thin liquid layer on a rotating disk. *J. Fluid Mech.*, 22(4):671–677, 1965.

[27] W. W. Flack, D. S. Soong, A. T. Bell, and D. W. Hess. A mathematical model for spin coating of polymer resists. *J. Appl. Phys.*, 56(4):1199–1207, 1984.

[28] C. A. J. Fletcher. *Computational Techniques for Fluid Dynamics*, volume I of *Springer series in Computational Physics*. Springer-Verlag, 1991.

[29] N. Fraysee and G. M. Homsy. An experimental study of rivulet instabilities in centrifugal spin coating of viscous Newtonian and non-Newtonian fluids. *Phys. Fluids*, 6(4):1491–1504, 1994.

[30] P. G. De Gennes. Wetting: Statics and dynamics. *Rev. Mod. Phys.*, 57:827–863, 1985.

[31] B. G. Higgins. Film flow on a rotating disk. *Phys. Fluids*, 29(11):3522–3529, 1986.

[32] L. M. Hocking. A moving fluid interface Part 2. The removal of the force singularity by a slip flow. *J. Fluid Mech.*, 79:209–229, 1977.

[33] F. A. Howes. The asymptotic solution of a class of third-order boundary value problems arising in the theory of thin film flows. *SIAM J. Appl. Math.*, 43(5):993–1004, 1983.

[34] C. Huh and L. E. Scriven. Hydrodynamic model of steady movement of a solid/liquid/fluid contact line. *J. Colloid Interface Sci.*, 35:85–101, 1971.

[35] J. H. Hwang and F. Ma. On the flow of a thin liquid film over a rough rotating disk. *J. Appl. Phys.*, 66:388–394, 1989.

[36] S. A. Jenekhe. The rheology and spin coating of polyimide solutions. *Polymer Eng. Sci.*, 23:830–834, 1983.

[37] S. A. Jenekhe. Effects of solvent mass transfer on flow of polymer solutions on a flat rotating disk. *Ind. Eng. Chem. Fundam.*, 23(4):425–432, 1984.

[38] S. A. Jenekhe and S. B. Schuldt. Coating flow of non-Newtonian fluids on a flat rotating disk. *Ind. Eng. Chem. Fundam.*, 23(4):432–436, 1984.

[39] O. E. Jensen and J. B. Grotberg. Insoluble surfactant spreading on a thin viscous film; shock evolution and film rupture. *J. Fluid Mech.*, 240:259–288, 1992.

[40] D. E. Kataoka and S. M. Troian. A theoretical study of instabilities at the advancing front of thermally driven coating films. *J. Colloid Interface Sci.*, 192:350–362, 1997.

[41] J. R. King. The spreading of power-law fluids. *IUTAM Symposium on Free Surface Flows*, pages 153–160, 2001. eds. A. C. King and Y. D. Shikhmurzaev.

[42] A. Kitamura. Thermal effects on liquid film flow during spin coating. *Phys. Fluids*, 13(10):2788–2794, 2001.

[43] S. S. Kucherenko and K D Leaver. Modelling effects of surface tension on surface topology in spin coatings for integrated optics and micromechanics. *J. Micromech. Microeng.*, 10:299–308, 2000.

[44] L. Landau and B. Levich. Dragging of a liquid by a moving plate. *Acta Physicochim. URSS*, 17:42–54, 1942.

[45] L. D. Landau and E. M. Lifshitz. *Fluid Mechanics*, volume 6 of *Course of Theoretical Physics*. Pergamon Press, 1987.

[46] R. G. Larson and T. G. Rehg. *Liquid Film Coating*, chapter Spin Coating, pages 709–734. Chapman & Hall, 1997. (ed. Kistler S F and Schweizer P M).

[47] C. J. Lawrence. The mechanics of spin coating of polymer films. *Phys. Fluids*, 31(10):2786–2795, 1988.

[48] C. J. Lawrence. Spin coating with slow evaporation. *Phys. Fluids A*, 2(3):453–456, 1989.

[49] C. J. Lawrence and W. Zhou. Spin coating of non-Newtonian fluids. *J. Non-Newtonian Fluid Mech.*, 39:137–187, 1991.

[50] A. F. M. Leenaars, J. A. M. Huethorst, and J. J. Van Oekel. Marangoni drying: A new extremely clean process. *Langmuir*, 11:1701–1703, 1990.

[51] G. I. Lepehin and G. V. Riabchuk. Temperature distribution in film of viscous liquid with heating on a rotating disk. *Rheology in Processes and Apparatus of Chemical Technology, Works of Polytechnic Institute of Volgograd*, pages 82–91, 1975. (in Russian).

[52] I. Leshev and G. Peev. Film flow on a horizontal rotating disk. *Chem. Eng. & Proc.*, 42:925–929, 2003.

[53] D. R. Lide and H. P. R. Frederikse, editors. *Handbook of Chemistry and Physics*. CRC Press, 76th edition, 1995.

[54] J. Marra and J. A. M. Huethorst. Physical principles of Marangoni drying. *Langmuir*, 7:2748–2755, 1991.

[55] B. S. Massey. *Mechanics of Fluids*. Chapman & Hall, 6th edition, 1989.

[56] S. Matsuhisa and R. B. Bird. Analytical and numerical solutions for laminar flow of the non-Newtonian Ellis fluid. *A.I.Ch.E.*, 11(4):588–595, 1965.

[57] F. Melo, J. F. Joanny, and S. Fauve. Fingering instability of spinning drops. *Phys. Rev. Lett.*, 63:1958–1961, 1989.

[58] D. Meyerhofer. Characteristics of resist films produced by spinning. *J. Appl. Phys.*, 49(7):3993–3997, 1978.

[59] S. Middleman. The effect of induced air-flow on the spin coating of viscous liquids. *J. Appl. Phys.*, 62:2530–2532, 1987.

[60] E. Momoniat and D. P. Mason. Investigation of the effect of the Coriolis force on a thin fluid on a rotating disk. *Int. J. Non-Linear Mech.*, 33(6):1069–1088, 1998.

[61] W. M. Moreau. *Semi-Conductor Lithography*. Plenum Press, New York, 1988.

[62] J. A. Moriarty and L. W. Schwartz. Effective slip in numerical calculations of moving-contact-line problems. *J. Eng. Math.*, 26:81–86, 1992.

[63] J. A. Moriarty, L. W. Schwartz, and E. O. Tuck. Unsteady spreading of thin liquid films with small surface tension. *Phys. Fluids A*, 3(5):733–742, 1991.

[64] T. G. Myers. Thin films with high surface tension. *SIAM Review*, 40(3):441–462, 1998.

[65] T. G. Myers. Application of non-Newtonian models to thin film flow. *Phys. Rev. E*, 72(066302):1–11, 2005.

[66] T. G. Myers and J. P. F. Charpin. The effect of the Coriolis force on axisymmetric rotating thin film flows. *Int. J. Non-Linear Mech.*, 36:629–635, 2001.

[67] T. G. Myers and M. Lombe. The importance of the Coriolis force on horizontal rotating thin film flows. *Chem. Eng. & Proc.*, 45:90–98, 2006.

[68] D. J. Needham and J. H. Merkin. The development of nonlinear waves on the surface of a horizontally rotating thin liquid film. *J. Fluid Mech.*, 184:357–379, 1987.

[69] S. B. G. O'Brien and L. W. Schwartz. Theory and modelling of thin film flows. *Encyclopedia of Surface and Colloid Science*, pages 5283–5297, 2002. By Marcel Dekker.

[70] H. Ockendon and J. R. Ockendon. *Viscous Flow.* Cambridge University Press, 1995.

[71] T. Ohara, Y. Matsumoto, and H. Ohashi. The film formation dynamics in spin coating. *Phys. Fluids A*, 1(12):1949–1959, 1989.

[72] A. Oron, S. H. Davis, and S. G. Bankoff. Long-scale evolution of thin liquid films. *Rev. Mod. Phys.*, 69(3):931–980, 1997.

[73] W. H. Press, S. A. Teukolsky, W. T. Vetterling, and B. P. Flannery. *Numerical Recipes in FORTRAN, The Art of Scientific Computing.* Cambridge Univesity Press, 2nd edition, 1992.

[74] S. Rafaï, D. Bonn, and A. Boudaoud. Spreading of non-Newtonian fluids on hydrophilic surfaces. *J. Fluid Mech.*, 513:77–85, 2004.

[75] J. W. Rauscher, R. E. Kelly, and J. D. Cole. An asymptotic solution for the laminar flow of thin film on a rotating disk. *J. Appl. Mech.*, 40:43–47, 1973.

[76] T. G. Rehg and B. G. Higgins. The effect of inertia and interfacial shear of film flow on a rotating disk. *Phys. Fluids*, 31(6):1360–1371, 1988.

[77] B. Reisfeld, S. G. Bankoff, and S. H. Davis. The dynamics and stability of thin liquid films during spin coating I. Films with constant rates of evaporation or adsorption. *J. Appl. Phys*, 70:5258–5266, 1991.

[78] B. Reisfeld, S. G. Bankoff, and S. H. Davis. The dynamics and stability of thin liquid films during spin coating II. Films with unit-order and large Peclet numbers. *J. Appl. Phys*, 70:5267–5277, 1991.

[79] A. B. Ross, S. K. Wilson, and B. R. Duffy. Blade coating of a power-law fluid. *Phys. Fluids*, 11(5):958–970, 1999.

[80] L. W. Schwartz. Gravity flow of a viscous liquid down a slope with injection. *Phys. Fluids*, 31(10):2739–2741, 1988.

[81] L. W. Schwartz. Hysterectic effects in droplet motions on heterogeneous substrates: direct numerical simulation. *Langmuir*, 14:3440–3453, 1998.

[82] L. W. Schwartz and R. V. Roy. Theoretical and numerical results for spin coating of viscous fluids. *Phys. Fluids*, 16(3):569–584, 2004.

[83] F. S. Sherman. *Viscous Flow.* McGraw-Hill, 1990.

[84] Y. D. Shikhmurzaev. The moving contact line on a smooth solid surface. *Int. J. Multiphase Flow*, 19(4):589–610, 1993.

[85] M. A. Spaid and G. M. Homsy. Stability of Newtonian and viscoelastic dynamic contact lines. *Phys. Fluids*, 8(2):460–478, 1996.

[86] L. L. Spangler, J. M. Torkelson, and J. S. Royal. Influence of solvent and molecular weight on thickness and surface topography of spin-coated polymer films. *Polymer Eng. Sci.*, 30(11):644–653, 1990.

[87] R. I. Tanner. *Engineering Rheology.* Oxford University Press, Revised edition, 1988.

[88] J. W. Thomas. *Numerical Partial Differential Equations - Finite Difference Methods.* Texts in Applied Mathematics (22). Springer, 1995.

[89] J. W. Thomas. *Numerical Partial Differential Equations - Conservation Laws and Elliptic Equations.* Texts in Applied Mathematics (33). Springer, 1999.

[90] L. F. Thomson, C. G. Willson, and M. J. Bowden. *Introduction to Microlithography.* American Chemical Society, Washington DC, 1983.

[91] D. J. Tritton. *Physical Fluid Dynamics.* Van Nostrand Reinhood (UK), 1977.

[92] S. M. Troian, E. Herbolzheimer, S. A. Safran, and J. F. Joanny. Fingering instabilities of driven spreading films. *Europhys. Lett.*, 10(1):25–30, 1989.

[93] Y. Tu. Depletion and retention of fluid on a rotating disk. *J. Lub. Technol.*, 105:625–629, 1983.

[94] E. O. Tuck and L. W. Schwartz. A numerical and asymptotic study of some third order ODEs relevant to draining and coating flows. *SIAM Review*, 32(3):453–469, 1990.

[95] D. E. Weidner and L. W. Schwartz. Contact-line motion of shear-thinning liquids. *Phys. Fluids*, 6(11):3535–3538, 1994.

[96] P. Wesseling. *Principles of Computational Fluid Dynamics.* Springer series in compuational mathematics (29). Springer, 1991.

[97] W. E. Williams. *Partial Differential Equations.* Clarendon Press, Oxford, 1980.

[98] S. K. Wilson, R. Hunt, and B. R. Duffy. The rate of spreading in spin coating. *J. Fluid Mech.*, 413:65–88, 2000.

[99] M. Yanagisawa. Slip effect for thin liquid film on rotating disk. *J. Appl. Phys.*, 61(3):1034–1037, 1987.